Available online at www.sciencedirect.com
ScienceDirect
Acta Materialia 55 (2007) 4067–4109
Acta MATERIALIA
www.elsevier.com/locate/actamat

Overview No. 144

Mechanical behavior of amorphous alloys

Christopher A. Schuh [a,*], Todd C. Hufnagel [b], Upadrasta Ramamurty [c]

[a] Department of Materials Science and Engineering, Massachusetts Institute of Technology, 77 Massachusetts Avenue, M.I.T., Cambridge, MA 02139, USA
[b] Department of Materials Science and Engineering, Johns Hopkins University, Baltimore, MD 21218, USA
[c] Department of Materials Engineering, Indian Institute of Science, Bangalore-560 012, India

Received 14 August 2006; received in revised form 29 January 2007; accepted 31 January 2007
Available online 19 April 2007

Abstract

The mechanical properties of amorphous alloys have proven both scientifically unique and of potential practical interest, although the underlying deformation physics of these materials remain less firmly established as compared with crystalline alloys. In this article, we review recent advances in understanding the mechanical behavior of metallic glasses, with particular emphasis on the deformation and fracture mechanisms. Atomistic as well as continuum modeling and experimental work on elasticity, plastic flow and localization, fracture and fatigue are all discussed, and theoretical developments are connected, where possible, with macroscopic experimental responses. The role of glass structure on mechanical properties, and conversely, the effect of deformation upon glass structure, are also described. The mechanical properties of metallic glass-derivative materials – including in situ and ex situ composites, foams and nanocrystal-reinforced glasses – are reviewed as well. Finally, we identify a number of important unresolved issues for the field.

Keywords: Metallic glass; Amorphous metal; Mechanical properties

1. Introduction

Amorphous metallic alloys represent a relatively young class of materials, having been first reported in 1960 when Klement et al. performed their classic rapid-quenching experiments on Au–Si alloys [1]. Since that time, there has been remarkable progress in exploring alloy compositions for glass formers, seeking elemental combinations with ever-lower critical cooling rates for the retention of an amorphous structure. The so-called "bulk" glass-forming alloys represent particularly impressive success in this endeavor, with characteristic specimen sizes in excess of 1 mm. These bulk glass formers – mostly complex alloys based on multicomponent mixtures – are now known to be numerous, and manifest intriguing properties due to their amorphous structures. There are several succinct and thorough recent reviews covering the science of glass forming, glass structure, and the interesting and potentially valuable properties of amorphous metals [2–4].

One of the enduring attractions of amorphous alloys is their interesting (and impressive) suite of mechanical properties. The mechanics of metallic glasses have proven to be of fundamental scientific interest for their contrast with conventional crystalline metals, and also occupy a unique niche compared with other classes of engineering materials. For example, amorphous alloys generally exhibit elastic moduli on the same order as conventional engineering metals, but have room-temperature strengths significantly in excess of those of polycrystals with comparable composition. And while they usually suffer a strong tendency for shear localization and macroscopically brittle failure at ambient temperature, there is clear evidence that metallic glasses are capable of legitimate plastic shear flow at the microscale. The consequent promise of high strength with non-negligible toughness has inspired substantial research effort on the room-temperature properties of metallic glasses. At the same time, the amorphous structure leads

* Corresponding author.
E-mail address: schuh@MIT.EDU (C.A. Schuh).

1359-6454/$30.00
doi:10.1016/j.actamat.2007.01.052

Nomenclature

a	crack length
A	temperature-dependent constant
B	bulk modulus
c_t	transverse wave speed
C	constraint factor
C_s	constant pertaining to strength in the inhomogeneous regime
D	constant pertaining to strength in the inhomogeneous regime
E	Young's modulus
ΔF_o	free energy for STZ activation
G_c	fracture energy
ΔG_s	activation free enthalpy to initiate deformation
h	indentation depth
H	hardness
k	Boltzmann constant
k_y	shear resistance or shear flow stress
K_c	fracture toughness
K_{Ic}	mode I fracture toughness
ΔK	stress intensity factor
m	Paris law exponent
n	stress sensitivity
N	number of fatigue loading cycles
p	hydrostatic pressure
P	load
Q	activation energy
r	distance ahead of a propagating shear front
r_p	plastic zone size
$\dot{s}$	diffusion jump rate
S	stress amplitude
T	temperature
T_{DB}	ductile-to-brittle transition temperature
T_g	glass transition temperature
T_o	reference temperature for excess free volume
ΔT	temperature increase above ambient
$\dot{u}$	shear displacement rate
Δu	shear displacement, as on a shear band
Δu^*	critical shear displacement for fracture
v_f	average free volume assigned to each atom
v^*	critical volume required for deformation
$\bar{v}$	mean free volume
V	activation volume
V_p	volume fraction of the reinforcement particles
α	coefficient of normal stress or pressure dependence (see also α_p and α_n)
α_{cte}	volume coefficient of thermal expansion
α_n	coefficient of normal stress dependence
α_o	parameter pertaining to the volume fraction of deformable material
α'_o	modified version of α_o for uniaxial loading
α_p	coefficient of pressure dependence
β	ratio of the dilatation to the shear strain of an STZ
γ	shear strain
$\dot{\gamma}$	shear strain rate
γ_c	critical strain for localization
γ_o	characteristic strain of an STZ
$\dot{\gamma}_m$	strain rate in an amorphous matrix surrounding a forming shear band
$\dot{\gamma}_s$	characteristic strain rate of shear banding
γ_t	surface tension
δ	shear band thickness
δ_i	plastic zone size around an indentation
$\dot{\varepsilon}$	uniaxial strain rate
κ	thermal conductivity
λ_c	critical wavelength of an instability
μ, $\mu(T)$	shear modulus, temperature-dependent shear modulus
ν	Poisson's ratio
ν_o	attempt frequency for an STZ
σ	uniaxial stress
σ_0	yield stress in uniaxial tension or compression
σ_0^c	yield stress in uniaxial compression
$\sigma_1,\sigma_2,\sigma_3$	principal stresses
σ_n	normal stress acting on the shear plane
σ_y	yield strength
σ_u	uniaxial tensile strength
σ_m	yield or flow stress of the amorphous matrix of a composite
σ_p	yield or flow stress of a reinforcement phase in a composite
τ	shear stress
τ_o	athermal shear stress
τ_y	effective yield stress
θ	angle of the shear plane with respect to the uniaxial loading axis
χ	fraction of plastic work converted into heat
ξ	geometrical constant of order unity
ζ	pressure gradient ahead of the crack tip
Ω_o	characteristic volume of an STZ
Ω_s	characteristic volume for a critical shear event

to high-temperature rheological properties well known in other glassy systems, including oxides and amorphous polymers: stable Newtonian flow at low stresses enables superplastic-like deformation that may be useful in shape-forming operations.

The availability of more and larger amorphous alloy specimens, combined with the intriguing collection of properties outlined above, has led to a rapid proliferation of research on the mechanical properties of metallic glasses over the past decade or so. Entirely new classes of metal

glass-based materials have also been developed – including foams, composites and nanocrystal-reinforced alloys – whose mechanical properties are just beginning to be studied seriously. There are a number of recent papers which outline the mechanical properties of metallic glasses in broad strokes, which tabulate and compare the properties among glasses of different and varied compositions, or which review some specific properties in detail [2–7]. On the other hand, the fundamental principles and mechanisms that underpin the mechanical properties of amorphous metals have not yet been holistically synthesized with the accumulation of new data over the past decade or so.

Our purpose in this article is to present an overview of the mechanical properties of metallic glasses with a specific focus upon fundamentals and mechanisms of deformation and fracture. This synthesis follows in the vein of the classic review articles of Pampillo (1975) [8] and Argon (1993) [9]; while many of the concepts laid out in these earlier reviews remain equally valid today, we incorporate here what we view as the most important refinements, revisions and recent advances in understanding the deformation of metallic glasses and their derivatives. Beginning from an atomistic picture of deformation mechanisms in amorphous metal, we proceed to review elastic, plastic and fracture behavior in light of these mechanisms. We then explore the importance of glass structure and its evolution during deformation, and survey the growing literature on ductilization of metallic glasses. The paper concludes with a view of important unresolved questions for what is a rapidly expanding field of research.

2. Deformation mechanisms

Because the bonding in amorphous alloys is of primarily metallic character, strain can be readily accommodated at the atomic level through changes in neighborhood; atomic bonds can be broken and reformed at the atomic scale without substantial concern for, e.g. the rigidity of bond angles as in a covalent solid, or the balance of charges as in an ionic solid. However, unlike crystalline metals and alloys, metallic glasses do not exhibit long-range translational symmetry. Whereas crystal dislocations allow changes in atomic neighborhood at low energies or stresses in crystals, the local rearrangement of atoms in metallic glasses is a relatively high-energy or high-stress process.

The exact nature of local atomic motion in deforming metallic glasses is not fully resolved, although there is general consensus that the fundamental unit process underlying deformation must be a local rearrangement of atoms that can accommodate shear strain. An example of such a local rearrangement is depicted in the two-dimensional schematic of Fig. 1a, originally proposed by Argon and Kuo [10] on the basis of an atomic-analog bubble-raft model. The event depicted in Fig. 1a has been referred to as a "flow defect" or "τ defect" [11,12], a "local inelastic transition" [13–15] and, increasingly commonly, a "shear transformation zone" (STZ) [12,16–22]. The STZ is essentially a local cluster of atoms that undergoes an inelastic shear distortion from one relatively low energy configuration to a second such configuration, crossing an activated configuration of higher energy and volume. Since the original analog model of Argon et al. [10,23], more sophisticated computer models have been employed to study glass deformation in both two and three dimensions [11,12,16,18,24–38]. STZs comprising a few to perhaps ~100 atoms are commonly observed in such simulation works, which span a variety of simulated compositions and empirical interatomic potentials; this suggests that STZs are common to deformation of all amorphous metals, although details of the structure, size and energy scales of STZs may vary from one glass to the next.

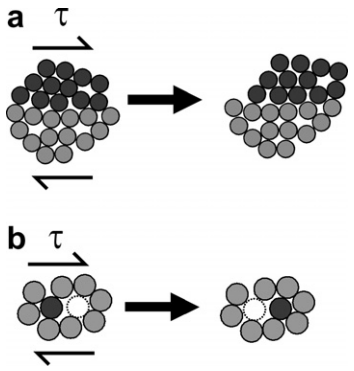

Fig. 1. Two-dimensional schematics of the atomistic deformation mechanisms proposed for amorphous metals, including (a) a shear transformation zone (STZ), after Argon [40], and (b) a local atomic jump, after Spaepen [39].

It is important to note that an STZ is not a structural defect in an amorphous metal in the way that a lattice dislocation is a crystal defect. Rather, an STZ is defined by its transience – an observer inspecting a glass at a single instant in time cannot, a priori, identify an STZ in the structure, and it is only upon inspecting a change from one moment in time (or strain) to the next that STZs may be observed and cataloged. In other words, an STZ is an event defined in a local volume, not a feature of the glass structure. This is not to suggest that the operation of an STZ is independent of the glass structure; indeed, STZ operation is strongly influenced by local atomic arrangements, and also has important consequences for structural evolution of a deforming glass. In a metallic glass body experiencing uniform stress, the STZ that is activated first is selected from among many potential sites on the basis of energetics, which vary with the local atomic arrangements [11,27,36–38]. For example, the local distribution of free volume is widely believed to control deformation of metallic glasses [10,23,39–42], and it is easy to envision that sites of higher free-volume would more readily accommodate local shear. Atomistic simulations have also correlated other structural state variables with local shearing, including short-range chemical or topological order [11,43,44].

The first quantitative model of STZ behavior was developed by Argon [40], who treated the problem in the context of an Eshelby-type inclusion [45]. In this scenario, the STZ operation takes place within the elastic confinement of a surrounding glass matrix, and the shear distortion leads to stress and strain redistribution around the STZ region. Argon calculated the free energy for STZ activation in terms of the elastic constants of the glass as

$$\Delta F_{\mathrm{o}} = \left[\frac{7-5\nu}{30(1-\nu)} + \frac{2(1+\nu)}{9(1-\nu)}\beta^2 + \frac{1}{2\gamma_{\mathrm{o}}}\cdot\frac{\tau_{\mathrm{o}}}{\mu(T)}\right]\cdot\mu(T)\cdot\gamma_{\mathrm{o}}^2\cdot\Omega_{\mathrm{o}} \tag{1}$$

Here ν is Poisson's ratio, τ_{o} is the athermal shear stress at which the STZ transforms, and $\mu(T)$ is the temperature-dependent shear modulus. The second term in the brackets captures the dilatational energy associated with STZ operation, and β is the ratio of the dilatation to the shear strain. Based on analog models of glass plasticity [10,23], the characteristic strain of an STZ, γ_{o}, is usually taken to be of order ~0.1, although this quantity can certainly be expected to vary across glass compositions and structural states. The characteristic volume of the STZ, Ω_{o}, is generally believed to encompass between a few and perhaps ~100 atoms, as supported by simulations and a variety of indirect experimental measurements [10,11,18,23,36–38,41,46–50]. Using typical values for transition metals, the bracketed term in Eq. (1) is of order unity, and the energy of an STZ is usually on the order of 1–5 eV, or ~20–120kT_{g}, with k the Boltzmann constant, and T_{g} the glass transition temperature.

An alternative, complementary viewpoint on the mechanism of plastic flow in metallic glasses is given by the classical "free-volume" model, as developed by Turnbull and co-workers [51,52] and applied to the case of glass deformation by Spaepen [39]. This model essentially views deformation as a series of discrete atomic jumps in the glass, as depicted schematically in Fig. 1b; these jumps are obviously favored near sites of high free volume which can more readily accommodate them. Because of the diffusion-like character of the process, the characteristic energy scale is of the order of the activation energy for diffusion, ~15–25kT_{g} [39,52,53], which is quite similar to the lower end of the range for the expected energy for an STZ operation. However, whereas the STZ activation energy corresponds to a subtle redistribution of many atoms over a diffuse volume, the activation energy in the free volume model corresponds to a more highly localized atomic jump into a "vacancy" in the glass structure.

If glass deformation were driven by local diffusive-like jumps such as envisioned in Fig. 1b, then one might expect a bias from gradients in pressure or normal stress, such as drive diffusional flow in polycrystalline solids [54–56]. It is not clear why local diffusive jumps would be biased by shear (deviatoric) stresses, and a single atomic jump does not accommodate shear strain [54]. Nonetheless, the free-volume model introduces a simple state variable to the problem of glass deformation, and allows constitutive laws to be developed on the basis of competing free volume creation and annihilation through a simple mechanism (such models are reviewed in Section 4).

Despite differences in the conceived atomic motions underlying the STZ-type model and the diffusive-jump-type model, these atomic-scale mechanisms share many common features that are crucial to understanding the macroscopic deformation response of metallic glasses:

- Both mechanisms exhibit characteristics of a two-state system; "forward" jumps or STZ operations compete with "backward" ones, and these can occur at the same spatial position in succession. This behavior has implications for the rheology of flowing glass, as well as anelastic and cyclic deformation.
- Both mechanisms are thermally activated, and exhibit similar energy scales; strength and flow character are significantly dependent upon temperature, and can be predicted on the basis of transition-state theory for thermally activated processes.
- Both mechanisms are dilatational; not only is a transient dilatation required at the saddle point configuration, but a semi-permanent free-volume increase is presumed to accumulate locally after the operation of either mechanism. Such dilatation has important consequences for flow localization and pressure dependency of mechanical properties.

A final important point about the deformation of metallic glasses is further shared by both the diffusive-jump and STZ viewpoints, and is best appreciated through comparison with the conventional view of deformation mechanisms in crystalline solids. In polycrystals one can generally enumerate a large number of distinct atomistic mechanisms, each with its own characteristic energy, size and time scales (e.g. dislocation climb, glide, diffusional flow). Deformation is viewed as a competition of rates from among these mechanisms, and the dominant mechanism depends upon temperature, strain rate and microstructure. In contrast, at present it seems that in metallic glasses only a single mechanism is required to explain the basic features of deformation over the full range of temperatures, strain rates and conceivable glass structures. This mechanism (whether one subscribes to an STZ-type or diffusive-jump mechanism) may occur homogeneously throughout a glass body, or may occur in a localized mode as during the formation of a shear band. Although the macroscopic mechanical response may differ between these two cases, the deformation mechanism is, at least nominally, the same. Of course, due to the complex distribution of local states in a metallic glass, the individual mechanistic events (STZ operations or atomic jumps) should actually occur with a spectrum of characteristic sizes and energies [9,40,41]. These are often replaced with reasonable averages for ease of discussion, and in fact it has been proposed that a sin-

gle, critical STZ size may be universal for many systems [36–38].

Several authors have attempted to explain plasticity in metallic glasses in terms of dislocation models [57–60], and although linear structural defects are not easily defined in an amorphous structure, the continuum notion of a dislocation line does not rely on the existence of a lattice; the general definition of a dislocation is the boundary between a region of material which has sheared and a region which has not. Under conditions where glass deformation proceeds through shear localization, a nascent shear band may spread by propagation of a shear front, which therefore represents a kind of dislocation. Li pointed out that the stress concentration associated with such a shear front (which he viewed as a Somigliana dislocation) can contribute to shear localization [58]; this is essentially equivalent to stating that the stress concentration activates STZs ahead of the shear front, causing it to advance. One must be careful, however, in drawing analogies with dislocations in crystalline alloys. In particular, interactions between "dislocations" and microstructure do not determine the mechanical properties of amorphous alloys in the manner common to crystalline solids. An obvious example is that metallic glasses do not strain harden, even at high shear band densities. Another example is provided by nanoindentation measurements of the hardness of nanoscale multilayers. The hardness of crystalline multilayers increases significantly when the bilayer period becomes small ($<$10 nm), due in part to image forces on dislocations resulting from differences in elastic modulus between the layers. In contrast, the hardness of amorphous multilayers follows a simple rule of mixtures, indicating that stored stress fields such as would be associated with discrete dislocations do not control the plastic behavior [61].

The atomic-level mechanisms outlined qualitatively above, including notably STZ- and free-volume-type models, also form the basis for more quantitative understanding of metallic glass deformation. In the remainder of this paper, we review the basic features of metallic glass deformation in reference to these mechanisms.

3. Elastic and anelastic deformation

Amorphous alloys are usually assumed to be elastically isotropic, although in some cases anisotropy can be introduced either during processing or as the result of external fields, particularly in thin films and magnetic alloys [62,63]. Isotropic materials have two independent elastic constants, commonly taken to be Young's modulus (E) and Poisson's ratio (ν). From a more fundamental point of view, however, it is useful to consider the bulk modulus (B) and shear modulus (μ), which represent the response to hydrostatic and shear stresses, respectively. The former involves bond stretching (or compression) only, while the latter involves bond distortion.

For amorphous alloys the bulk modulus is typically about 6% smaller than for crystalline alloys of similar composition [64]. The comparison is not necessarily straightforward because amorphous alloys often crystallize to complicated microstructures with multiple phases, but the difference also holds true in simulations when calculated moduli for an elemental amorphous metal are compared with known values for the crystal [65]. For crystals, B increases with increasing curvature of the interatomic potential energy well and decreases with increasing equilibrium separation between atoms [66]. A metallic glass is slightly less dense than its crystalline counterpart (density changes of 0.5–2.0% due to devitrification are typical), so on average the interatomic spacings are slightly larger in the glass. Assuming that the short-range order and thus the cohesive forces are not significantly different between the two structures, the difference in atomic separation adequately explains the difference in bulk modulus.

In contrast, the response of metallic glasses to shear stresses is significantly different from that of crystals. For instance, both μ and E are about 30% smaller in amorphous alloys than in the corresponding crystals [64,67–70], a difference that is too large to be adequately explained on the basis of a change in atomic spacing alone [71]. Weaire and co-workers [72] proposed that the difference is a result of how the local environment influences atomic rearrangements in response to shear stresses. In a crystal, each atom experiences a displacement that is defined by the macroscopic strain. An unrelaxed glass has a wider range of atomic environments and slightly less dense packing, allowing local atomic displacements that differ from those prescribed by the macroscopic strain. Simulations show that these "internal rearrangements" reduce the shear modulus by about 30%, in agreement with the experimental observations [25,65,72].

The range of atomic environments in a glass is such that some atoms reside in regions where the local topology is unstable. In these regions, the response to shear stress may include not only atomic displacements but also an anelastic reshuffling of the atomic near-neighbors (i.e. an anelastic STZ operation). Even though the fraction of atoms involved in these events may be small, the local strains are large enough that their cumulative effect makes a significant contribution to the macroscopic strain [73]. Other sources of anelasticity in metallic glasses include thermoelastic and magnetoelastic effects, similar to those in crystalline alloys [74,75]. Furthermore, like all glasses, metallic glasses show strong viscoelastic effects near the glass transition temperature, T_g [76–78].

Annealing a metallic glass can produce both reversible and irreversible structural relaxation, which affect elastic and anelastic behavior. Although it is difficult to characterize the structural changes precisely, irreversible relaxation is often associated with changes to the topological short-range order [79,80]. These result in an increase in density and a corresponding increase in elastic modulus, due to both the decreased interatomic spacing and the topological changes that make the anelastic internal rearrangements described above more difficult [3,71,81]. Consistent with

this is the observation that irreversible relaxation also reduces the internal friction below T_g [82–86].

A fully relaxed glass achieves a structure that is characteristic of the annealing temperature. Subsequent annealing at a different temperature causes changes in the structure and properties that are reversible. For instance, both elastic modulus [87] and internal friction [82] can be varied reversibly by cyclic annealing between two temperatures. The reversible structural changes are thought to be related to changes in compositional short-range order [79,80]. For instance, the room-temperature elastic modulus (E) decreases with increasing annealing temperature [87]. This is consistent with a decrease in compositional short-range order at the higher annealing temperature if we assume a preference for unlike atomic near-neighbor bonds (due to a negative heat of mixing between the constituent elements) and that these bonds are stiffer, on average, than bonds between like near-neighbors.

The internal friction effects described above have a broad distribution of relaxation times, presumably due to a similarly broad distribution of atomic environments and possible structural rearrangements. Some amorphous alloys also show distinct internal friction peaks well below T_g in the as-cast state [88–90], although others do not [86,91]. The presence of a peak suggests that the internal friction is due to specific and (relatively) well-defined structural features. Similar sub-T_g internal friction peaks can be induced by inhomogeneous deformation [85,86,91] and removed by subsequent annealing or electron irradiation [86], raising the intriguing possibility that they are somehow associated with plastic flow defects. However, the activation volume deduced from internal friction measurements is several hundred atomic volumes. This is quite large compared with some estimates for the size of individual STZs (see Sections 2 and 4.1) [40,92], although similar to recent estimates based on the potential energy landscape model [36–38].

4. Plastic deformation

The plastic deformation of metallic glasses on the macroscopic scale is essentially a biased accumulation of local strains incurred through the operation of STZs and the redistribution of free volume. Depending upon the temperature, the applied strain rate and the glass condition, these local mechanistic events can be distributed homogeneously or inhomogeneously in time and space. In this section we review these two modes of deformation in turn, and connect the atomistic deformation mechanisms described earlier with measurable macroscopic responses.

4.1. Homogeneous plastic flow

The spatially homogeneous deformation of metallic glass may be thought of as the viscous flow of a supercooled fluid, and indeed is typically observed at elevated temperatures in or near the supercooled liquid regime. The homogeneous flow of metallic glass is of direct application-relevance in shape-forming operations [93–102], and for this reason it has been studied extensively. Furthermore, when both the structure of the glass and the deformation it sustains are relatively homogeneous, the deformation becomes amenable to straightforward statistical modeling using rate theory, and the phenomenology of deformation is easy to rationalize.

4.1.1. Steady-state flow

In a steady-state condition, homogeneous flow is regarded as a balance between structural disordering and ordering, e.g. free volume creation and annihilation. Local diffusive jumps or STZ operations redistribute stresses and create free volume via dilatation, but relaxation processes are also operative to remove such free volume as it is created. In steady-state, the basic phenomenology of flow is therefore given by the biased accumulation of local STZ strains. For example, under shear loading, the activation of an STZ (or a diffusive jump) obeys a rate law of the form:

$$\dot{s} = \nu_o \cdot \exp\left(-\frac{Q - \tau V}{kT}\right) \tag{2}$$

Here $\dot{s}$ is the rate at which the event occurs under an applied shear stress τ, and kT is the thermal energy. The characteristic activation energy for the process, Q, depends on the event being described; for an STZ operation Q would be equal to ΔF_o from Eq. (1). In the STZ framework the activation volume V is the product of the characteristic STZ volume and shear strain, $\gamma_o \Omega_o$ [40,46]. The attempt frequency ν_o is essentially the frequency of the fundamental mode vibration along the reaction pathway, and should be of the order of the Debye frequency for a sufficiently local process.

Under steady-state conditions, STZ operations can occur both in favor of and in opposition to the sign of the applied stress, with activation energies $(Q - \tau V)$ and $(Q + \tau V)$, respectively. The net rate of forward operations is thus obtained by subtracting a backward STZ flux from Eq. (2). Ascribing each net forward operation the characteristic strain γ_o, the steady-state shear strain rate takes the form:

$$\dot{\gamma} = \alpha_o \nu_o \gamma_o \cdot \exp\left(-\frac{Q}{kT}\right) \sinh\left(\frac{\tau V}{kT}\right) \tag{3}$$

where α_o incorporates numerical factors as well as the fraction of material that is available to deform via the activated process. An additional minor correction may be applied to convert Eq. (3) into a uniaxial form for comparison with tensile and compressive test data [47,50,103]:

$$\dot{\varepsilon} = \alpha'_o \nu_o \gamma_o \cdot \exp\left(-\frac{Q}{kT}\right) \sinh\left(\frac{\sigma V}{\sqrt{3}kT}\right) \tag{4}$$

with σ and $\dot{\varepsilon}$ the uniaxial stress and strain rate, respectively, and α'_o a modified constant.

Structural state variables may be introduced into Eq. (3) by considering the likelihood that a given site in a metallic glass will contribute to deformation. For example, Spaepen [39] envisioned that only sites of high free volume would contribute to deformation, giving:

$$\alpha_o \propto \exp\left(-\frac{\xi v^*}{v_f}\right) \tag{5}$$

where the average free volume assigned to each atom is v_f, and a critical volume v^* is required for deformation to occur. The factor ξ is a geometrical constant of order unity. By taking the free volume to be a linearly increasing function of temperature (as would be expected due to thermal expansion), one obtains an additional correction to the Arrhenius temperature scaling of Eq. (3) [51]:

$$\alpha_o \propto \exp\left(-\frac{\xi v^*}{\alpha_{cte}\bar{v}(T-T_o)}\right) \tag{6}$$

where α_{cte} is the volume coefficient of thermal expansion, $\bar{v}$ is the mean free volume and T_o is a reference temperature. The scaling introduced in Eq. (6) has been commonly used to fit viscosity data of metallic glass-forming alloys and liquids [52,104–108]. Furthermore, the degree to which the temperature dependence of flow deviates from the simple Arrhenius form of Eq. (3) – via the additional dependence of Eq. (6) – separates "strong" from "fragile" glass formers [109]. Fragile glasses are those with structural sensitivity to temperature via Eq. (6), while strong ones more closely obey the Arrhenius form of Eq. (3).

The phenomenology of Eqs. (3) and (4) arises from the recognition that homogeneous deformation is a statistical superposition of many independent atomic-scale events with a characteristic size and energy scale; it need not be attached directly to any specific mechanism, and in fact the same general form arises naturally from both the STZ- and diffusive-jump-type mechanistic views [39,40]. Eq. (3) is generally found to be an excellent descriptor for steady-state homogeneous deformation of metallic glasses [47–50,103]. For example, Fig. 2 reproduces one of the most comprehensive sets of steady-state flow data for a metallic glass, from the work of Lu et al. on $Zr_{41.2}Ti_{13.8}Cu_{12.5}Ni_{10}Be_{22.5}$ [110]. This data encompasses more than five decades of strain rate, two of stress, as well as eight different temperatures near the glass transition of 623 K. Also shown in Fig. 2 is the best fit of Eq. (4) to these data assuming temperature independence of α_o (i.e. assuming a strong glass former); the model satisfactorily captures the complex stress dependence of the rheology, as well as the changes with temperature.

Fitting Eqs. (3) or (4) to experimental data yields values for the activation volume V as well as the activation energy, Q; such experiments therefore provide indirect quantitative insight into the atomic-scale deformation mechanism. For example, the data in Fig. 2 yield an activation energy of ~4.6 eV, or 445 kJ mol^{-1}. For $Zr_{41.2}Ti_{13.8}Cu_{12.5}Ni_{10}Be_{22.5}$, this represents an energy of about 85 times kT_g, which is of the correct order for the operation

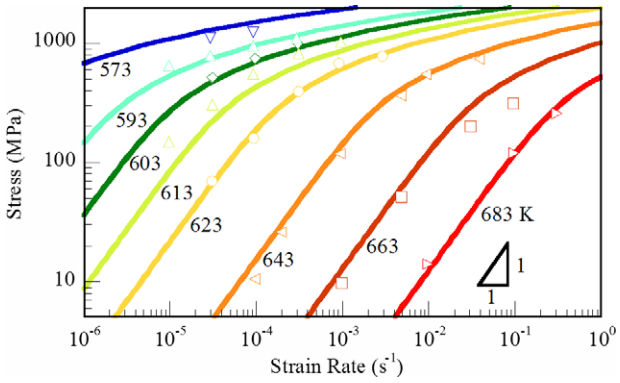

Fig. 2. Steady-state homogeneous flow data for $Zr_{41.2}Ti_{13.8}Cu_{12.5}Ni_{10}Be_{22.5}$ metallic glass at elevated temperatures, from the work of Lu et al. [110]. Also shown is the best fit of Eq. (4) obtained by treating α_o as temperature independent.

of an STZ (see Section 2). Furthermore, the data also yield a fitted activation volume $V \approx 7.5 \times 10^{-29}$ m^3. Assuming a characteristic STZ strain of ~0.1, this suggests that the characteristic STZ volume is of order $\sim 7.5 \times 10^{-28}$ m^3, roughly 40 times the Goldschmidt volume of Zr. One can therefore conclude that an average STZ probably contains about 20–30 atoms. Estimates on this same order have been obtained by other authors through similar procedures [46–50] for various different glasses. Computer simulations also reveal local shear events of the same size scale, as discussed earlier (Section 2), and if a smaller characteristic strain is assumed, STZ sizes ranging up to perhaps 100 atoms can also be justified.

The stress- or strain rate-sensitivity of flow in the steady-state condition is a topic of perennial interest in metallic glasses, largely owing to its practical implications for flow stability. At high temperatures and low applied stresses, flow is Newtonian, i.e. strain rate is proportional to stress. This can be observed in Fig. 2, where the slopes of the data series approach unity at low strain rates. The model of Eq. (3) also reduces to a Newtonian form in the low stress limit:

$$\dot{\gamma} = \frac{\alpha_o \nu_o \gamma_o V}{kT} \cdot \exp\left(-\frac{Q}{kT}\right)\tau \quad (\tau \ll kT/V) \tag{7}$$

At higher applied stress levels, the stress sensitivity of deformation drops rapidly and the flow is non-Newtonian. At sufficiently high stresses, the bias for forward STZ operation becomes very large, and the influence of the back-flux is lost:

$$\dot{\gamma} = \frac{1}{2}\alpha_o \nu_o \gamma_o \cdot \exp\left(-\frac{Q-\tau V}{kT}\right) \quad (\tau \gg kT/V) \tag{8}$$

Between the low- and high-stress limits expressed by Eqs. (7) and (8), the stress sensitivity varies continuously. Expressing the constitutive relationship as a general power law, the stress sensitivity, n, enters as:

$$\dot{\gamma} = A\tau^n \tag{9}$$

with A a temperature-dependent constant. As the strain rate is increased, the value of n increases from unity (Eq.

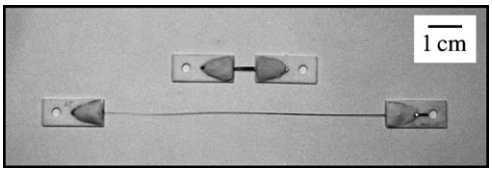

Fig. 3. Photograph of $Pd_{40}Ni_{40}P_{20}$ metallic glass specimens before (top) and after (bottom) deformation in the homogeneous condition at $T = 620$ K and $\dot{\varepsilon} \approx 10^{-1}$ s^{-1}; from Kawamura et al. [96].

(7)) to extremely high values; whereas $n = 1$ promotes stable flow, higher stress sensitivity is associated with instabilities [111–114]. In glasses the former condition leads to large extensibility of particular relevance in shape-forming contexts [96,98,115–117]. For example, Kawamura et al. [96] examined the tensile extensibility of $Pd_{40}Ni_{40}P_{20}$ metallic glass at various temperatures and rates. At higher strain rates, they observed the divergence from Newtonian flow through a rising value of n, and found a corresponding rapid decrease in tensile elongation. Whereas Newtonian conditions led to elongations in excess of 1000%, those at higher rates with non-Newtonian rheology exhibited dramatically reduced values as low as ~20%. Fig. 3 is an example of one of their tensile specimens deformed to 1260% elongation.

In addition to conventional mechanical flow instabilities such as necking, metallic glasses also appear sensitive to structural instabilities during deformation in the non-Newtonian regime. Nieh and co-workers [118,119] deformed a glass of $Zr_{52.5}Al_{10}Ti_5Cu_{17.9}Ni_{14.6}$, and observed the characteristic transition from Newtonian to non-Newtonian flow at high strain rates. They also conducted transmission electron microscopy examinations of both deformed and undeformed specimens, and suggested that non-Newtonian deformation is associated with the precipitation of nanocrystals within the glass. They further observed that in crystalline materials n may be expected to exceed unity; the presence of crystallized regions may in fact contribute to the non-Newtonian character of the rheology. A number of other authors have confirmed that homogeneous flow is often accompanied by partial crystallization and, indeed, that homogeneous deformation accelerates crystallization. Such nanocrystallization has been observed in a variety of different metallic glasses, in states of tension [98,115,116,118–120] and compression [121], as well as under more complex loading states [99]. Simple hydrostatic pressure affects crystallization, but its influence is the subject of some debate [122–138]. Nanocrystallization during flow has also been linked to strain hardening in the homogeneous regime [120,139].

4.1.2. Non-steady-state flow

Apart from the steady-state condition, homogeneous flow can also occur under conditions of structural transience; instead of a balanced condition of free volume creation and annihilation, a net gain or loss of free volume can occur during deformation. This condition is most frequently observed upon initiation of strain from a relaxed state, and leads to a characteristic stress "overshoot", as observed in Fig. 4a for $Zr_{41.2}Ti_{13.8}Cu_{12.5}Ni_{10}Be_{22.5}$. Upon loading, elastic and plastic deformation occur, and the plastic deformation leads to structural evolution (i.e. accumulation of free volume) that is accompanied by softening; the stress–strain curve therefore exhibits a peak and a decrease in stress with further applied strain. After some weakening has occurred, diffusive relaxation gradually comes to match the rate of free volume production, and a steady-state condition is eventually achieved. A complementary situation occurs during a rapid strain-rate-change experiment upon lowering of the applied strain rate, where a stress "undershoot" may be observed (see Fig. 4b).

For any set of test conditions (i.e. temperature, applied stress or strain rate) there is thus a single steady-state glass structure, and transients represent the evolution of structure towards the steady state. Steif et al. [140] presented an early mathematical description of transients in metallic glass deformation by applying the free volume model. Rather than assuming a steady-state condition, they solved differential equations for free volume production and anni-

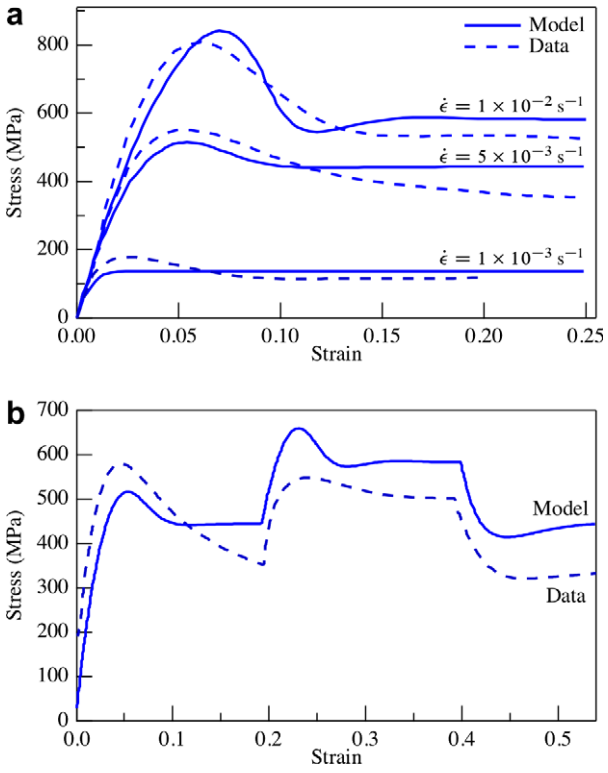

Fig. 4. Experimental data illustrating transients observed during viscous deformation of $Zr_{41.2}Ti_{13.8}Cu_{12.5}Ni_{10}Be_{22.5}$ metallic glass at 370 °C ($T/T_g = 1.03$) [110]. In (a) the experimental data exhibit characteristic stress overshoots before a steady-state condition is achieved, and the height of the overshoot increases with applied uniaxial strain rate. In (b) the non-steady-state behavior of the glass during a strain-rate change test is illustrated for three successive rates of $\dot{\varepsilon} = 5$, 10 and 5×10^{-3} s^{-1}. In both figures the predictions of a "fictive stress" internal variable model are plotted for comparison, and illustrate the general ability of such state models to capture transients in glass flow data.

hilation numerically according to the model of Spaepen [39]. They demonstrated the prediction of an overshoot due to the non-steady evolution of free volume. The ability to explain such transients is perhaps the signature success of the free volume flow model, and the free volume concept has been used consistently by other authors to interpret non-steady flow and relaxation kinetics in the homogeneous regime [46,48,93,103,104,141–147].

It is frequently presumed that free volume is an adequate state variable to describe the structure of a glass deformation process, although it is important to remember that other effects such as chemical ordering may be involved. For example, Falk and Langer [16] derived a set of time-dependent equations based on STZ activation, but incorporating a structural state description that captures transients even in the absence of thermal activation. Other authors have used concepts such as the "fictive stress" to capture structural transients [110,148,149]; these essentially replace free volume as the internal variable, and the modeling approach remains philosophically similar to that of Steif et al. [140] using the free volume evolution equations. Fig. 4 shows examples of such a model applied to transient overshoots in $Zr_{41.2}Ti_{13.8}Cu_{12.5}Ni_{10}Be_{22.5}$ (Fig. 4a) as well as a strain-rate change test (Fig. 4b). In the final analysis, any internal state variables may be used to describe the basic features of non-steady-state flow in the homogeneous region, provided that they supply a rate-dependent "memory". Experimental evidence suggests that this memory is independent of direction [150], which supports the common usage of scalar state variables.

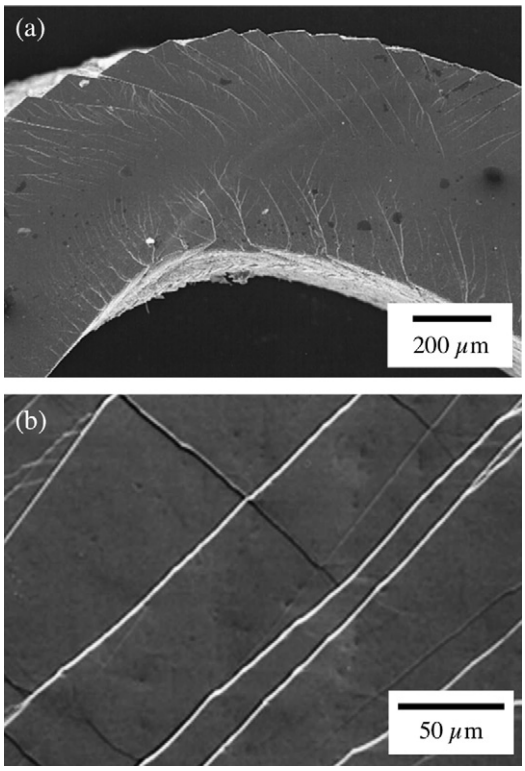

Fig. 5. Scanning electron micrographs illustrating the "slip steps" or surface offsets associated with shear bands in deformed metallic glasses. In (a) a bent strip of $Zr_{57}Nb_5Al_{10}Cu_{15.4}Ni_{12.6}$ illustrates slip steps formed in both tensile and compressive modes of loading, on the top and bottom surfaces, respectively [163]. In (b) the side of a compression specimen of $Zr_{52.5}Cu_{17.9}Ni_{14.6}Al_{10}Ti_5$ is shown, for which the loading axis was vertical [442]; here the slip steps document shear deformation at an inclined angle to the applied compressive load.

4.2. Inhomogeneous flow and shear banding

As noted earlier, constitutive laws for homogeneous deformation of metallic glass become non-Newtonian at high stresses; this transition is also promoted by a decrease in temperature. The divergence from Newtonian behavior corresponds to a decreasing rate sensitivity and a corresponding decline in flow stability. Coupled with a general lack of intrinsic strain hardening mechanisms, this leads to a strong sensitivity to perturbations, and a tendency for instability. Indeed, at very high stresses and lower temperatures metallic glasses deform essentially exclusively through localization processes. Under tensile loading, both mode I and mode II instabilities (i.e. cracking and shear banding, respectively) can be observed in metallic glasses, and the tendency for one mode over the other is apparently governed by the structure and elastic properties of the solid, as will be discussed in Section 7.3. Under most other states of loading, however, localization usually occurs in a shear mode through the formation of shear bands, which operate very rapidly and can accommodate displacements apparently up to nearly the millimeter scale [151]. Two experimental images illustrating shear "slip steps" associated with shear band operations in metallic glasses are shown in Fig. 5a and b; further discussion of the structure and character of shear bands is postponed until Section 6.2.

Whereas homogeneous flow is well described using rheological models that average the operation of many local atomic-scale events, inhomogeneous flow of metallic glasses is less analytically tractable. However, the inhomogeneous formation of shear bands has important practical consequences for the strength, ductility, toughness and eventual utility of metallic glasses. In this section we review some existing models for the localization process, and examine the effects of rate, pressure, temperature and elastic constants upon shear localization.

4.2.1. The process of localization

Shear localization or shear band formation is generally recognized as a direct consequence of strain softening – an increment of strain applied to a local volume element softens that element, allowing continued local deformation at ever-higher rates. In metallic glasses, there are a number of potential causes for strain softening and localization, including the local production of free volume due to flow dilatation, local evolution of structural order due to STZ operations, the redistribution of internal stresses associated with STZ operation, and local heat generation. Although

all of these have been discussed in the literature, the dominant contributor to localization is generally believed to be a local change in the state of the glass (i.e. a local increase in free volume or evolution of structural order). Here we examine such mechanisms in more quantitative detail; in a subsequent section (Section 4.2.2), we will revisit the question of heat generation.

Argon [40] modeled localization as a consequence of strain softening from free volume accumulation. Beginning with his STZ model, he envisioned the origin of a shear band as a local perturbation in strain rate, and examined the growth of this perturbation with applied strain in a one-dimensional model. He introduced the dynamics of free volume accumulation with strain, and its softening effect upon the glass via constitutive laws such as those described in Section 4.1. He derived and numerically solved a bifurcation equation describing the divergence of strain rate in the band and in the surrounding matrix. Fig. 6a shows the results of such a calculation, illustrating the acceleration of strain development in the shear band as the external shear strain γ increases, and the concomitant decrease of shear strain rate in the surrounding matrix.

A philosophically similar one-dimensional analysis of instability growth was developed in the context of the free volume model by Steif et al. [140]. In this case the perturbation was introduced directly as a fluctuation of free volume, and tracked by numerically solving equations for free volume and strain rate evolution. Typical results from the work of Steif et al. are illustrated in Fig. 6b, and complement those of Argon from Fig. 6a. Here the strain in the shear band is plotted as a function of the applied shear strain, and localization of strain occurs rapidly once a critical point has been reached.

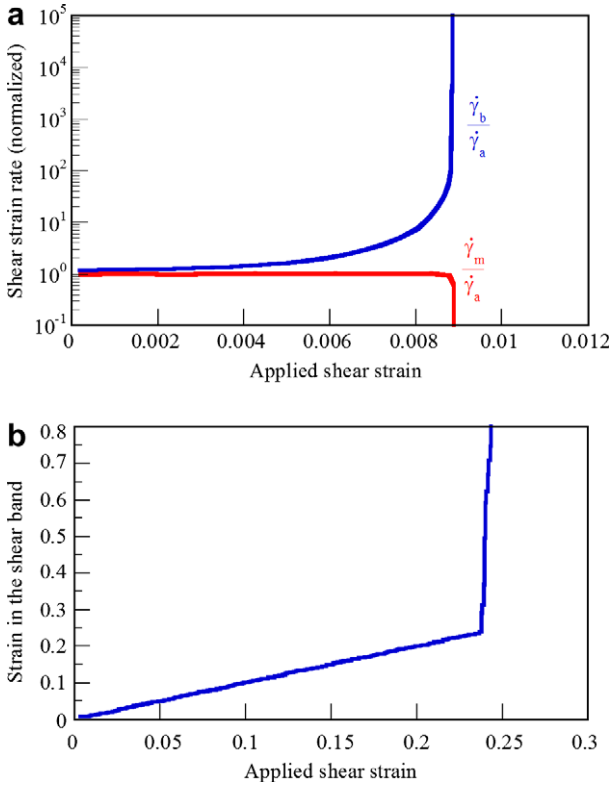

Fig. 6. Calculations from the work of (a) Argon [40] and (b) Steif et al. [140] illustrating the process of strain localization in metallic glasses. In (a), a history of strain rate is shown for both the forming shear band ($\dot{\gamma}_b$) and the surrounding matrix ($\dot{\gamma}_m$); these quantities are normalized by the applied shear strain rate. In (b), the history of strain in the shear band is shown.

Both of these models suggest the same basic sequence of events upon loading a metallic glass in the inhomogeneous regime. As stress is increased, strains are first accommodated elastically, until the stress level increases to the point where it can activate flow in a locally perturbed region. Owing to the perturbation, there is a mismatch in strain rate between the perturbed and unperturbed regions. The increased rate of strain accumulation in the perturbed region is accompanied by strain softening, which further exacerbates the strain rate mismatch in a runaway growth process. The partitioning of strain rate into a shear band occurs over a finite range of applied macroscopic strain, and the strain in the band quickly becomes very large, exceeding unity in most cases.

Plastic shearing within a mature shear band stops when the driving force for shear decreases below some threshold value, i.e. when the applied strain is fully accommodated by the shear accumulated within the band, relaxing the stress. This situation occurs commonly in constrained modes of loading, such as indentation [6], crack opening or crack tearing [152–155], or compression of low-aspect-ratio specimens [156–158]. In these cases shear bands form exclusively to accommodate the imposed shape change, and strain only to the extent required for this purpose. The result is that, after a single shear band operates and arrests, the material can be deformed further through successive shear banding operations that occur upon continued straining. Load–displacement responses from such experiments exhibit characteristic patterns of flow serration, as shown in Fig. 7a and b for constrained compression and indentation loading. Here each serration is a relaxation event associated with the formation of a shear band, registered as a load drop when the experiment is displacement-controlled (Fig. 7a), or a displacement burst under load-control (Fig. 7b).

The localization models put forth by Argon [40] and Steif et al. [140] do not capture accommodation of the applied strain and reduction of the driving force for deformation; these models assume unconstrained shear loading of matrix and shear band in parallel, under which conditions shear bands can sustain infinite strains. And, in unconstrained modes of loading, it is common to observe "infinite" strain in experiments, i.e. very large plastic strains as well as macroscopic failure along the very first shear band to form [151,159,160]. (The process of fracture will be discussed in more detail later in Section 5.1.) More sophisticated mechanical models of localization, such as the finite-element model of Anand et al. [161], can

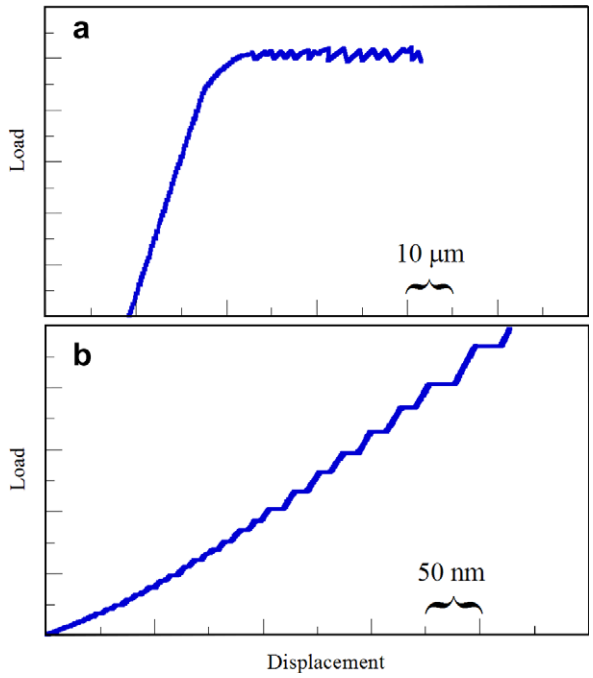

Fig. 7. Examples of mechanical test data that illustrate serrated flow of metallic glasses, through repeated shear band operation in confined loading. In (a), the compression response of a $Pd_{77.5}Cu_6Si_{16.5}$ specimen of low aspect ratio is shown [156], while (b) is an instrumented indentation curve for $Pd_{40}Cu_{30}Ni_{10}P_{20}$ glass [192]. Because (a) represents a displacement controlled experiment, serrations are represented as load drops, while the load-controlled experiment in (b) exhibits displacement bursts.

account for multiaxial loading conditions and appropriately capture the arrest of shear bands as strain is accommodated.

Under constrained loading, the net flow of metallic glasses is manifested through a series of shear banding events, and is typically characterized, on average, as elastic–perfectly plastic [162,163]. However, suggestions of macroscopic, global strain softening or hardening have been reported occasionally [158,164–170]. These effects are most frequently attributed to evolution of the glass structure owing to the severe local shearing inside of shear bands, as well as attendant evolution of heat, short-range topology and chemical order. For example, under appropriate loading conditions, the operation of "secondary" shear bands can be directly influenced by prior operation of a "primary" one [156,171,172]. In fact, secondary shear bands can in some cases operate directly atop primary ones [156,172]; i.e. more than one shear banding event can occur on the same shear plane. More details on the structural evolution within shear bands are presented in Section 6.2, and the impact of such evolution on plasticity is covered in Section 7.4.3.

The process of shear localization is a critical topic in metallic glass research, and one with many remaining outstanding questions. For example, the evolution of strain in both time and space during the initiation of a shear band remains incompletely resolved. A shear band may initially form and fill the shear plane by the spatial propagation of a small displacement (i.e. by the chaining of many STZs spatially, in sequence), followed by a stage of continued uniform shear on the same plane. Alternatively, it may occur by intense shear accumulating in a small volume, which then propagates as a front that sweeps across the shear plane. Most likely, the true sequence of events is intermediate to these two extreme cases, but details of the process remain scarce because the time scales are short for experiments, yet long for atomistic simulations. When describing or interpreting mechanical data, it is important to bear such issues in mind. Additionally, there is significant confusion regarding the definition of "shear band", a term which is variously used to describe an event, the residual trace of that event seen as a surface offset, a transient structural feature of a deforming body, or a permanently altered region within a metallic glass. In this article, we shall endeavor to separate these distinct meanings through the use of consistent language:

- "slip step" is used throughout to describe shear offsets at surfaces;
- "shear front" refers to a presumed traveling front of shear displacement;
- "shear banding event" denotes the kinetic event of shear band initiation and propagation (such as might be detected as a flow serration, whether by a single shear front or a shear front followed by continued uniform deformation on the shear band); and
- "shear band" is reserved for the approximately planar volume of material that is sheared during a "shear banding event", as a consequence of the passage of a "shear front". Note that this term may apply to a volume that experienced a shear banding event in the past, or is presently undergoing such an event; the term "operating shear band" is occasionally used to clearly differentiate the latter case from the former.

With regard to the latter two terms, it is important to remember that a single "shear band", depending upon when one observes it, may have sustained one or several distinct "shear banding events".

4.2.2. Heat evolution

There has been considerable debate as to whether shear localization in metallic glasses is due primarily to thermal effects or instead to shear-induced disordering (such as dilatation). The possibility that shear banding events are essentially adiabatic phenomena (similar to adiabatic shear bands in crystalline alloys) was first proposed by Leamy and co-workers [173], but was quickly criticized by others on the grounds that rapid thermal conduction would limit the temperature rise in a thin shear band [8]. One way to approach this question is to attempt to calculate the temperature increase resulting from shear that occurs either on the entire shear band at once [174] or as a propagating shear front [175]. Here, we take a slightly different approach by first assuming that shear

banding events *are* adiabatic, calculating some of their properties, and then comparing these to the experimental measurements.

An adiabatic shear banding event represents a competition between the rate at which heat is generated in the band due to plastic work and the rate at which heat is dissipated from the band by thermal conduction.[1] By balancing these two terms, Bai and Dodd [176] developed an expression for the thickness (δ) of a fully developed adiabatic operating shear band under steady-state conditions,

$$\delta = \sqrt{\frac{\kappa \cdot \Delta T}{\chi \cdot \tau \cdot \dot{\gamma}}} \tag{10}$$

where κ is the thermal conductivity, ΔT is the temperature increase above ambient, χ is the fraction of plastic work converted into heat, τ is the shear stress and $\dot{\gamma}$ is the shear strain rate. (ΔT, τ and $\dot{\gamma}$ all vary through the thickness of the band; here, we consider their values at the center of the band.) While only approximate, experimental observations of adiabatic shear bands in crystalline alloys suggest that this expression is accurate to within a factor of about 2 [176], which makes it adequate for order-of-magnitude calculations. More sophisticated treatments of adiabatic shear banding, including non-steady-state solutions, can be found elsewhere [177].

We can use Eq. (10) to estimate the steady-state thickness of an adiabatic shear band, but to do so we need to know τ, ΔT and $\dot{\gamma}$. (It is known that $\chi \approx 1$ [178], and we will assume that κ is known for the alloy in question.) In a complete treatment, τ would be obtained from a constitutive relation for the flow stress in terms of $\dot{\gamma}$ and T (see Section 4.1), but here we shall simply assume that it is determined by the macroscopic yield stress in shear, and take a typical value $\tau \approx 1$ GPa. Several attempts have been made to measure ΔT (see below); here, we will calculate the shear band thickness as a function of ΔT, noting that temperature increases of several hundred degrees are typically required to reach the glass transition temperature (where significant softening occurs).

Determining $\dot{\gamma}$ is not straightforward, because the strain rate inside the operating shear band can greatly exceed the macroscopic strain rate. However, in tests with macroscopic strain rates of $\sim 10^{-4}\,\mathrm{s}^{-1}$, both Neuhauser [179] and Wright and co-workers [174] measured shear displacement rates of $\dot{u} \approx 10^{-4}\,\mathrm{m\,s}^{-1}$. To get a shear strain rate, we take $\dot{\gamma} \approx \dot{u}/\delta$ and rewrite Eq. (10) as

$$\delta = \frac{\kappa \cdot \Delta T}{\chi \cdot \tau \cdot \dot{u}} \tag{11}$$

The resulting shear band thickness δ is plotted in Fig. 8 for various displacement rates $\dot{u}$ in the operating shear band.

[1] Although common, because heat is lost by conduction to the surrounding material, the use of the word "adiabatic" in this context is, strictly speaking, incorrect.

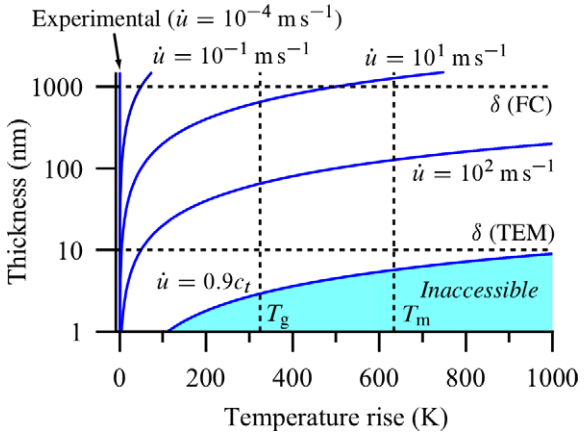

Fig. 8. Calculations based on Eqs. (10) and (11), illustrating the combinations of shear band thickness and adiabatic temperature rise that result for various shear displacement rates $\dot{u}$ on an operating shear band. The range of experimental observations for shear band thickness in metallic glasses, δ, are also illustrated with dashed horizontal lines, based on TEM observations ($\delta \sim 10$ nm) and the "fusible coating" (FC) detector ($\sim$1 μm). For the purposes of illustration, glass transition (T_g) and melting (T_m) temperatures for $Zr_{41.2}Ti_{13.8}Cu_{12.5}Ni_{10}Be_{22.5}$ are also shown.

We take $\dot{u} = 0.9c_t$ (where c_t is the transverse wave speed) as an upper bound on the displacement rate [180]. The experimentally measured values for δ range from $\sim$10 nm on the low end from electron microscopy (see Section 6.2) to $\sim$1000 nm from the "fusible coating" method (described later in this section) on the high end.

It is clear from Fig. 8 that a displacement rate on the order of $\dot{u} \approx 10^2\,\mathrm{m\,s}^{-1}$ is required to produce an adiabatic shear band consistent with the observed thickness and with the necessary ΔT to achieve significant softening. This displacement rate is approximately six orders of magnitude greater than the displacement rates that are actually observed for quasi-static loading. Put another way, if shear bands in metallic glasses were primarily adiabatic, then either the displacement rates or the shear band thicknesses would be much greater than experimental observations suggest. Thus, it appears unlikely that shear localization in metallic glasses is driven primarily by thermal (adiabatic) softening. (Note, however, that this treatment follows the conventional theory of adiabatic shear banding in taking the shear deformation to occur uniformly on the shear plane.)

These considerations notwithstanding, it is clear that significant increases in temperature do occur during shear banding events. Attempts to measure temperature rises in operating shear bands directly using thermography have been hampered by the spatial and temporal resolution of the instruments, which necessitate extrapolations to estimate the conditions inside the shear band [181–183]. Lewandowski and Greer circumvented these issues with a "fusible coating" detector [180]. They coated metallic glass specimens with a thin layer of tin and observed melting of the coating at the places where shear bands intersected the surface (Fig. 9), thus providing direct evidence of

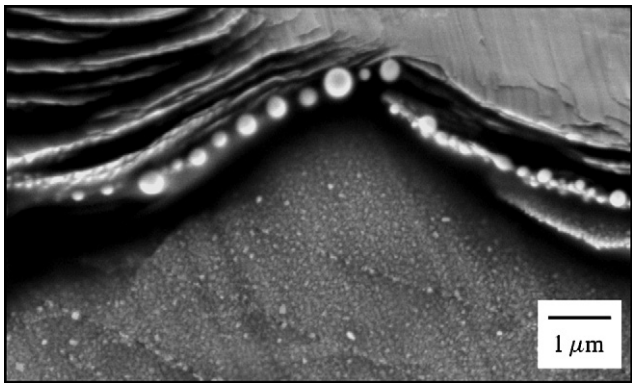

Fig. 9. A scanning electron micrograph showing the surface of a $Zr_{41.2}Ti_{13.8}Cu_{12.5}Ni_{10}Be_{22.5}$ glass initially covered with a "fusible coating" of tin and subsequently deformed [180]. At the slip steps associated with shear bands, the fusible coating has beaded due to local melting, providing evidence of heat generation within the operating shear bands.

temperature rises of $\Delta T \approx 200$ K in the operating shear bands, at least near the surface. Although the fusible coating "detector" is limited to a single temperature per experiment (the melting point of the coating), it has excellent spatial (~100 nm) and temporal (~30 ps) resolution [180]. Obtaining more specific information about the actual maximum temperature of the operating shear band requires additional approximations. However, by making a lower-bound estimate on the shear band propagation time, Lewandowski and Greer did show that the shear bands cannot be fully adiabatic, in agreement with the calculations above. Zhang and Greer reached a similar conclusion based on the thinness of the bands and the time available for thermal conduction [184].

The calculations and experiments described thus far are all for loading at low strain rates. There is evidence that the fracture stress of metallic glasses drops somewhat under dynamic compression at uniaxial strain rates $\dot{\varepsilon} > 10^2\ s^{-1}$ [159,181,185,186]. Sunny et al. have suggested that this may be an artifact resulting from premature failure due to stress concentrations at the sample/platen interface [187,188]. Another possibility is an influence of adiabatic effects (see Section 4.2.3.1) that manifest specifically at high applied strain rates. We are aware of no measurements of shear displacement rates or shear band thicknesses evolved during dynamic loading. However, the real-time cinematography in Ref. [185] suggests a shear strain rate of $\dot{\gamma} \approx 3 \times 10^7\ s^{-1}$, which gives a displacement rate of $\dot{u} \approx 30\ m\ s^{-1}$ (assuming a 1000 nm thick shear band). As Fig. 8 shows, this is in reasonable agreement with the displacement rate required to generate a fully adiabatic shear band with a temperature increase sufficient to cause significant softening of the glass. Fig. 8 does not account for the strain rate sensitivity of the flow stress, but in the high flow stress/high strain rate regime the strain rate sensitivity is not strong (Eq. (8) and Fig. 2) and thus does not affect the order-of-magnitude calculations of thermal effects considered here.

4.2.3. Phenomenology of inhomogeneous flow

4.2.3.1. Temperature and rate effects on strength. The process of shear band operation has been regarded essentially as a stress-assisted nucleation event [36,40,92,160] that takes place at high stresses, where a local shear transition is first initiated. Once an event of sufficient magnitude has occurred (a "critical" shear event) the local vicinity is softened, and continued deformation proceeds autocatalytically, with strain partitioning to the shear band as described above and in Fig. 6. The exact physical nature of the critical shear event remains elusive, but the simplest and most common assumption is that this event corresponds to the activation of a single STZ of relatively high characteristic energy. At lower temperatures this process occurs at higher stresses and without diffusive rearrangements to accommodate it, and can involve significant softening that inspires localization. If the strength of the glass is limited by the initiation of this first, critical shear event, then the constitutive law for inhomogeneous deformation is written [40]:

$$\dot{\gamma} = \dot{\gamma}_s \cdot \exp\left(-\frac{\Delta G_s}{kT}\right) \tag{12}$$

where $\dot{\gamma}_s$ is a characteristic strain rate and ΔG_s is the activation free enthalpy to initiate deformation. The exponential form of Eq. (12) differs from the hyperbolic sine form of Eq. (3), because the initiation of an operating shear band is a non-steady-state event that is generally not accompanied by a back-flux of shear events. In other words, Eq. (12) describes the transient yield strength of a metallic glass prior to any deformation taking place and altering the glass structure.

Argon [40] observed that the development of local shear confined on a plane within a metallic glass is tantamount to the nucleation of a shear dislocation loop within a continuum solid, and wrote a rigorous expression for ΔG_s in terms of the elastic properties of the glass and the size of the critical event. Rather than assuming a simple linear superposition of strain energy and activation enthalpy (i.e. $Q - \tau V$, as used in the analysis of steady-state flow), this approach directly accounts for the fact that stress level influences the size of the critical shear event (i.e. V is a function of τ). Argon's analysis can be simplified to a form common in solid mechanics:

$$\Delta G_s \approx C_s \tau_s \Omega_s \left(1 - \frac{\tau}{\tau_s}\right)^2 \tag{13}$$

where $C_s \approx 4.6$ is a constant, τ_s is the athermal stress required to initiate the critical shear event, which occupies a characteristic volume Ω_s. In the simplest interpretation where the critical event is the activation of a single STZ, $\Omega_s \sim \Omega_o$ as defined above, with $\tau_s \sim \tau_o$ the stress required to activate an STZ in the absence of thermal energy. As pointed out by Argon [40], the athermal shear yield stress of metallic glasses is governed by a critical strain level as

$$\tau_s = \gamma_c \cdot \mu(T) \tag{14}$$

The critical strain proposed by Argon, $\gamma_c \approx 0.03$, remains remarkably accurate in the face of more recent analyses; Johnson and Samwer [36], for example, give $\gamma_c \approx 0.0267$ as a "universal" value for a number of metallic glasses at room temperature.

Rearranging Eq. (12), the temperature and strain-rate dependence of strength is more clearly discerned:

$$\tau = \tau_s - \tau_s \left[\frac{\ln(\dot{\gamma}_s/\dot{\gamma})}{C_s \tau_s \Omega_s} kT \right]^{1/2} \tag{15}$$

Further normalization is possible by expressing the critical energy barrier $\tau_s \Omega_s$ in terms of the glass transition temperature, giving an equation of the form:

$$\tau = \tau_s - \tau_s \left[D \cdot \ln(\dot{\gamma}_s/\dot{\gamma}) \cdot \frac{T}{T_g} \right]^{1/2} \tag{16}$$

where D is a dimensionless constant.

Physically, Eq. (16) suggests that temperature assists in overcoming the activation barrier for a critical shear event, and allows shear localization to occur at lower stress levels. However, the temperature dependence of strength is relatively weak, being captured by a power law with a temperature exponent less than unity. Fig. 10 reproduces a host of experimental data collected in Ref. [36], which illustrates the strength of metallic glasses in non-steady flow. Eq. (16) is fitted to these data with $\gamma_c \approx 0.037$ and $D \cdot \ln(\dot{\gamma}_s/\dot{\gamma}) \approx 0.2$, and can clearly capture the experimental trend. Recently, Johnson and Samwer [36] have derived a similar temperature dependence as Eq. (16), using the scaling behavior expected for a fold catastrophe for that of the critical shear event. Their derivation yields a slightly different exponent of 2/3 on the bracketed term in Eq. (16), which produces a similarly shaped best-fit trendline in Fig. 10.

The strengths reported in Fig. 10 were obtained during instrumented mechanical tests, and are all reflective of the transient, non-steady-state strength of the glass. At low temperatures, this value is essentially equal to the fracture stress (for unconstrained loading), because shear failure results rapidly once the yield condition is reached and local softening occurs. At high temperatures, these strength data represent the yield stress, which is usually closely related to the peak stress measured before softening occurs. At high homologous temperatures, the values of strength reflected in Fig. 10 do not represent the true load-bearing capacity of metallic glasses, because diffusive homogeneous flow can occur at lower stresses. In Fig. 10, this is illustrated by plotting the homogeneous steady-state flow law of Eq. (3) for four different strain rates using dashed lines; these curves are calculated using the best-fit parameters for $Zr_{41.2}Ti_{13.8}Cu_{12.5}Ni_{10}Be_{22.5}$ obtained in Section 4.1.1. A simple way to interpret the model trendlines in Fig. 10 is to regard the operational strength of the glass as the lower of either the solid or dashed line. Thus, at T/T_g greater than about 0.8, a transient higher stress denoted by the solid line may be achieved before the glass structure has had time to equilibrate under the applied strain rate, but, given time and/or continued deformation, the strength of the solid will drop to the steady-state value on the dashed line.

Eq. (16) also captures another important feature of the strength of inhomogeneously deforming metallic glasses, namely, a very weak scaling of strength with rate (as $-(\ln \dot{\gamma})^{1/2}$). In both uniaxial tension and compression, there is experimental support indicating that metallic glasses exhibit essentially rate-independent strength over at least six orders of magnitude, covering the entire quasi-static range and up to the range of low-velocity impacts. Fig. 11 summarizes a variety of experiments [159,181,185,189,190] focused upon this issue, and supports rate-independent fracture strength for both Pd- and Zr-based metallic glasses. As noted in Section 4.2.3.1, there is some evidence for softening at rates near

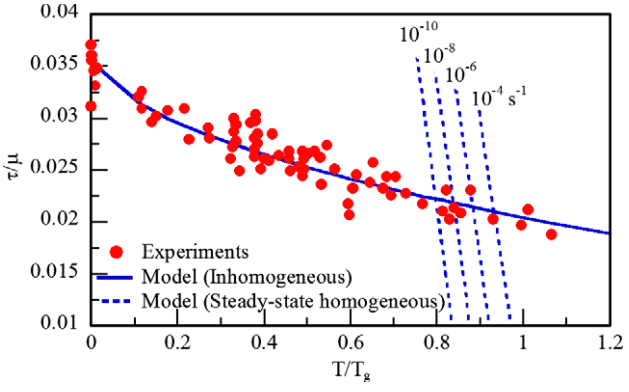

Fig. 10. Shear strength of metallic glasses as a function of temperature, on scales normalized by shear modulus, μ, and glass transition temperature, T_g, respectively. The experimental data here were collected by Johnson and Samwer [36] for a variety of glasses, and the solid line denotes the best fit of Argon's model (Eqs. (15) and (16)) assuming a constant strain rate. The dashed lines indicate the steady-state homogeneous flow stress from Eq. (3); viscous flow becomes strength limiting at higher temperatures and low rates.

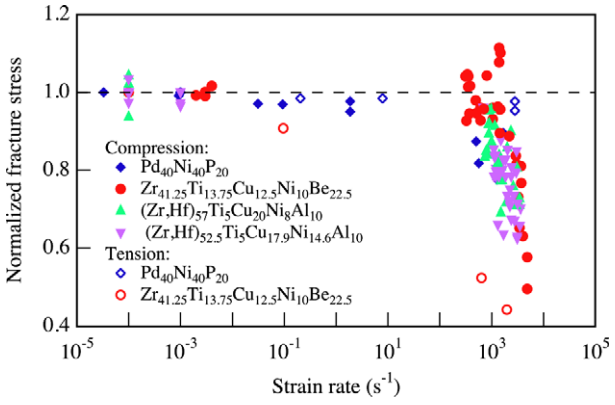

Fig. 11. Experimental measurements of fracture stress for a number of metallic glasses tested over a broad range of rates, after the compilation of Mukai et al. [159]. Over at least six decades of strain rate, strength is nominally rate-independent, although at the very highest rates tested to date ($\sim 10^3\ s^{-1}$) there is evidence for softening that is attributed to adiabatic shear localization.

or above $10^3\ s^{-1}$, which is believed associated with adiabatic heat generation.

4.2.3.2. Temperature and rate effects on shear banding and flow. Although the absolute strength of inhomogeneously deforming metallic glasses is only weakly temperature dependent and virtually rate-independent, the character of plastic flow beyond the initial yield point is strongly dependent upon these variables. In particular, it has been found that operating shear bands exhibit a characteristic rate or frequency, and changes in the applied strain rate relative to this value markedly impact the rate at which shear bands form and the amount of shear that they individually accommodate.

Fig. 12 shows a sequence of nanoindentation load–displacement curves acquired on a Pd–Ni–P metallic glass, at a series of different deformation rates for constant temperature (Fig. 12a) and at a series of different temperatures for constant rate (Fig. 12b) [92]. Most of these curves exhibit the same general shape, and the indentations acquire about the same maximum depth for a given applied load; this is reflective of a relatively constant hardness or strength, which is in line with the discussion in the previous section. (These data were all acquired at temperatures below the point where homogeneous flow can occur; cf. Fig. 10.) What changes more markedly with rate and temperature among these curves, however, is the degree of flow serration, as observed in the number and size of the discontinuities in the data. In particular, lower deformation rates promote more obvious flow serration, as does a modest increase in temperature.

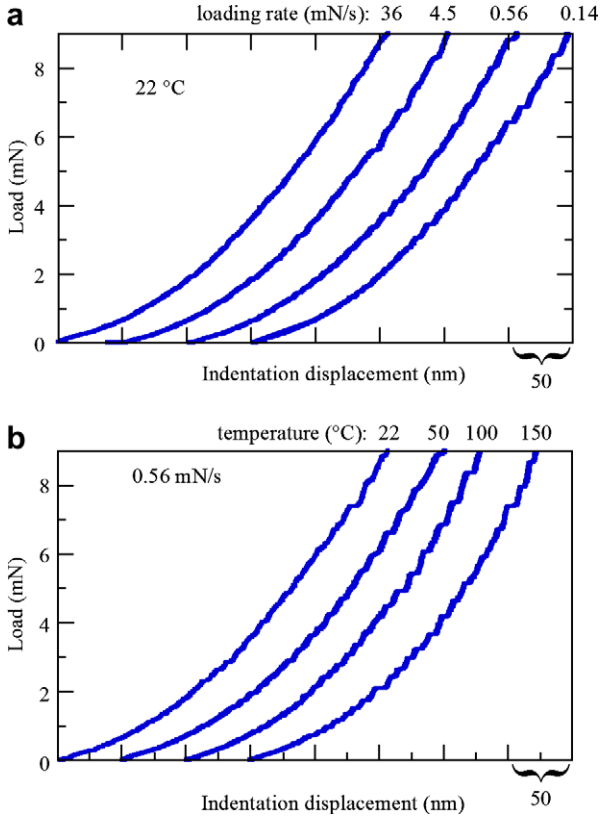

Fig. 12. Instrumented nanoindentation data from Ref. [92], illustrating the effect of (a) deformation rate and (b) test temperature on shear banding, as captured in serrated plastic flow curves. These data are for $Pd_{40}Ni_{40}P_{20}$, and illustrate that higher rates and lower temperatures lead to reduced flow serration, which translates into a higher number density of shear bands with smaller shear offsets.

The trends epitomized in Fig. 12 in indentation loading have also been observed in a variety of other experiments covering various modes of loading [6,8,152,153,162,172,191–194], including uniaxial compression [151,156,195]. A similar phenomenon has also been reported in simulations of slowly quenched two-dimensional amorphous systems [44]. The increase in flow serration with rate and temperature corresponds to a change in the shear banding behavior: more shear bands of generally smaller shear offset form at higher rates. This can be seen directly by examining the slip steps on deformed specimens, where higher loading rates are found to proliferate the spatial density of shear bands [189,191]. This trend is most easily seen for complex constrained modes of loading, such as indentation or crack opening. In these cases, the geometry guarantees that (i) runaway shear failure cannot occur and (ii) virgin material is continually accessed as the deformation proceeds and the plastic zone size expands. Therefore, the shear bands that form are relatively independent of one another, the frequency of their activation is directly correlated with their spacing, and deformation is essentially history-independent [162]. In contrast, in uniaxial deformation (constrained or unconstrained) the stressed volume is unchanging with strain, and each shear band to operate changes the structure of the solid; secondary shear localization events can occur on the same plane as the primary ones, and therefore plasticity does not always occur in virgin material [156].

The origin of the rate and temperature effects on serrated flow seen in Fig. 12 is attributed to a crossover in the applied strain rate and the intrinsic frequency of shear band formation [92,151,162]. At low rates a single shear band may operate to swiftly accommodate applied strain, while at high strain rates a single shear band apparently cannot keep up with the applied strain. Consequently, even as the first shear band forms, stress is not quickly relieved in the surrounding matrix and the yield condition remains satisfied in other locations; multiple shear banding events occur in separate locations in order to accommodate the applied strain. As suggested by Eq. (12), shear banding is associated with a characteristic frequency $\dot{\gamma}_s$, and once the yield point has been reached the exponential term in Eq. (12) is equal to unity; then strain can be accommodated at a maximum possible strain rate of $\dot{\gamma}_s$. Therefore, $\dot{\gamma}_s$ represents the critical strain rate separating the conditions under which shear bands operate individually ($\dot{\gamma} \leqslant \dot{\gamma}_s$) from those where multiple shear bands would be required to accommodate the applied strain rate ($\dot{\gamma} \geqslant \dot{\gamma}_s$) [92].

Based on experimental data such as those in Fig. 12a, the magnitude of $\dot{\gamma}_s$ is on the order $\sim 1\ s^{-1}$ for a variety of metallic glasses at room temperature [192]. However,

$\dot{\gamma}_s$ is also clearly temperature dependent (cf. Fig. 12b), and for this reason different glasses exhibit disparate rate effects when tested at room temperature, owing to differences in their homologous temperatures (T/T_g) [92]. Schuh et al. [92] considered the effect of temperature upon the kinetics of strain localization within the framework of the bifurcation analysis of Argon [40] described in Section 4.2.1. They demonstrated that it is more difficult, i.e. more applied strain is required, to induce shear banding events at higher temperatures. This is because the rate at which an operating shear band develops is governed by the mismatch in strain rate between the flow localization region and the surrounding matrix. At higher temperatures, it is more difficult to develop such a strain rate mismatch, as thermal energy contributes to accelerated flow of the matrix. At low temperatures, when one STZ is triggered in the matrix, localization can proceed quickly because there is no thermally activated accommodation mechanism. Diffusive accommodation opposes localization, and as a result shear bands need to be driven longer and to larger strains in order for flow to fully localize at higher temperatures. This is illustrated in Fig. 13, which shows the strain rate in a developing shear band $\dot{\gamma}_b$ in reference to that in the surrounding matrix $\dot{\gamma}_m$, as a function of the applied strain level.

Similar considerations to those described above explain why serrated flow and shear band spacing are strongly dependent upon applied strain rate and temperature. For example, from Fig. 13 it is directly seen that, for a constant applied strain rate, the shear strain accommodated by a single shear band at a homologous temperature of 0.6 is roughly half that accommodated by one at $T/T_g = 0.7$. Accordingly, twice as many shear banding events might be expected at the lower temperature, with a concomitantly closer spacing between the bands. Higher temperatures (and, by extension, lower strain rates) therefore promote large shear bands with wider spacings, and obviously serrated flow. Low temperatures and high rates yield a higher number density of smaller shear bands, i.e. flow appears more homogeneous and less serrated by virtue of a more finely distributed field of flow localization. An interesting corollary of this effect is suggested by Mukai et al. [189] and Sergueeva et al. [196,197], who observe that at low rates in tension fracture usually occurs on a single well-defined shear plane, whereas at high rates multiple shear bands may form simultaneously and lower the chance for fracture to occur on any one band. There is some suggestion that this might lead to apparently ductile flow at high rates [159,196,197], despite a lack of work hardening and negligible strain rate sensitivity.

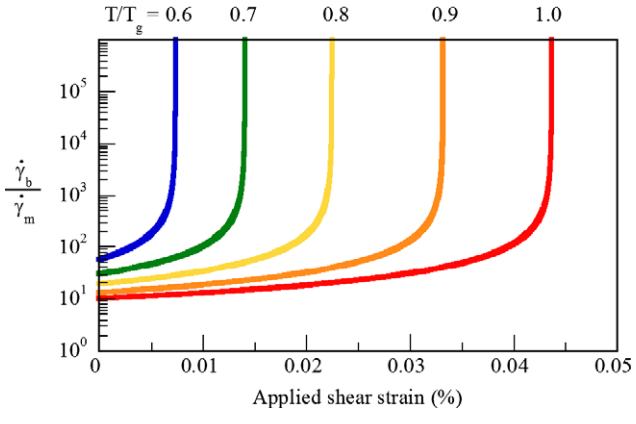

Fig. 13. Calculations from Ref. [92] showing the effect of temperature on strain localization. In the vein of Fig. 6a, this graph plots the strain rate in a forming shear band ($\dot{\gamma}_b$) relative to that in the matrix ($\dot{\gamma}_m$), as a function of the applied strain. Higher temperatures delay the development of the operating shear band by promoting flow of the surrounding matrix; shear bands must be driven to higher strains before the strain rate fully partitions.

4.2.3.3. Pressure effects. The dependence of plastic flow in metallic glasses on the applied pressure or the normal stress acting on the shear plane has been a topic of active research. This is due to the contrast that metallic glasses present with respect to crystalline metals, reflecting fundamental aspects of the mechanisms of plastic deformation. Plastic deformation in crystalline metals, which is generally controlled by the propagation of shear displacements via dislocation motion, is more or less exclusively dependent on the deviatoric part of the stress tensor (at least in some cubic or close-packed crystals). This is because hydrostatic stress causes only volumetric changes, and volume changes associated with plastic deformation in such crystals are usually insignificant [198]. Therefore, the flow stress in crystalline metals is often described by either the von Mises or the Tresca yield criteria, both of which consider only the shear (deviatoric) stresses [199]. The von Mises yield criterion is

$$\frac{1}{6}[(\sigma_1-\sigma_2)^2+(\sigma_2-\sigma_3)^2+(\sigma_3-\sigma_1)^2]=k_y^2 \tag{17a}$$

where σ_1, σ_2 and σ_3 are the principal stresses (in descending order of magnitude). The sole material parameter in Eq. (17a) is k_y, which represents the shear resistance of the material (i.e. shear yield stress). An equivalent form of the von Mises criterion can be written using the compressive yield stress σ_0 as the material parameter:

$$(\sigma_1-\sigma_2)^2+(\sigma_2-\sigma_3)^2+(\sigma_3-\sigma_1)^2=2(\sigma_0)^2 \tag{17b}$$

The Tresca criterion considers only the maximum shear stress and thus ignores the intermediate principal stress σ_2:

$$\tau_y=\frac{(\sigma_1-\sigma_3)}{2}=k_y \tag{18}$$

where τ_y is the effective yield stress.

It has long been known that disordered materials experience dilatation due to plastic deformation [200,201], so for metallic glasses it has been widely expected that the hydrostatic stress (or the normal stress acting on the shear plane) will play a role in determining the yield locus. At the most basic level, this can be reasoned in terms of the flow strength-to-modulus (σ_0/E) ratio. With increasing σ_0/E,

the pressure dependence becomes significant as local dilatation associated with microscopic plasticity events becomes significant. In crystalline metals, σ_0/E is small (of the order of 10^{-3}) as dislocations glide relatively easily and without much dilatation on closely packed (and thus widely separated) planes; pressure effects are often negligible. In contrast, metallic glasses have high σ_0/E ($\sim$0.02), so pressure effects on plasticity may be important. For this reason, yield criteria for metallic glasses often incorporate hydrostatic elements of the stress tensor. For example, the Mohr–Coulomb yield criterion takes into account the effect of the normal component of stress on the shear plane,

$$\tau_y = k_y - \alpha_n \sigma_n \tag{19}$$

where τ_y is the effective yield stress for shear on the shearing plane, k_y is the shear resistance of the glass (i.e. the yield stress in pure shear), α_n is a friction coefficient and σ_n is the normal stress on the shear plane. Note that a compressive normal stress on the shear plane opposes dilatation, increasing the effective yield stress; this dependence is described by the parameter α_n.

Several yield criteria with similar features to the Mohr–Coulomb equation have been used to analyze the multiaxial response of metallic glasses. For example, the pressure-dependent Tresca criterion has a form similar to Eq. (19):

$$\tau_y = k_y - \alpha_p p \tag{20}$$

where p is the hydrostatic pressure, $p = -\frac{1}{3}(\sigma_1 + \sigma_2 + \sigma_3)$ and α_p is the coefficient of pressure dependence. Finally, the Drucker–Prager yield criterion may be written as

$$\frac{1}{2}[(\sigma_1 - \sigma_2)^2 + (\sigma_2 - \sigma_3)^2 + (\sigma_3 - \sigma_1)^2]^{1/2} - \alpha_p p = \left[1 - \frac{\alpha}{3}\right]\sigma_0^c \tag{21}$$

where σ_0^c is the flow stress in uniaxial compression [199]. The latter two criteria are conceptually similar to that of Mohr and Coulomb (Eq. (19)), in that they explicitly incorporate a dependence on hydrostatic components of the stress tensor. What is more, with similar coefficients α these criteria describe essentially the same pressure dependence. In fact, based on measurements of uniaxial yield stress alone, it is quite difficult to discern an appreciable difference between a pressure or normal stress dependence if the values of α_n and α_p are comparable, although the shape of the yield surface is slightly different for each of the above cases. Additionally, both pressure and normal stress dependence may be included separately as two distinct terms in the yield condition, as proposed by Li and Wu [202] for polymers and Donovan [203] for metallic glasses.

A variety of experimental results show that the pressure dependence of plastic flow in metallic glasses is modest. The experiments of Kimura et al. [204] on amorphous $Pd_{78}Cu_6Si_{16}$ suggested that the von Mises yield criterion was appropriate, although they also noted a small pressure dependence in $Fe_{40}Ni_{40}P_{14}B_6$ that only became apparent at large hydrostatic pressures [205]. Bruck and co-workers also suggested that the von Mises criterion adequately described yielding in $Zr_{41.2}Ti_{13.8}Cu_{12.5}Ni_{10}Be_{22.5}$ [206]. On the other hand, Donovan used a Mohr–Coulomb criterion (Eq. 19) to describe yielding in $Pd_{40}Ni_{40}P_{20}$, and reported a normal stress dependence of α_n=0.11 [203]. A weak pressure dependence has also been reported for various amorphous alloys by Davis and Kavesh [207] as well as Lewandowski and co-workers [208,209] on the basis of mechanical testing with superimposed hydrostatic pressure. These authors also used the Mohr–Coulomb criterion, but reported smaller normal stress dependencies of $\alpha_n < 0.05$.

There have been some reports that the pressure dependence of flow is stronger than the work described above would suggest. For instance, Lu and Ravichandran [210] conducted confined compression tests on $Zr_{41.2}Ti_{13.8}Cu_{12.5}Ni_{10}Be_{22.5}$, imposing large radial confinement stresses (up to 2 GPa), resulting in hydrostatic pressure of $\sim$2.5 GPa. Their yield stress measurements could be well fitted with a pressure-dependent Tresca criterion (Eq. (20)), giving a pressure coefficient $\alpha_p \approx 0.17$ over a pressure range of 0.6–2.7 GPa. Flores and Dauskardt [211] used compression and notched-bar tensile tests to show that the average failure stress decreases with increasing mean stress (i.e. rises with pressure). By conducting an elastic analysis of the notched bars, they demonstrated the attainment of a critical mean stress at the notch root. Further, by modifying the free volume model of Spaepen [39] and Steif et al. [140] to include such pressure effects, they suggested that failure in metallic glasses may be considerably more sensitive to the tensile mean stress, or negative pressure, than to net compressive stresses.

Indentation methods have also been used to examine the pressure sensitivity of plastic flow in amorphous alloys. The inherent stability of this constrained geometry allows continued deformation at the yield condition, and a critical evaluation of the pressure sensitivity of amorphous metals is possible because of the multi-axial state of stress that prevails in the deformation zone. Vaidyanathan et al. [212] examined both the micro- and nano-indentation responses of $Zr_{41.2}Ti_{13.8}Cu_{12.5}Ni_{10}Be_{22.5}$ employing the instrumented indentation method wherein the load, P, and depth of penetration, h, are continuously measured. This experimental work was complemented by three-dimensional finite-element analysis of the Berkovich indentation with various constitutive relations. Their experimental and simulated P–h curves, which are reproduced in Fig. 14a, agree when the Mohr–Coulomb criterion was used with $\alpha_n = 0.13$, a value consistent with some of the experimental work described above. Further, Vaidyanathan et al. [212] showed that the shear band traces on the surface of the specimen and around the indenter follow the contours of effective Mohr–Coulomb stress (Fig. 14b and c).

Data from the work reviewed above is compiled as a function of stress triaxiality (which is proportional to $-p$) in Fig. 15 [19]. In this plot, states of net tension appear on the right, while those of net compression are on the left; the downward slope of the data is indicative of pressure-dependent strength. It is important to note that the various

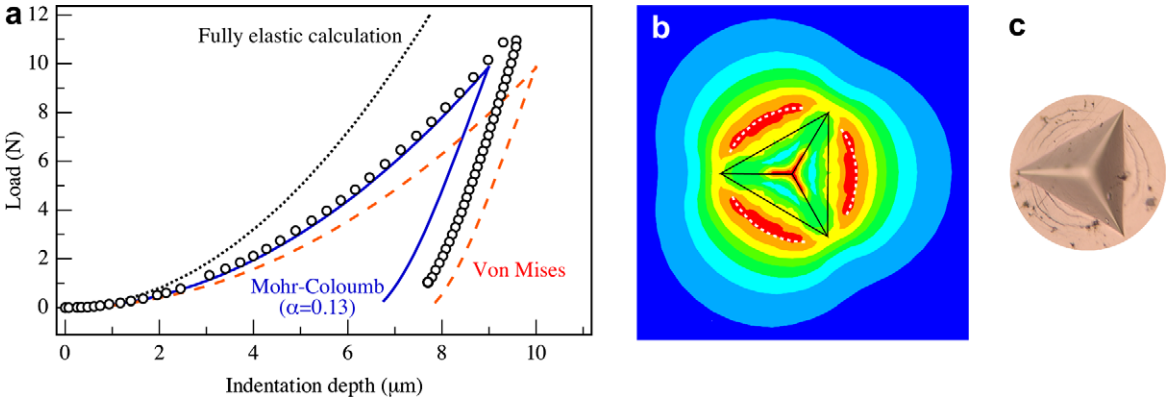

Fig. 14. Instrumented indentation data, acquired on a $Zr_{41.2}Ti_{13.8}Cu_{12.5}Ni_{10}Be_{22.5}$ metallic glass, which illustrate the pressure-dependence of strength [212]. In (a) the predictions of rigorous finite element calculations are compared with experimental data, using either the von Mises (Eq. (17)) or Mohr–Coulomb (Eq. (19)) yield criteria; the latter criterion with a friction coefficient $\alpha_n \approx 0.13$ is required to explain the higher-than-expected hardness (lower indentation depth). In (b) and (c), top-down views of the specimen surface near the pyramidal impression site are shown, to compare the predicted locations of slip steps from the finite-element calculations (b) with experimental observations (c).

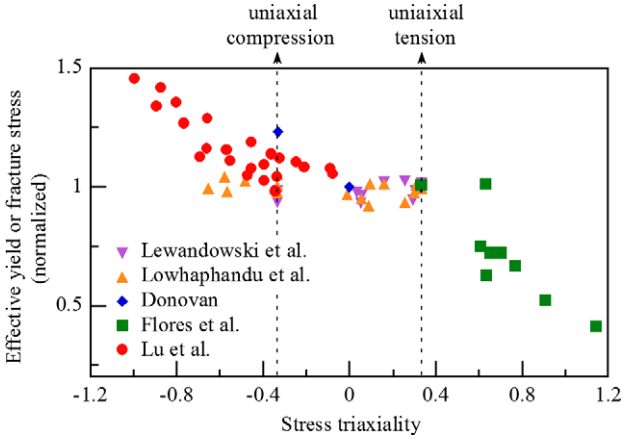

Fig. 15. Experimental data illustrating the effects of pressure on the yield/fracture stress of metallic glasses, after Ref. [19], with data from Lewandowski and Lowhaphandu [208], Lowhaphandu and Lewandowski [209], Donovan [203], Flores and Dauskardt [211], as well as Lu and Ravichandran [210]. Here the "effective" or von Mises equivalent strength is normalized by the value plotted as a function of stress triaxiality, which is proportional to the negative of the hydrostatic pressure.

studies collected in Fig. 15 are not directly comparable to one another, as they involve different geometries and alloys, and each data set has its own shortcomings. For example, the experiments of Lu and Ravichandran [210] may be affected by friction between the specimen and the confinement die used to produce high pressures, while the multiaxial tension experiments of Flores and Dauskardt [211] assumed yield at a point within a complex stress field. Nonetheless, the assembled data in Fig. 15 collectively capture the general trend revealed individually in these various works: the strength of metallic glasses is generally found to exhibit some degree of sensitivity to the applied pressure or stress triaxiality. The precise slope of the data varies widely in these studies, roughly over the range $\alpha_p = 0.03$–0.17, and there is significant scatter even within each individual investigation. For perspective, it is worthwhile to note that the pressure sensitivity of more strongly dilatant materials such as polymers (for which $\alpha \sim 0.2$ is common [213,214]) or granular packings (for which α is sometimes greater than 0.3 [199]) is much higher than that of metallic glasses. From a mechanistic point of view, however, the fact that a modest pressure or normal stress dependence is usually observed in amorphous metals points to an atomic-scale deformation mechanism that involves some degree of dilatation.

The atomistic origin of pressure and normal stress effects on yielding in metallic glasses was investigated by Schuh and Lund [18,215], who used atomistic simulations to examine the deformation characteristics of STZs. Using empirical inter-atomic potentials, they computed the yield surface of a metallic glass for biaxial loading, which is shown in Fig. 16. The yield stress from these data is clearly larger in compression than in tension, consistent with a pressure or normal-stress dependence. Fitting their results to the Mohr–Coulomb criterion, they identified a friction coefficient for STZ operation $\alpha_n \approx 0.12$, in reasonable agreement with most of the experimental data for metallic glasses described above. By extending their work to different configurations of STZs with different degrees of dilatation, Lund and Schuh [19] proposed that a reasonable range for α in densely packed glasses is 0.12–0.40, and suggested that the exact value is determined by factors such as the free volume distribution and the chemical and topological short-range order within the glass.

The pressure dependence of flow and fracture in metallic glasses leads to interesting manifestations in their mechanical responses. First, it leads to tension–compression asymmetry, with metallic glasses being generally stronger in states of net compressive loading than in tension. However, the reported differences are not large (typically less than 20%), and may be influenced by premature fracture in tension due to the presence of flaws. Second, the angle that shear band planes make with respect to the loading axis, θ, is a function of the normal stress sensitivity: $2\theta = \cot^{-1}(\alpha_n)$ for compression and $\cot^{-1}(-\alpha_n)$ in

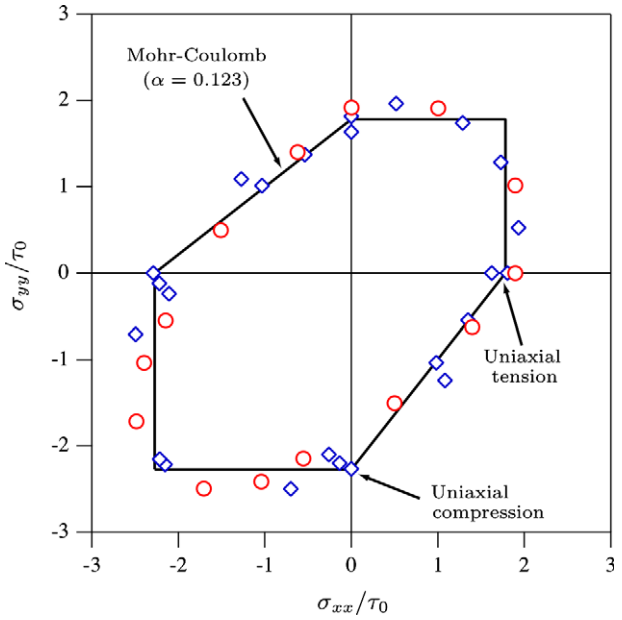

Fig. 16. A biaxial section of the yield locus for metallic glass simulated using atomistic techniques [18,215], which plots stresses along the x and y directions (σ_{xx} and σ_{yy}, respectively) in a normalized fashion. The simulation data (shown as points) reflect an asymmetry characteristic of a pressure dependence, as captured by e.g. the Mohr–Coulomb criterion (Eq. (19)) with $\alpha_n \approx 0.12$ (shown as a solid line).

tension. Therefore, for von Mises or Tresca solids, $\theta = 45°$, and flow occurs on the plane of maximum shear stress. Zhang et al. [216] as well as Lund and Schuh [18] have compiled the fracture angles reported in literature on different metallic glasses. While the fracture angle in tension is reported to be greater than 45° (ranging between 48 and 60° in most cases), the fracture angle in compression is less than 45° (between 40 and 44°). It is important to avoid confusion between the angle of fracture and that upon which shear bands initiate [217]; furthermore, end effects may also contribute to the selection of a specific shear or fracture angle. Nonetheless, these results generally support the view that flow and failure in metallic glasses is sensitive to hydrostatic components of the applied stress tensor. Not only do these observations support a Mohr–Coulomb-type yield criterion, they also show that fracture is more sensitive to the normal stress in tension vis-à-vis compression. The latter observation is expected as the local dilatation required to trigger STZs is promoted by tensile modes of loading, as is the nucleation of microvoids that initiates the fracture sequence. Such effects can be captured through secondary pressure dependencies incorporated into the flow rule for a glass that has already exceeded the yield criterion [161].

A third area where pressure dependence impacts mechanical response of metallic glasses is in fracture under complex stress states. Flores and Dauskardt [218,219] have compared the mode I and II fracture toughness of $Zr_{41.2}Ti_{13.8}Cu_{12.5}Ni_{10}Be_{22.5}$, and noted that the latter is ~4–5 times higher than the former. They suggest that, because normal tensile stresses lead to dilatation and hence increase the free volume of the material directly ahead of the mode I crack tip, flow and fracture occur at relatively lower loads, leading to lower toughness vis-à-vis mode II loading where the normal stresses are absent.

Perhaps the most significant effect of pressure-sensitive plastic flow behavior of metallic glasses is on their hardness, H. One of the attractive features of amorphous metals, in addition to high strength and large yield strain, is their high H values, which have direct relevance to tribological applications [5]. The constraint factor, $C = H/\sigma_0^c$ (hardness to compressive yield strength ratio), ranges between 3 and 4.5 for a variety of metallic glasses under fully plastic conditions (although a wider range has been measured [220]), whereas for crystalline metals it is $\leqslant 3$. This is due to the large compressive stresses beneath an indenter, which increase the flow stress via yield criteria such as those of Eqs. (19)–(21). The high pressure also affects plastic flow around the indenter. For example, Ramamurty et al. [221,222] have measured the plastic zone size δ_i around as well as beneath a sharp indenter by employing the "bonded interface" technique in Pd-based and Zr-based glasses. They showed that while the variation of δ_i with load P was in accordance with an "expanding cavity" plastic indentation model (which predicts $\delta_i \propto P^{1/2}$), the shear yield strength extracted from the experimental data was considerably larger due to the pressure-sensitive nature of the plastic flow.

The classical expanding cavity model, originally developed by Marsh [223] and Johnson [224] to relate hardness and deformation in crystalline metals, has been recently expanded by Narasimhan [225] to account for the pressure sensitive plastic flow in metallic glasses. Patnaik et al. [226] have performed numerical simulations employing the extended Drucker–Prager criterion (Eq. (21)) of Narasimhan, and compared it with experimental results obtained for $Zr_{41.2}Ti_{13.8}Cu_{12.5}Ni_{10}Be_{22.5}$ to show that the indentation strain vs. hardness data are captured for values of α_p in the range of 0.1–0.2. Most importantly, this work demonstrates that the high values of C observed in metallic glasses result from their pressure sensitivity (Fig. 17). More recently, Keryvin et al. [227] examined the constraint factor for elastic, elasto-plastic and fully plastic indentation conditions in both Zr- and Pd-based glasses using different types of indenters (conical, spherical and pyramidal) and showed that $\alpha \approx 0.1$ captures the experimental trends rather well over a wide range of indentation strains.

With an appropriate yield criterion and flow rule, continuum descriptions of metallic glass deformation are possible for arbitrary geometries, and the above consequences of pressure sensitivity can be readily captured through, e.g., finite-element simulations. For example, Anand and Su [161] developed a sophisticated elastic–viscoplastic constitutive model of pressure-sensitive and plastically dilatant materials. In this model, the pressure dependency arises explicitly through a dilatancy function and an internal friction coefficient, which are taken as input parameters. An

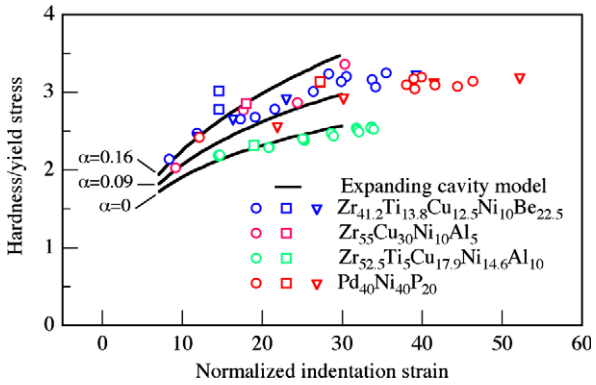

Fig. 17. The constraint factor, $C = H/\sigma_0^c$, is plotted as a function of the indentation strain associated with the hardness measurement, and normalized with the yield strain, after Refs. [226,227]. In order to match all of the experimental data, the plastic "expanding cavity" model must be evaluated with a pressure-dependent yield criterion, such as the Drucker–Prager criterion of Eq. (21), as shown by the solid lines.

important feature of this model is that the asymmetry and pressure dependence can arise not only through the yield criterion, but also through a nominally separate effect involving the flow rule. Finite-element simulations that implement this constitutive model accurately describe the metallic glass response under a variety of loading conditions (tension, compression, strip bending and indentation). Most importantly, the model also captures the shear band morphology for a given set of testing conditions.

To conclude this section, we observe that most of the research cited above is on room temperature behavior of metallic glasses. It might be expected that with increasing temperature the pressure sensitivity may become less pronounced as it becomes easier to activate STZs and hence σ_0/E drops markedly (at least once the transition to homogeneous flow has begun). Certainly experimental measurements will become easier at elevated temperatures high enough to promote stable homogeneous flow, where the confounding effects of shear localization and fracture can be avoided. However, this issue has not been examined yet.

4.2.4. Size effects in plasticity

In single-phase metallic glasses there is no microstructure per se, and the intrinsic structural length scales of the system are generally believed to be of atomic dimensions; the 10–100 atom volumes associated with STZ activity are a manifestation of this. For most experiments, the scale of the test (or specimen) is much larger than this intrinsic scale, and thus complications due to size-related constraints on the deformation mechanism are not expected. However, the process of shear localization introduces additional length scales to the deformation of metallic glasses, including the width of a shear band (cited as 10–1000 nm in the earlier discussion), its shear displacement and the characteristic spacing between shear bands. As a consequence of these scales, tangible size effects can manifest in mechanical tests.

As described in Section 4.2.1, for constrained geometries, shear bands are produced in a consecutive series that sequentially accommodates increments of applied strain. For such a mechanical test (e.g. a bending test), the time series of shear banding events maps to a spatial distribution of shear bands on the specimen surface, with a characteristic spacing. If one imagines the same experiment conducted again with similar geometry of a smaller size, then it is clear that the characteristic shear band spacing on the specimen surface must also decrease if the shear banding events are to individually accommodate the same amount of strain. As a consequence, shear band spacing is proportional to the characteristic specimen size, an effect noted recently by Conner et al. [163,228] and illustrated in Fig. 18. By the same token, the shear displacement of a single shear band (and the magnitude of the associated slip step) also increases with specimen size, an effect modeled by Conner et al. [163] as well as Ravichandran and Molinari [229]. This effect has important consequences for the fracture of metallic glasses in bending because fracture is generally believed to occur along a shear band once a critical level of displacement has been attained. This results in a scale-dependent fracture strain for metallic glasses, where thinner specimens may be bent to larger plastic strains without fracture and thicker plates are apparently brittle [163,228,230]. (More details on fracture and ductility are discussed in Sections 5.1 and 7.)

The "size effect" described above is basically geometrical in nature, and has been discussed without consideration of kinetic effects. However, as detailed in Section 4.2.3.2, shear band spacing and shear offset are also impacted by strain rate and temperature. This fact speaks to the possibility of a physical (non-geometrical) size effect in metallic glasses. As noted above, the characteristic strain rate associated with shear banding ($\dot{\gamma}_s$ from Eq. (12)) is believed to be of order $\sim 1\ s^{-1}$. By comparing this value with the magnitude of the Debye frequency ($\sim 10^{12}\ s^{-1}$), Schuh et al. [92] related $\dot{\gamma}_s$ to a characteristic

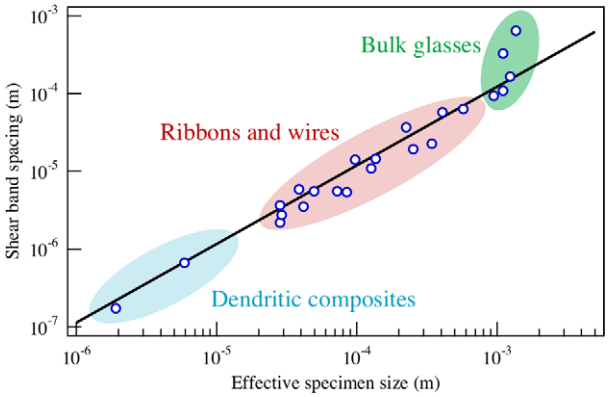

Fig. 18. Average shear band spacings are plotted as a function of characteristic specimen dimensions for a variety of metallic glasses (and some derivative composites) deformed in constrained modes of loading, after Conner et al. [163].

volume on the order of 10^8 atoms in size; they described this volume as representing the scale of the shear band once it is fully formed and "propagating". Assuming that at this point the operating shear band is roughly disk-shaped and has a thickness in the range of 10–100 nm, this calculation suggests a characteristic shear band scale on the order of 50–500 nm. Although the details of shear band formation are not yet fully resolved, such calculations suggest that the process of localization is characterized by intrinsic time and length scales larger than those of STZs and, indeed, large enough to measurably impact deformation behavior at small scales.

Both the geometric and intrinsic size effects described above may have practical implications for the toughness and ductility of structural bulk metallic glasses, and are certainly germane for applications involving thin films or micro-devices. What is more, there may be important interactions between the geometric and kinetic phenomena described above, although this has not yet been investigated in detail.

4.3. Deformation map

Based on the phenomenologies reviewed above, it is possible to construct a deformation map for metallic glasses, in the vein of classical deformation mechanism maps for polycrystalline materials [231]. Because virtually every aspect of glass deformation described above is captured through recourse to a single mechanism (STZ operation), it is not necessary to delineate regimes dominated by various deformation mechanisms; instead the term "mechanism" is dropped for clarity and the resulting "deformation map" focuses upon modes of deformation such as homogeneous and inhomogeneous flow. Spaepen first constructed a deformation map for metallic glasses in 1977 on the basis of his free-volume deformation theory [39], and the same essential form of the map remains valid. The original deformation map of Spaepen has been revisited by later authors [92,110,160], and here we will reconstruct the map and incorporate a number of recent observations in metallic glass deformation.

Throughout the following discussion, we use the material constants established in earlier sections (mostly for Zr-based metallic glasses), which are representative values that yield schematic deformation maps in reasonable quantitative units. Here we develop two complementary maps: one in coordinates of stress and temperature (Fig. 19a), which follows the form originally proposed by Spaepen [39], and a second in strain rate–temperature space (Fig. 19b) as delineated by Megusar et al. [160]. When stress is on the abscissa of the map, strain rate can be represented as a series of contours; conversely, contours of stress lie in the strain rate–temperature map. In both maps we present stresses as fractions of the shear modulus, which allows for at least approximate generalization to many glasses. In addition, absolute stress magnitudes are also presented for the specific case of $Zr_{41.2}Ti_{13.8}Cu_{12.5}Ni_{10}Be_{22.5}$.

The most fundamental element of the deformation map is the transition from homogeneous steady-state flow to inhomogeneous deformation, which occurs essentially at the point where the strain rates given by Eqs. (3) and (12) are equal. This boundary was considered by Spaepen [39] in the context of the free volume model, and by Megusar et al. [160] in the context of the STZ model. It separates a regime at high temperatures and low stresses or strain rates (where viscous homogeneous flow occurs) from one at lower temperatures or higher stresses and strain rates (where shear bands form); it is plotted with a thick solid line in the maps of Fig. 19. In the stress–temperature map of Fig. 19a, this line also directly indicates the operational strength of the glass prior to flow localization, which declines slightly with temperature. In the rate–temperature map of Fig. 19b, the shape of the transition curve is roughly parallel to a family of iso-stress contours that can be drawn in the homogeneous regime.

Within the homogeneous regime, sub-regions termed "elastic", "Newtonian" and "non-Newtonian" can also be differentiated on the maps. Given that homogeneous flow is thermally activated, there is, strictly speaking, no regime where it may be avoided; however, at strain rates below $\sim 10^{-12}\,s^{-1}$ it can be practically neglected, and this condition is used to define the elastic regime that appears in Fig. 19a. The Newtonian/non-Newtonian transition is more easily delineated by virtue of the condition $\tau \sim kT/V$ (cf. Eqs. (7) and (8)). At low strain rates of $\sim 10^{-5}\,s^{-1}$, non-Newtonian flow is generally observed at temperatures below the glass transition, with Newtonian flow above. However, the deformation maps illustrate that non-Newtonian flow as well as shear localization can be observed at high temperatures – even in the supercooled liquid regime – provided that the applied shear rate is high enough.

In the low temperature inhomogeneous regime, the strength of the glass is essentially rate independent; no rate dependence is reflected in the strength map of Fig. 19a, while in Fig. 19b vertical contours of constant stress may be drawn based upon the form of Eqs. (15) and (16) and the data in Fig. 10. The exception to this rate independence is at the highest applied strain rates of order $\sim 10^{3}\,s^{-1}$, where softening is seen due to adiabatic shear localization (cf. Sections 4.2.2 and 4.2.3.1, and Fig. 11). In the map of Fig. 19b, this softening effect is denoted schematically with dashed arrows.

Pressure dependence can be included through any of the roughly equivalent forms of Eqs. (19)–(21), leading to a family of iso-pressure contours for any given applied stress level. This is illustrated for a single value of applied pressure in Fig. 19a, where the logarithmic axis significantly downplays the subtle effect of pressure. In the rate–temperature map of Fig. 19b, the pressure effect is made more tangible, as shown by dotted lines added to the map for just a single applied shear stress ($\tau \sim 0.024\,\mu$). These calculations assume a pressure coefficient of $\alpha = 0.12$. (Presumably a similar pressure dependence can be expected to shift the curves in the high-temperature homogeneous regime, but

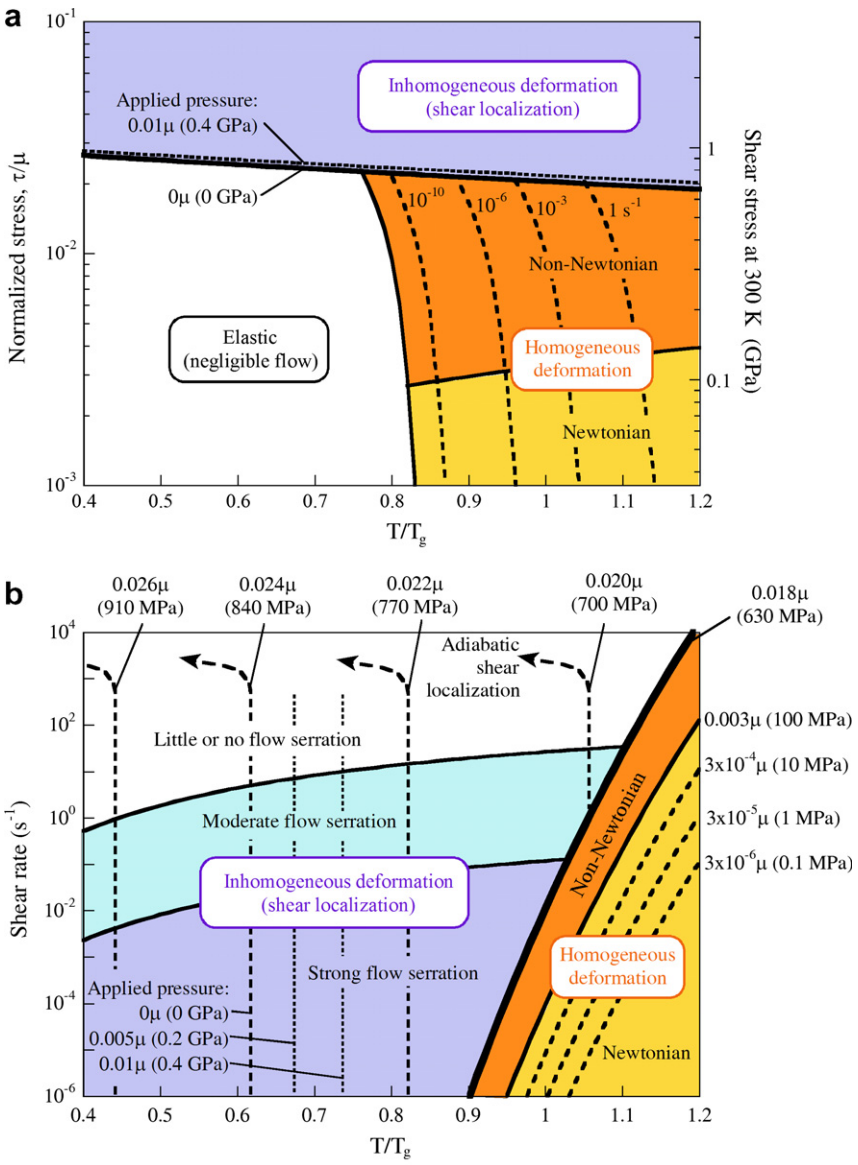

Fig. 19. Deformation map for metallic glasses in (a) stress–temperature and (b) strain rate–temperature axes. The main division on the map separates homogeneous deformation at high temperatures and low stresses/rates from inhomogeneous flow (shear localization) at lower temperatures and higher stresses/rates. In the homogeneous regime contours for steady-state flow are indicated, as is the transition from Newtonian to non-Newtonian flow. In the inhomogeneous regime, the effect of confining hydrostatic pressure is shown, and various degrees of flow serration are denoted in (b). The absolute stress values shown are for the specific glass $Zr_{41.2}Ti_{13.8}Cu_{12.5}Ni_{10}Be_{22.5}$.

as noted in Section 4.2.3.3, this speculation remains to be experimentally supported.)

The effect of applied strain rate upon shear banding events and serrated flow can also be represented on the rate–temperature deformation map (Fig. 19b), with contours of nominally constant shear band offset or interband spacing, or contours representing roughly constant degrees of flow serration. This behavior is governed by the kinetics of strain localization as described in Section 4.2.3.2 and illustrated in Fig. 13. Such contours are plotted with thin solid lines in the deformation map of Fig. 19b along the lines of the developments in Ref. [92], delineating in a semi-quantitative fashion sub-regimes (shaded differently in Fig. 19) in which relatively heavier or lighter flow serration is expected. According to these contours, higher rates and lower temperatures promote more finely spaced shear bands of generally smaller shear offset.

One important element of glass deformation not explicitly captured in these maps is the evolution of glass structure during deformation. For example, the homogeneous regime represented in Fig. 19 is based upon steady-state flow conditions and does not account for transients such as overshoots that are associated with structural evolution. In principle, a structural state variable could be included as a third axis to this plot [44] to allow a description of such transience. In the low-temperature regime the "strength" values can in most cases be regarded as yield stresses, which in unconstrained loading may be equal to the fracture

stress. However, these values are strictly representative only of the initiation of deformation, and do not presume anything beyond that point. The contours of shear band density or flow serration bear a similar caveat, in that they assume a constant glass structure, or a deformation mode that accesses fresh material with each passing shear band; evolution of glass structure within primary shear bands may affect the kinetics of secondary ones, but this is not accounted for in the map.

Fig. 19 also lacks explicit information about fracture behavior (which will be discussed in more detail in the next section). In the high-temperature regime, ductility is affected by the stress sensitivity (see Section 4.1), and the Newtonian regime allows higher extensibility as compared with the non-Newtonian regime. For inhomogeneous flow at low temperatures, ductility and fracture behavior are governed by geometric constraint, or by mechanisms which allow for the cessation of operating shear bands; these effects are covered in Section 7.

In spite of the above issues, the deformation maps assembled in Fig. 19 are a simple but informative view of glass deformation as a function of strain rate, temperature and stress. They may be used as semi-quantitative tools, e.g. for rationalizing observed trends with applied rate or temperature, or for comparing observed mechanical responses for different glasses tested at a common absolute temperature (room temperature) but at different homologous temperatures (T/T_g).

5. Fracture and fatigue

5.1. Fracture

Metallic glasses are, at best, quasi-brittle materials, because they do not possess sufficient intrinsic micromechanisms to mitigate high stress concentrations at crack tips. Contributing to this are an absence of strain hardening, and a lack of intrinsic crack propagation barriers such as grain boundaries. In spite of these limitations, some amorphous alloys do exhibit toughness values comparable to crystalline structural alloys; on the other hand, others are quite brittle, with characteristics similar to oxide or silicate glasses [81,102,232–236]. Such low toughness values will certainly prove a serious impediment to the widespread structural usage of amorphous metals, and in many cases may render them impractical. The toughness of a metallic glass is also considerably more sensitive to structural variability or relaxation than is strength, which introduces an additional element of uncertainty in their reliable use.

Despite the critical nature of these issues, the fracture behavior of metallic glasses has received relatively little attention. To at least some extent, this is due to the historical lack of sufficient quantities of material for valid fracture toughness measurements. In this section, we briefly review the available literature in order to understand the sources of toughness in amorphous alloys.

5.1.1. Fracture phenomenology

Due to the ribbon geometry of rapidly quenched glasses, early experimental work on fracture typically employed notched or unnotched bending tests to evaluate the fracture behavior of metallic glasses [204]. Mostly, these studies were directed at determining whether a particular metallic glass is ductile or brittle and how the fracture behavior depends on composition, processing (including quenching rates, structural relaxation and hydrogenation), and temperature [204,237]. Then as now, fracture was considered "ductile" if it involved large plastic strains, at least locally, due to inhomogeneous flow. In this case, the fracture surface morphology exhibits a characteristic "vein" or "river" pattern such as the one shown in Fig. 20a. In contrast, brittle fracture is reflected as a relatively smooth fracture morphology. However, higher magnification imaging shows that even the smooth fracture surfaces also have a vein morphology, albeit on a much finer scale, as shown in Fig. 20b [238,239].

Once unstable fracture begins, the material at the crack tip softens significantly. Although the heat evolution in a single shear band may be modest (see Section 4.2.2), the

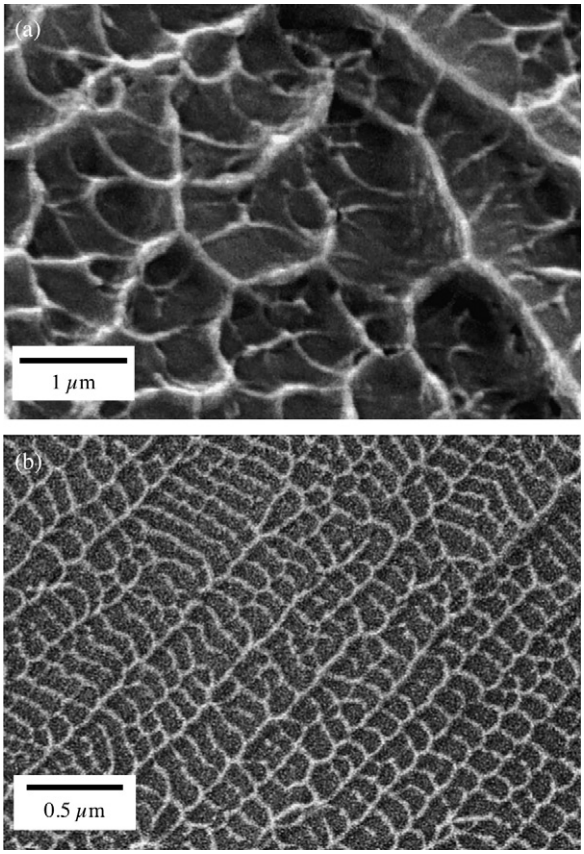

Fig. 20. Fracture surfaces of $La_{55}Al_{25}Cu_{10}Ni_5Co_5$ metallic glass from the work of Nagendra et al. [239], illustrating (a) the typical vein morphology for a nominally "ductile" fracture, as well as (b) a fine-scale view of the nominally smooth fracture surface obtained from "brittle" specimens; even in the brittle case a vein-like morphology is observed, but on a much finer scale.

final fracture event generally releases significantly more energy, and adiabatic heating is believed to contribute to softening during the fracture process. Evidence for this comes from the observation of molten droplets released during fast fracture, which is consistent with melting on the fracture surface [240]. During unstable fracture the material is fluid-like, and the scale of the vein pattern can be estimated by applying Taylor's meniscus instability criterion to determine the critical wavelength of the instability, λ_c:

$$\lambda_c = 2\pi\sqrt{\frac{-\gamma_t}{\zeta}} \tag{22}$$

where γ_t is the surface tension (which resists the fracture) and ζ is the pressure gradient ahead of the crack tip (due to the externally applied load) [241]. Therefore, the scale of the vein pattern on the fracture surface should, in principle, be indicative of the toughness of a given metallic glass. Indeed, recent experimental results show that the fracture morphology of "tough" glasses are rough with a deep vein morphology (Fig. 20a) whereas the brittle glasses have very shallow (nanometer scale) vein patterns (Fig. 20b).

Recently, Xi et al. [238] have demonstrated a correlation between the plastic zone size, r_p, measured from the fracture surfaces and that estimated from fracture toughness and yield strength data using

$$r_p = \frac{1}{6\pi}\left(\frac{K_c}{\sigma_y}\right)^2 \tag{23}$$

where K_c is the fracture toughness and σ_y is the yield strength [238,242]. A further illustration of this is shown in Fig. 21, which is a plot of the plane strain fracture energy, G_c, as a function of plastic zone size for a variety of metallic glasses. These values are calculated assuming that the same plane strain state is present in each measurement, using

$$G_c = \frac{K_c^2}{E(1-\nu)^2} \tag{24}$$

As the plastic zone size approaches the atomic scale (1-10 Å) the fracture energy approaches the "Griffith limit" for a truly brittle material, $G_c = 2\gamma_t \approx 2\ \mathrm{J\ m^{-2}}$. An important implication of Xi et al.'s observation is that the toughness of metallic glasses is apparently insensitive to the micromechanism of fracture and only depends on the scale of the plastic zone. This is broadly consistent with the ideas implicit in Eq. (22). However, the nature of the structural features that control the plastic zone size, as well as the connection between fracture and fundamental deformation processes (such as STZs), remain to be clarified by future research.

Metallic glasses exhibit a relatively sharp ductile-to-brittle transition, similar to that observed in some crystalline metals. Early work by Wu and Spaepen [243] and Yavari et al. [244] suggested that the transition occurs because the free volume drops below a critical level required for inhomogeneous plastic flow. Recently, Raghavan et al. [245] have employed impact toughness tests on notched bars (conventionally employed for evaluating the ductile-to-brittle transition in crystalline alloys) and confirmed that it is sensitive to the free volume content of the material. This is illustrated in Fig. 22, where impact toughness is plotted as a function of the degree of partial devitrification for a La-based metallic glass. Similar results are reported by other authors, demonstrating that annealing-induced structural relaxation and devitrification lower toughness [81,246,247]. Furthermore, it appears that the magnitude of the toughness jump across the transition temperature depends on the free volume, with fully relaxed (and hence low free volume) glasses showing particularly marked increases in toughness above the transition. Temperature also appears to play a role in determining the length scale of the plastic zone [247]. Again, however, the

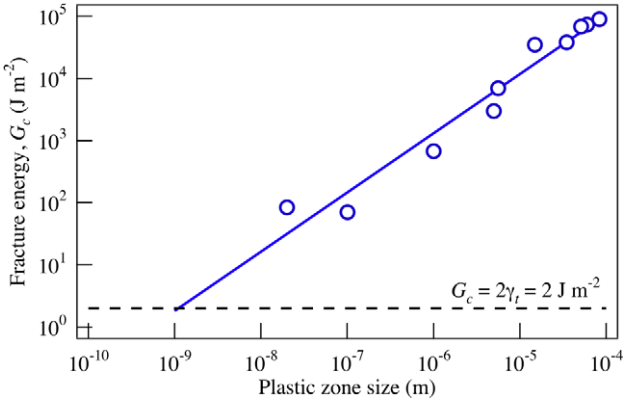

Fig. 21. Correlation between the fracture energy of Eq. (24) and the size of the plastic zone, for a variety of metallic glasses, based on data from Ref. [238]. The data appropriately converge to the "Griffith limit" for sufficiently small plastic zone sizes, where all of the fracture energy is used to create new surface.

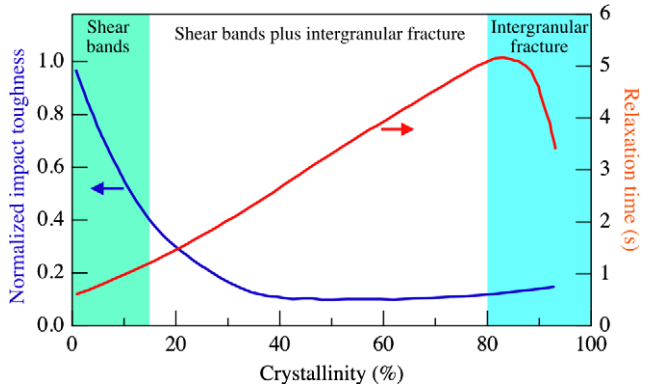

Fig. 22. Data from Ref. [239] illustrating the effect of structure on the impact toughness and characteristic structural relaxation time of $La_{55}Al_{25}Cu_{10}Ni_5Co_5$ glass. As the glass is exposed to higher relaxation times-at-temperature, the degree of devitrification (crystallinity) increases, which corresponds to higher relaxation times, lower toughness and a transition from "ductile" to "brittle" fracture modes.

precise role that free volume plays in enhancing fracture toughness remains to be elucidated.

5.1.2. Fracture mechanisms

The toughness of any material is determined by the intrinsic energy management mechanisms available to mitigate stress concentrations at crack tips. If the elastic strain energy concentrated in the small, nonlinearly deforming region ahead of the crack tip leads to instantaneous instability, fracture is brittle. On the other hand, if the material can "manage" the energy by dissipating it through various nonlinear processes (preferably involving a large volume of material, i.e. a large plastic zone), it will be tough. At a broad level, whether a crack tip is likely to get blunted or remain sharp as it propagates is determined by two competing processes, viz. shear flow or dilatational fracture, ahead of the crack tip [248].

In terms of micromechanisms of fracture, both homogeneous and inhomogeneous plastic flow mechanisms (discussed in Section 4) can help dissipate strain energy and toughen metallic glasses. High levels of tensile stresses at the crack tip (in mode I loading) lead to local dilatation and hence blunting through nonlinear viscous flow (if sufficient time is allowed) [140]. The characteristic relaxation time is a sensitive function of the condition of the glass, and increases significantly with structural relaxation or partial crystallization, leading to a precipitous drop in impact toughness, as shown in Fig. 22 [239,246,249]. Similarly, structural relaxation, which reduces the available free volume in an amorphous alloy, increases the relaxation time and in turn leads to embrittlement as crack-tip stress mitigation through viscous flow becomes less viable [246,249].

5.1.3. Fracture toughness of metallic glasses

Although there were a number of early attempts to study the fracture toughness of metallic glasses with nonstandard test methods (such as tensile testing of edge- or center-notched ribbon specimens) [236,250,251], the availability of bulk specimens enabled true fracture toughness measurements following standard methods. The early work on bulk metallic glasses indicated that some alloys (notably $Zr_{41.2}Ti_{13.8}Cu_{12.5}Ni_{10}Be_{22.5}$) could have mode I fracture toughnesses comparable to structural steels, with K_{Ic} in the range 30-68 MPa $m^{1/2}$ [233,234], and also established that severe embrittlement can occur upon crystallization. Lowhaphandu and Lewandowski [154], however, reported a lower K_{Ic} of ~19 MPa $m^{1/2}$ in fatigue pre-cracked specimens, and showed that the measured value is highly sensitive to the notch root radius – more so than in crystalline alloys of similar strength.

One possible origin for the discrepancy among fracture toughness values measured on glasses of nominally the same composition lies in the effect of plastic deformation (shear banding) and crack branching in the notch-root area, which effectively lowers the stress concentration factor [154]. In situ observations of crack-branching by Flores and Dauskardt (see Fig. 23) [155], and analysis thereof, showed that the stress intensity at individual branch tips is much smaller (~15 MPa $m^{1/2}$) than the far-field stress intensity factor (55–130 MPa $m^{1/2}$). Values at the lower end of the measured range (K_{Ic} ~ 10–20 MPa $m^{1/2}$) are consistent with the Taylor instability model described earlier, which assumes no plasticity or crack branching [241,247]. Thus, it appears that the wide variability in reported toughness measurements may in part depend on whether significant plasticity develops ahead of or around the crack tip. Other effects, such as compositional or structural variation, may also contribute [154,227,252].

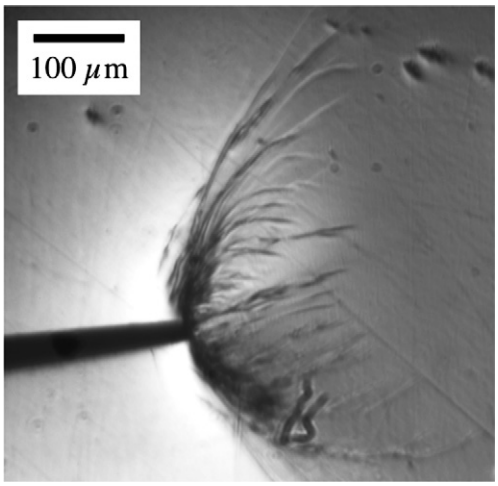

Fig. 23. An in situ photograph of crack branching in a $Zr_{41.25}Ti_{13.75}Ni_{10}Cu_{12.5}Be_{22.5}$ metallic glass loaded in mode I, at an applied stress intensity of $K = 116$ MPa $m^{-1/2}$, from the work of Flores and Dauskardt [155].

Flores and Dauskardt's work clearly demonstrates the important role played by extensive inhomogeneous flow (through shear bands) in imparting high toughness to metallic glasses. This observation is further supported by the studies of Lee et al. [253], who examined the notch toughness of a strip-cast Zr-based glass containing crystalline particles. The particles were found to aid in crack branching as well as in arresting propagating shear bands, thereby enhancing toughness. The effect of second-phase particles on plasticity in metallic glasses is also reviewed in more detail later in Section 7.4.

5.2. Fatigue

Like fracture, fatigue of amorphous metals was not studied extensively until relatively recently, mostly due to the lack of suitably large specimens for testing. Recent work has shown that the fatigue crack growth behavior is similar to that of other high-strength alloys, but the fatigue life behavior of amorphous alloys appears to be significantly different from that of crystalline alloys, for reasons that are not well understood. Complicating the situation are discrepancies in the results from various research groups, which may be due to differences in specimen geometry and preparation, as we discuss below.

5.2.1. Fatigue crack growth in the steady-state regime

Early work [236,251,254–256] on rapidly solidified metallic glass wires and ribbons established that, like crystalline alloys, steady-state fatigue crack growth obeys the Paris equation,

$$\frac{da}{dN} \propto \Delta K^m \tag{25}$$

where a is the crack length, N is the number of cycles, ΔK is the stress intensity range and m is a constant for a given material [257]. More recent work on bulk specimens that satisfy plane strain conditions confirm this, with $m \cong 2$ (although values from 1.7 to 4.9 have been reported) [234,247,258,259], comparable to that for ductile crystalline metals (and, notably, much lower than for oxide glasses) [257]. Amorphous alloys also show a fatigue threshold ΔK_{th} below which fatigue cracks do not propagate; typical values are $\Delta K_{th} = 1\text{-}5\ \text{MPa m}^{1/2}$, again comparable to many crystalline alloys [234,247,256–258,260,261]. Yet another similarity is the observation of fatigue striations on the fracture surface, the spacing of which can be correlated with the measured fatigue crack growth rate [236,262]. Together, these observations strongly suggest that the process of fatigue crack advance in amorphous alloys, as in crystalline alloys, involves irreversible plastic deformation that repetitively blunts and resharpens the crack tip [247].

5.2.2. Fatigue limit

Many crystalline alloys exhibit a fatigue limit – a stress amplitude S below which the material can be cycled indefinitely without failure – of about 40% of the tensile strength [257]. Early work on fatigue of amorphous alloys showed fatigue limits of 10–20% of the tensile strength [256,262]. More recent work on Zr-based glasses shows divergent results, with some groups reporting fatigue limits on the order of 5% of the tensile strength [247,258,259], but Liaw and co-workers reporting values on the order of 15–25% of the tensile strength [261,263–267] (Fig. 24). The reasons for the discrepancy are not entirely clear. Menzel and Dauskardt [268] attributed some of the difference to an incorrect stress concentration factor and a failure to properly account for the location of the crack initiation site for the data presented in Ref. [261]. Another difference is in testing technique; generally speaking, the lower values for fatigue life come from four-point bend tests, while the early results from Liaw et al. used a notched cylinder geometry, in which the volume of material probed is much smaller. A smaller specimen volume is less likely to have a defect that will cause fatigue crack initiation, and thus one might expect such specimens to show higher fatigue limits. But fatigue cracks appear to initiate easily (see below), and in any event the most recent work from the Liaw group [265], using a four-point bend test, reported results consistent with their earlier work (albeit on an alloy of different composition).

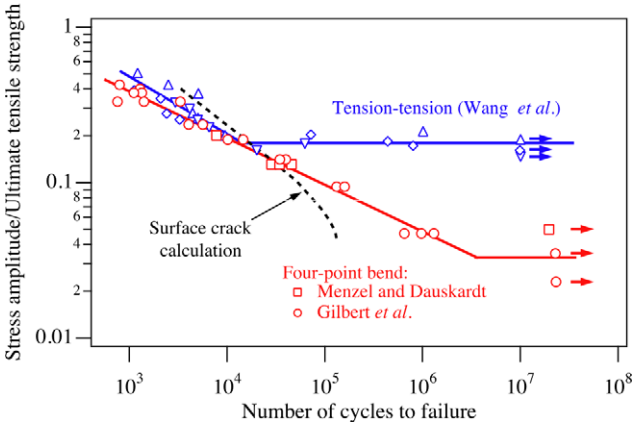

Fig. 24. Fatigue life (S-N) data for $Zr_{41}Ti_{13.8}Cu_{12.5}Ni_{10}Be_{22.5}$ metallic glass from two groups, using four-point bend [247,259] and tension–tension geometries [266,267]. Also shown is the calculation of fatigue life by Menzel and Dauskardt [259], which assumes that cracks nucleate early and grow at rates consistent with "long" fatigue cracks.

It may well be that the fatigue limit is sensitive to seemingly minor differences between the specimens. One possibility is the effect of residual stresses and structural relaxation on fatigue crack propagation. Bulk metallic glass specimens can have residual stresses which result from the difference in cooling rate between the interior and exterior of the casting [269,270]; residual stresses are known to affect fatigue life [257]. Another potential difference is in structural relaxation, again due to different cooling rates. Launey and co-workers recently reported that specimens taken from a 4.8-mm thick plate had a fatigue limit twice that of specimens taken from a 2.6-mm thick plate, a difference they attributed to greater structural relaxation in the thick plate due to slower cooling [271]. In this regard, it is interesting to note that the Liaw group's specimens [261,263–265] are machined from relatively small ingots, while those used by the Ritchie [247,258] and Dauskardt [260] groups were machined from cast plates (although naively one might expect the plates to be more fully relaxed and thus have higher fatigue limits). Finally, other effects may play a role as well, including things as diverse as the surface finish of the specimens, composition differences and the formation of an oxide surface layer [272]. Clearly, this is an area in which additional work is required to understand these effects; in particular, careful attention should be paid to the effects of residual stresses, relaxation and surface preparation.

5.2.3. Fatigue crack initiation

Using replica techniques to monitor the surface structure of fatigue specimens, Menzel and Dauskardt have recently examined the process by which fatigue cracks initiate on the surface of fatigue specimens [259]. They found that a shear band initiates first, after only a few loading cycles, oriented at ~49° to the direction of maximum stress. Such a shear band grows to a characteristic length (on the order of 40-70 μm) at which it suddenly transitions to a mode I form crack, oriented normal to the maximum stress. After this, the crack grows at a rate consistent with "long" fatigue cracks until final failure. Thus, the fatigue

life of nominally smooth specimens can be accounted for by considering only the growth of fatigue cracks, as shown in Fig. 24. This stands in surprising contrast to high cycle fatigue in crystalline metals, for which crack nucleation often accounts for ~80% of the fatigue life [257]. Apparently, once formed, fatigue cracks in amorphous alloys propagate with little hindrance, due to the lack of microstructure.

The significance of fatigue crack initiation suggests two routes for controlling fatigue failure in amorphous alloys. The first is that introducing microstructure (by making a composite) might limit growth of the small fatigue cracks and thereby improve fatigue performance. Unfortunately, the early work here is also in disagreement, with Flores and co-workers [260] reporting that the presence ~25% of a ductile dendritic phase increases the fatigue limit relative to a single-phase glass, and Wang and co-workers [266] reporting just the opposite for a similar material. Significantly, Flores et al. reported that the presence of the second phase did not contribute significantly to crack-closure effects and so the steady-state crack growth rate was not affected [260], again highlighting the importance of crack initiation.

A second approach to improving fatigue performance might be to introduce compressive residual stresses at the surface, such as has recently been done by shot peening [273]. The compressive stresses would presumably hinder the process by which surface shear bands transform to mode I cracks, as well as the growth of the small cracks themselves. In this regard it is interesting to note that the fatigue limit of specimens loaded in compression–compression is much higher than those which experience tensile stresses for at least part of the loading cycle [268]. This suggests that a compressive residual stress large enough to ensure that the surface of the component never goes into tension might dramatically enhance the fatigue performance of amorphous alloys.

An outstanding question is how shear bands can initiate at all at the low stresses associated with high cycle fatigue. Recent simulations suggest that free volume accumulates locally due to cyclic loading, leading to shear band formation and providing the kinematic irreversibility required for fatigue [274]. It is clear, though, that further critical experimental and theoretical work is required before the micromechanisms of fatigue crack initiation in amorphous alloys are fully understood.

6. Glass structure and mechanical properties

6.1. Role of structural relaxation

Since glasses are in metastable equilibrium, they traverse a series of lower energy states within the potential energy landscape when they are annealed at a temperature high enough for atomic motion, but insufficient for crystallization. This process, which is illustrated schematically in Fig. 25, is common to all glasses, and is referred to as structural relaxation; the lowest energy state that is non-crystalline is referred to as the *ideal* glass. In this state, the physical properties of the glass are the same as those of the equilibrium liquid extrapolated to the annealing temperature.

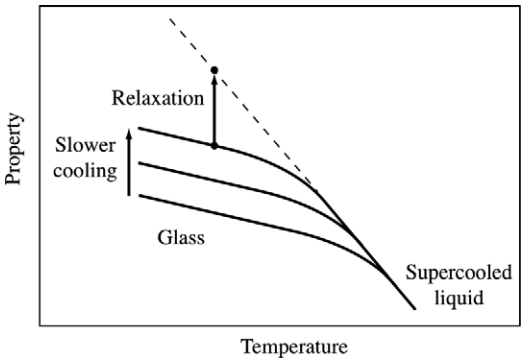

Fig. 25. Schematic relating the properties (i.e. density) of glasses to their thermal history, after Greer [80]. The ideal glass state is denoted by the dashed line, and true glassy alloys deviate from this ideality by a degree that depends upon the rate at which they were cooled from the melt. Relaxation by annealing allows traversal towards the ideal state at a constant temperature.

6.1.1. Mechanisms of relaxation

The atomic scale phenomena associated with structural relaxation can be broadly classified as either compositional (or chemical) short-range ordering or topological short-range ordering [80,275]. Topological short-range ordering refers to changes in the structure of the glass, particularly with regard to the arrangement of atomic sites. Changing the topological short-range order requires significant atomic mobility and is usually associated with irreversible structural relaxation due to annealing near the glass transition. Compositional short-range order, on the other hand, refers to how atoms of different elements are arranged on these atomic sites and is associated with reversible structural relaxation, often at temperatures well below the glass transition. Differences in the kinetics of these two kinds of relaxation were demonstrated by Koebrugge et al. [276], who showed that the kinetics of topological short-range ordering can be described by the free volume model, while those of compositional short-range ordering can be appropriately described by the activation energy spectra model. A detailed consideration of relaxation mechanisms and kinetics are beyond the scope of this article, but good reviews are available (e.g. Ref. [80]).

One of the major consequences of irreversible structural relaxation of metallic glasses is annihilation of free volume due to densification. For instance, Nagel et al. [277] employed positron annihilation spectroscopy as well as density measurements to study free volume changes associated with relaxation, and showed that the density of amorphous $Zr_{46.7}Ti_{8.3}Cu_{7.5}Ni_{10}Be_{27.5}$ increases by ~0.1% upon relaxation. For comparison, complete crystallization of this glass increases the density by ~0.8%. Furthermore, Nagel

and co-workers demonstrated that the annihilated free volume can be restored by heat treatment above T_g.

Another method for studying free volume changes with annealing is to monitor enthalpy changes near the glass transition using differential scanning calorimetry (DSC). Van den Beukel and Sietsma [278] interpreted DSC data in terms of free volume relaxation kinetics. Both the exothermic relaxation below T_g and the height of the glass transition peak are related to the free volume of the material [279]. For instance, Slipenyuk and Eckert [280] recently showed that changes in the enthalpy of a $Zr_{55}Cu_{30}Al_{10}Ni_5$ glass are linearly correlated with free volume changes (monitored through density measurements).

6.1.2. Mechanical properties and relaxation

Since the amount and distribution of free volume controls the plasticity in metallic glasses, structural relaxation has a pronounced effect on mechanical behavior [80]. For instance, densification associated with irrreversible structural relaxation leads to an increase in bulk modulus, as described earlier. In the context of this review, however, the most important changes are in the ductility and toughness, with structural relaxation leading to embrittlement of some (but not all) metallic glasses. Early work attributed annealing-induced embrittlement to a variety of factors, including reduction of free volume [243,281], the precipitation of crystalline phases [282] and phase separation [283]. These are not necessarily mutually exclusive, because the effect of crystallization or phase separation may be to reduce the free volume in the remaining amorphous matrix. More recently, Lewandowski and co-workers have shown that there is a correlation between elastic properties (and μ/B in particular) and fracture toughness, which can be manipulated via structural relaxation [81]; this is discussed in more detail in Section 7.3.

An example of the effect of free volume on embrittlement was provided by Wu and Spaepen [243], who examined the ductile–brittle transition temperature T_{DB} of $Fe_{79.3}B_{16.4}Si_4C_{0.3}$ amorphous ribbons and showed that the loss in ductility is due to free volume annihilation. In particular, they showed a direct correlation between T_{DB} and the fractional change in free volume (deduced from relaxation enthaply), and suggested that a minimum amount of free volume is necessary for ductility. Although they observed no phase separation in their glasses using small-angle X-ray scattering [284], Yavari pointed out that the scattering from phase separated zones in these alloys might be quite weak, and therefore better investigated by techniques able to detect light elements, such as field-ion microscopy [283].

Ramamurty and co-workers [249,285] demonstrated a precipitous drop in impact toughness with annealing in $Zr_{41.2}Ti_{13.8}Cu_{12.5}Ni_{10}Be_{22.5}$, and showed that the variation of both the impact toughness and relaxation enthalpy with annealing time obey a stretched exponential relaxation function as shown in Fig. 26, similar to that observed in the positron annihilation studies by Nagel et al. [277]. It

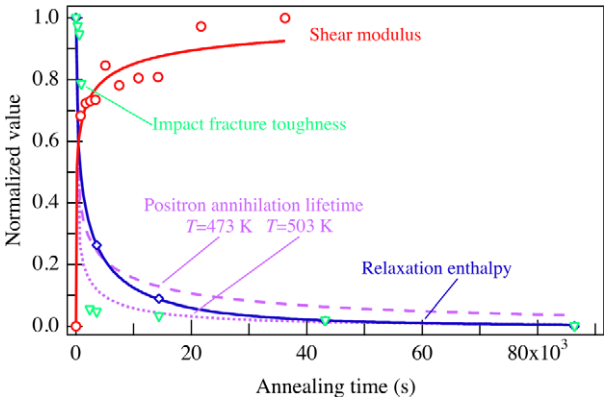

Fig. 26. Structural relaxation of metallic glass as a function of annealing time, as manifested in the measured relaxation enthalpy [249], positron lifetimes [277], impact fracture toughness [285] and shear modulus [286].

is interesting to note that the variation of shear modulus with annealing time reported by Lind et al. [286] shows a similar relationship. This is consistent with the recent observation that the intrinsic toughness of metallic glasses is associated with the ratio of shear to bulk modulus, μ/B [81], which will be discussed later in Section 7.3. Since changes in shear modulus with annealing are large relative to the corresponding change in bulk modulus (see Section 3), the correlation between the trends in Fig. 26 appears reasonable.

Reduction in free volume due to structural relaxation contributes to embrittlement in two ways. First, a loss of free volume increases the viscosity of the metallic glass (cf. Eqs. (6) and (3)), which in turn implies a loss of atomic mobility even in the solid. This may make stress relaxation by means of viscoplastic flow more difficult (e.g. at a crack tip region) and hence toughness is reduced. Second, free volume reduction apparently suppresses the shear banding susceptibility of annealed glasses. Murali and Ramamurty [249], by employing both micro- and nano-instrumented indentation techniques, showed that the number density of shear bands in relaxed $Zr_{41.2}Ti_{13.8}Cu_{12.5}Ni_{10}Be_{22.5}$ alloy is considerably lower than that measured in the as-cast glass. Since macroscopic plasticity in metallic glasses is mediated by shear bands, the size of the plastic zone at the crack tip gets reduced dramatically, contributing to the embrittlement [287]. This is also reflected in a dramatic change in the fracture morphology from a coarse vein pattern (Fig. 20a) to a smooth fracture surface with plasticity evident only on a much finer scale.

6.2. Characterization of shear bands

6.2.1. General observations

Much of the early work on shear bands involved inferences about their structure and behavior from macroscopic observations. For instance, shear bands subjected to chemical attack etch more readily than the surrounding undeformed material [288,289]. It was also observed that, if

interrupted, deformation continues on the same shear bands that were previously active [8,289]. Annealing below T_g eliminates both of these effects, and also makes possible greater degrees of plastic deformation by repeated rolling–annealing cycles [290].

A number of authors found explanations for these effects in terms of disruption of the atomic short-range order inside the shear bands, as originally proposed by Polk and Turnbull [52]. However, it is also possible that the observed effects are explicable by other mechanisms (such as residual stresses around the shear bands [291,292]), so direct structural characterization of the shear bands is desirable. This is a significant challenge, because shear bands typically comprise only a small volume fraction of a deformed specimen, and bulk characterization techniques average over both the shear bands and the (presumably undeformed) remainder of the material. Nevertheless, several attempts have been made using scattering techniques to study heavily cold-worked specimens [293–299]. All of these provide evidence for structural disordering, most often through decreased intensity and broadening of the first scattering maximum. It has also been observed that these structural changes can be reversed by annealing [300].

Characterization of individual shear bands is possible using transmission electron microscopy (TEM). Perhaps the most basic structural feature of a shear band is its thickness, which is of practical importance for determining the relative importance of thermal effects in deformation (see Section 4.2.2). TEM observations indicate that shear bands in metallic glasses are only 10–100 nm thick [301–305], which is quite small in comparison with adiabatic shear bands in crystalline metals, which are typically 10–100 μm thick [177]. However, it should be noted that all of the measurements for metallic glasses are from shear bands that were limited in extent, produced in foils or thin films either by bending or by in situ tension. Fully developed shear bands in bulk specimens may be thicker, but this is difficult to ascertain because shear bands create no microstructural changes that are readily observable in the TEM. It is true that the micron-scale features on fracture surfaces (Fig. 20a) are suggestive of softening in a thicker band, but the extensive plastic deformation associated with fracture is likely not representative of what happens in a shear band in the absence of fracture. Indeed, the surfaces of slip steps associated with shear bands on which fracture did not occur are rather smooth [174,306], again suggesting that the shear bands themselves are thin.

6.2.2. Dilatation and voids in shear bands

It is clear from abundant experimental evidence that both homogeneous and inhomogeneous deformation are accompanied by significant shear-induced dilatation of the structure, and indeed this dilatation is usually believed a contributor to plastic flow via reduced viscosity (see Section 4). It is interesting to note that shear-induced dilatation appears to be a universal feature of deformation of randomly packed structures; for instance, its importance in soil mechanics has long been recognized [200,201].

The most straightforward evidence for dilatation comes from measurements of density changes of metallic glass specimens as a result of plastic deformation. Density decreases of some 0.1–0.2% have been observed upon extensive inhomogeneous deformation due to wire drawing [307] and rolling [308,309], and indirect evidence of dilatation due to indentation has also been obtained from X-ray scattering [310]. These observed density changes are large compared with those experienced by crystalline alloys (which typically show only ~0.01% dilatation due to plastic deformation [311]) but small in comparison to many polymers. However, if, as is commonly assumed, deformation and thus dilatation are restricted to the shear bands, then by making reasonable approximations as to the number density and thickness of shear bands, one quickly arrives at the conclusion that the dilatation inside the shear bands themselves must be quite large (>10%) [308]. It is interesting to note that if the stored plastic strain energy in a metallic glass is similarly ascribed solely to the shear bands, the resulting strain energy density is also quite high [178]. Together, these observations raise the possibility that plastic deformation, even in the inhomogeneous regime, may not be restricted to the shear bands, or that shear bands are more diffuse than usually thought.

Free volume can also be measured indirectly but quantitatively by studying structural relaxation near the glass transition using DSC [278]. This technique has been used to measure changes in free volume during homogeneous deformation at elevated temperature [142]. The evolution of free volume due to inhomogeneous deformation can also be studied in this way, but the experiments are complicated by the small volume fraction of shear bands (even in heavily deformed specimens) and the possibility of relaxations other than that due to free volume (e.g. of residual stress). Nevertheless, measurements do show an increase in free volume with increasing degree of inhomogeneous deformation [306,312,313], consistent with the dilatation measurements described above.

Positron annihilation techniques are powerful tools for studying open volume regions in solid materials [314,315], and early work using the technique on metallic glasses showed that plastic deformation resulted in an increase in positron lifetime, consistent with a greater degree of open volume in the amorphous structure [299,309]. More detailed information, such as the type of electrons (valence or core) involved in positron annihilation, can be obtained from the broadening of the electron momentum spectrum, from which inferences can be made about the nature of the open volume regions. Suh and co-workers [316] observed a maximum in the fraction of positrons that annihilated with valence electrons as a function of temperature. They attributed this effect to the presence of both "shallow" and "deep" traps for positrons, with the shallow traps being identified as Bernal canonical holes in the amorphous

structure [317,318]. The deep traps were associated with open volume regions that are larger than Bernal holes (but smaller than vacancies in crystals). An intriguing possibility is that the deep traps may be associated with potential shear transformation zones of particularly low activation energy. Suh and co-workers did observe that the deep traps could be removed by annealing, while the shallow traps could not (as would be expected if they are inherent to the glass structure).

It is also possible to discern the local chemical environment around open volume regions from positron annihilation measurements. In zirconium-based glasses, for instance, the open volume sites tend to be associated with Zr, Ti and Al [319,320], while in copper-based glasses the open volume sites are associated with Zr and Cu [306]. The chemical ordering effect is enhanced by plastic deformation [320], but the implications of this for mechanical behavior are not clear. An interesting possibility is that this sort of indirect structural information could be combined with other, more direct techniques (such as X-ray scattering) to obtain more detailed understanding of the structural changes associated with plastic deformation.

The first detailed study of the internal structure of individual shear bands in metallic glasses was by Donovan and Stobbs [302], who examined shear bands in $Ni_{76}P_{24}$ thin films and $Fe_{40}Ni_{40}B_{20}$ thin films and ribbons. For shear bands formed in tension, they observed enhanced small-angle scattering in the shear bands, which they attributed to the presence of sub-nanometer-scale voids. They speculated that excess free volume, stabilized by the shear stress during deformation, coalesced into voids once the deformation halted. They did not see this effect for shear bands formed in compression. In both cases, however, they observed that the first amorphous halo in the diffraction pattern was broadened (suggestive of increased structural disorder) and shifted (indicating a change in the average interatomic spacing in the shear band), consistent with the scattering measurements described above. However, all of these effects were observed only near the specimen surface; shear bands that penetrated into the bulk were not observable at all.

Recently, more quantitative studies of individual shear bands have been performed using high-resolution TEM, as shown in Fig. 27. Li and co-workers [304,321] imaged voids of approximately 1 nm diameter in shear bands formed ahead of cracks in thin specimens of Zr-based metallic glasses. Again, it was suggested that the voids result from coalescence of excess free volume in the shear band once deformation stops. The nucleation of nanovoids has a large thermodynamic driving force [322]. However, it is not clear why void formation occurs in this case but not, for instance, during annealing of metallic glasses to remove excess free volume. Jiang and Atzmon [305] reported similar observations for shear bands formed on the initially tensile side of ribbons deformed by bending followed by unbending, but observed no voids on the initially compressive side of the same ribbons. This indicates that the hydrostatic component of stress affects void nucleation, an effect not considered in the purely thermodynamic argument for void nucleation [322].

6.2.3. Nanocrystallization in shear bands

Several groups have reported the formation of nanocrystals inside shear bands in metallic glasses. Chen and co-workers [323] observed fcc Al nanocrystals in bent ribbons of some aluminum-based amorphous alloys. Subsequently, other groups reported crystallization inside shear bands in bent ribbons [305,324], in shear bands resulting from nanoindentation [325,326] or microhardness testing [137], and as the result of ball milling or cold rolling of amorphous alloys [327–330]. An example of such nanocrystals formed during bending of an $Al_{90}Fe_5Gd_5$ glass is reproduced in Fig. 28, from the work of Jiang and Atzmon [305].

The mechanism by which crystallization occurs in shear bands is the subject of considerable debate. It is possible that localized heating of the shear band causes crystallization (see Section 4.2.2). The observation of radial diffusion profiles around the nanocrystals [331] is suggestive of thermally driven crystallization, and the direct observation of significant temperature rises inside shear bands [180] support this idea (see Section 4.2.2). However, as Demetriou

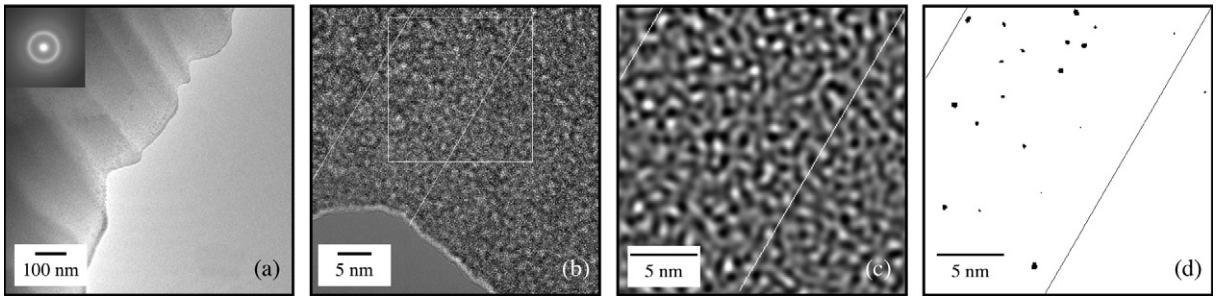

Fig. 27. A series of images from the work of Gu et al. [443] on $Zr_{52.5}Ti_{17.9}Cu_{20}Ni_8Al_{10}$ glass, examining the glass structure in the vicinity of a microcrack tip. In (a) and (b) shear bands are observed around the perforation site, in conventional (a) and high-resolution (b) images. In (c), Fourier filtering has been applied to the indicated portion of (b), and extremes in the intensity, which are related to regions of excess free volume, are represented in (d). In (b)–(d), the position of a shear band is identified by the lines, and it is clear that free volume has accumulated preferentially within the shear band. Additionally, nanoscale voids of ~1 nm size and less are observed within the shear band in (d).

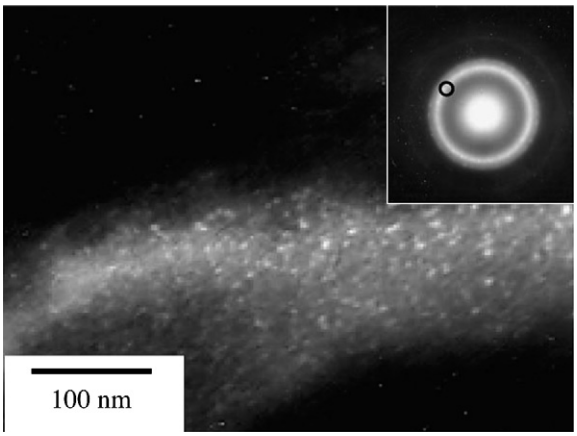

Fig. 28. A dark-field image of $Al_{90}Fe_5Gd_5$ metallic glass, from the compressive side of a bent specimen [305]; a high number density of nanocrystals can be seen.

and Johnson have pointed out [95], elevated temperatures alone are not a sufficient explanation, because the driving force for nucleation decreases with increasing temperature. If there are no pre-existing nuclei to grow, it is not clear that the rapid heating and cooling inside a shear band allow sufficient time for nucleation and thus crystallization. Again, the thickness of the shear band is important because it, along with the strain rate and the thermal conductivity of the alloy, determines the time scale available for crystallization.

Several experimental observations suggest that localized heating cannot be solely responsible for crystallization in shear bands. For instance, Jiang and Atzmon showed that, in bent ribbons, nanocrystals formed inside the shear bands on the side of the ribbon that was originally in compression, but not on the side originally in tension [305]. Since the strain rate and the associated heating are presumably similar for both sides of the same ribbon, the strain state itself must be important. Also, nanocrystals form in shear bands due to nanoindentation, even at very low loading rates where the expected temperature increase is small [325,326].

In their original paper, Chen et al. [323] attributed the nanocrystallization to extensive disruption of short-range order by shear, and not to temperature increases inside the shear bands. Similarly, others have proposed that the dilatation associated with shear deformation inside the band results in enhanced atomic transport [305,325], a viewpoint supported by evidence that plastic deformation and tensile strains greatly enhance atomic mobility in amorphous alloys [332–335]. Another possibility is that shearing affects the thermodynamics of glass-forming alloys, and not just kinetics [95,336]. In polymer solutions, for instance, there can be strong coupling between shear flow and concentration fluctuations [337–339], and simulations of sheared binary atomic mixtures suggest that a similar phenomenon could manifest in metallic glasses [336,340]. In particular, the non-equilibrium conditions associated with strong shear flow may shift the liquid miscibility gap and cause the system to phase separate, or alternatively may promote short-range chemical ordering among elements with negative heats of mixing. Since a large portion of the activation barrier for homogeneous nucleation in glass-forming liquids comes from the need to establish composition fluctuations [341], chemical ordering or phase separation induced by flow may significantly lower the activation barrier for crystallization. If correct, this idea may explain the observed dependence of nanocrystallization on alloy composition [305,323]. However, to date, the experimental evidence for shear-induced phase separation in glass-forming alloys is only indirect [342].

6.2.4. Shear band structure from simulations

Computer simulations provide unique insight into atomic-scale processes in materials, so it is natural to apply them to understand the internal structure of shear bands. Several early simulations showed cooperative atomic displacements associated with shear transformation zones [11,28,343], while more recent simulations are large enough to capture shear localization in some detail. For instance, Albano and Falk [344] saw subtle changes in short-range order associated with shear softening, and, in particular, in the alignment of atomic triplets (which is observable in the three-body correlation function but not in the pair correlation function). Interestingly, the alignment of these clusters could either increase or decrease with shear softening, depending on the degree of structural order in the original (as-quenched) glass. Shear localization was associated only with glasses quenched from the supercooled liquid state, which had a high degree of initial order and in which the order progressively decreased upon shearing. Shi and Falk also examined shear localization in light of the initial structure of two- [44] and three-dimensional [43] Lennard-Jones glasses. Models with an initial percolating k-core cluster [345] of quasi-crystalline short-range order showed shear localization at low strain rates; those without this order showed homogeneous deformation. In the former case, the quasi-crystalline order was disrupted in the shear band.

Bailey and co-workers have examined shear localization in model three-dimensional MgCu glasses [346]. They had some difficulty in obtaining localization; taking into account the results of Shi and Falk, this may be because Bailey's models were more rapidly cooled and thus had a lower degree of initial short-range order. However, they were able to force localization either under multiaxial loading (which suppressed the necking instability) or with a stress-concentrating notch. The results showed shear band thicknesses of $\sim$10 nm and dilatation of $\sim$1%, in good agreement with the experimental results described above, but changes in short-range order in the shear band were not described in detail. Simulations by Li and Li also showed shear band widths of $\sim$10 nm, but with somewhat larger dilatations in the shear bands [347]. They also noted that shear bands could form isothermally, due to the

disruption of short-range order, but that, if allowed to, the temperature in the shear band would rise quickly. This is consistent with the views described in Section 4.2.2 above that shear band formation is not primarily due to thermal softening.

In principle, the kinds of structural changes observed in these recent simulations could be observable experimentally. It may be that the scattering results described above, which show a general increase in disorder upon homogeneous deformation, are consistent with the simulations, but this has not been demonstrated. It may be possible to verify the specific kinds of changes in short-range order due to localization described by Falk and co-workers [43,44,344] in individual shear bands using TEM, although this would be a very challenging experiment. A promising development, however, is the recent application of fluctuation electron microscopy [348] to metallic glasses [349,350]. Unlike conventional scattering techniques, which only provide pair correlation information, fluctuation microscopy is sensitive to higher-order (three- and four-body) correlation functions. This may make it a powerful technique for characterizing structural changes in shear bands.

7. Distribution of shear bands and the pursuit of ductility

It is commonly assumed [163,229] that fracture initiates when the shear displacement Δu on a particular shear band reaches a critical value, Δu^*. The value of Δu^* depends on the alloy and the loading condition, but is typically taken to be on the order of tens of microns. If shear band propagation is not constrained in some manner, plastic strain accumulates on one dominant shear band which thus reaches Δu^* quickly, while the strain on any other shear band is still relatively small. Thus, fracture occurs with only limited macroscopic plastic strain and the ductility of monolithic metallic glasses – defined as plastic strain to failure in tension – is essentially zero in most cases.[2] However, if it were possible to limit the propagation of individual shear bands and thus distribute the plastic strain over many bands, then the onset of fracture might be delayed and significant macroscopic plastic strains could be realized. In this section, we discuss several approaches to this problem.

7.1. Geometrical constraints

As discussed in Section 4.2.1, the most obvious way to achieve larger plastic strains is to provide a geometrical constraint to shear band propagation. For instance, it has long been recognized that some metallic glasses can be plastically deformed by cold rolling or bending [8]. Similarly, uniaxial compression specimens with low aspect ratios can be deformed to large plastic strains [156–158]. But although these observations might be of interest for deformation processing of metallic glasses, the geometries are too restrictive to be generally useful for load-bearing applications. A somewhat more general approach is to constrain the shear bands by producing a laminated composite in which layers of ductile crystalline metal alternate with layers of metallic glass [351–354]. This prevents catastrophic shear band propagation and promotes formation of multiple shear bands, thus increasing the macroscopic plastic strain to failure.

7.2. Foams and nanoporous metallic glasses

As discussed in Section 5.1, the size of the plastic zone associated with a crack tip, r_p, increases as the square of the fracture toughness, K_c, and decreases as the square of the yield strength, σ_y. Brittle fracture occurs if r_p is less than the specimen size. As Ashby and Greer have pointed out [355], because metallic glasses are quite strong, r_p is small (~0.1-1 mm), particularly in comparison with the dimensions of many load-bearing components. In a metallic glass foam, however, the ligament size can approach the plastic zone size, allowing ductile deformation by bending of the ligaments and thus significant plastic strain in compression [356]. A high level of porosity coupled with the high yield stress of the glass gives these foams very high specific strengths, making them potentially attractive for applications requiring high impact energy absorption [357]. At lower levels of porosity (50%), metallic glasses can still show significant plasticity in compression (although not as large as that of foams with higher porosity) due to widespread initiation of shear bands at the pores [358]. Anisotropic distributions of elongated pores can be produced by homogeneous deformation in the supercooled liquid state [359]; compression tests in various orientations relative to the pores clearly show the importance of stress concentrations around the pores on shear band initiation.

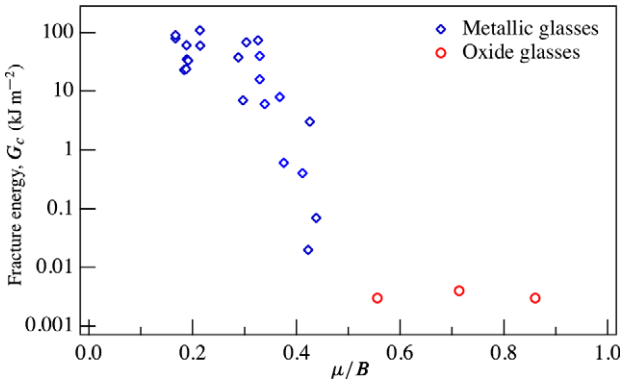

Fig. 29. Effect of the dimensionless ratio of shear and bulk moduli (μ/B) upon the toughness of various glasses, expressed in terms of the fracture energy G_c; after Lewandowski et al. [81].

[2] There is a tendency in some of the metallic glass literature to refer to "ductility" in compression; properly speaking, however, plastic deformation in compression is *malleability*.

7.3. Intrinsic approaches to distribute shear bands

Although some amorphous alloys can support significant plastic strains, other alloys appear to be inherently brittle. Lewandowski and co-workers demonstrated a correlation between the fracture energy G_c of metallic glasses and their elastic properties [81]. As shown in Fig. 29, amorphous alloys with $\mu/B < 0.41$ are tough, while those with $\mu/B > 0.43$ are brittle. This correlation can also be expressed in terms of Poisson's ratio, ν. For instance, Schroers and Johnson [360] reported that amorphous $Pt_{57.5}Cu_{14.7}Ni_{5.3}P_{22.5}$, which has a particularly large Poisson's ratio of $\nu = 0.42$ (and thus small μ/B), can show large plastic strains in compression and bending, and has a large fracture toughness ($K_c \approx 80$ MPa $m^{1/2}$) as well. It is interesting to note that such a correlation was first suggested by Chen [361], who proposed that metallic glasses with large ν would show large plastic strains to failure.

Lewandowski and co-workers [81] interepreted the correlation between μ/B (or ν) and fracture energy in terms of a competition between plastic flow on the one hand and fracture on the other, while Schroers and Johnson [360] rationalized it in terms of a competition between shear and dilatation. A low value of μ implies weak resistance to plastic deformation in shear [36], while a high value of B implies strong resistance to the dilatation required for mode I crack propagation. Both of these hearken back to Kelly et al.'s [248] interpretation of the similar correlation [362] in crystalline materials as a competition between plastic flow on the one hand and fracture on the other. For crystalline metals, the relationship between μ/B and fracture can be explained quantitatively in terms of plastic deformation processes near the crack tip [363], but no similar quantitative model has been developed for amorphous alloys. Still, the idea that a low value of μ/B favors extension of the shear bands over crack propagation has obvious intuitive appeal.

Recently, a surprising correlation between fragility (which is a property of the supercooled liquid) and ν (which is a property of the solid glass) was reported for a variety of glass-forming systems, showing fragility increasing with ν [364]. (Recall that a "strong" glass is one whose viscosity follows an Arrhenius law such as Eq. (3), decreasing exponentially or nearly so with temperature near T_g, while "fragile" glasses deviate from Arrhenius behavior by the additional factor captured in Eq. (6), and show an even more pronounced temperature dependence [109].) This observation prompted Egami [365] to suggest an alternative explanation of the correlation between toughness and ν. If the temperature of an operating shear band nears T_g, then the viscosity will drop more rapidly for a fragile glass (i.e. one with large ν) than for a strong glass. Egami went on to speculate that this would reduce the stress concentration driving shear band propagation in fragile glasses [365]. If true, this would make it more difficult to attain the critical shear displacement Δu^* and thus explain the increased toughness. However, it should be noted that the link between ν and fragility for metallic glasses has recently been called into question [366,367]. Furthermore, this model does not explain annealing-induced embrittlement, where the correlation between ν and fracture behavior is also observed [81].

There is, however, a more subtle way in which the elastic properties (and ν in particular) may influence fracture. An analysis of bending of thin plates shows that increasing ν reduces the spacing (and thus increases the number) of shear bands; for a given macroscopic plastic strain, therefore, the shear displacement Δu on each of the shear bands is reduced [229]. If the onset of fracture is determined by reaching a critical shear displacement Δu^* as described above, then an increase in ν should result in a larger macroscopic plastic strain to failure.

An additional useful point about these correlations is that it appears possible to predict, at least approximately, the elastic properties of a metallic glass based on an appropriately weighted average of the properties of its constituent elements [367,368] (although recent work [369] suggests that this may not always be true). Thus, as Lewandowski and co-workers pointed out [81], it might be possible to design a metallic glass composition (at least in terms of the majority elements) with the appropriate elastic constants and thus enhanced plasticity in mind. Of course, this must be balanced with the need to select an alloy composition likely to have good glass-forming ability in the first place.

Several groups have reported enhancements in plastic strain to failure (in compression) resulting from relatively minor changes in alloy composition [369–373]. While the elastic properties of these alloys have apparently not been investigated in detail, the changes in composition are small enough that significant differences in ν and μ/B are not to be expected. But noticeable differences in the appearance of slip steps on the specimen surfaces are apparent, suggesting an effect on shear band initiation or propagation which may be due to differences in structure [370,373]. The details of the mechanism by which structure influences shear band initiation and propagation remain, however, elusive.

7.4. Extrinsic approaches to distribute shear bands: composite structures

The desire to improve the ductility of metallic glasses has naturally led to the exploration of materials consisting of an amorphous matrix with one or more discontinuous crystalline phases. The two goals of making a composite are to promote initiation of a large number of shear bands (to distribute the macroscopic plastic strain over as large a volume as possible) and to inhibit shear band propagation (to reduce the shear strain on any one band and thus delay fracture).

Broadly speaking, there are three ways to produce a mixed microstructure consisting of an amorphous matrix with a crystalline second phase:

1. partial devitrification of a metallic glass (usually to produce a nanocrystalline phase);
2. precipitation of a crystalline phase during solidification, often with a dendritic morphology, with the remainder of the melt forming a glass ("in situ composites"); and
3. addition of second-phase particles to a melt prior to casting, casting of a glass-forming alloy around a preform of crystalline particles or fibers, or making amorphous/crystalline laminates [351,352] ("ex situ composites").

We use the generic term "metallic-glass-matrix composite" (or simply "composite") to refer to materials produced by any of these processes. An informative distinction can be also made based on the size of the particles relative to the characteristic length scale for shear localization and the morphology of the crystalline phase. To illustrate this, Fig. 30 draws together data from the literature on the strength and plasticity of a wide variety of metallic-glass-matrix composites [360,370,373–418]. The symbols for this figure are chosen to emphasize the form of the reinforcement: individual particles with diameters >1 μm [376–400], nanocrystals with diameters <1 μm [401–410], dendritic phases [411–416] or fibers [380,417,418]. Fig. 30a shows a figure of merit for strength:

$$\frac{\sigma_c - \sigma_e}{\sigma_e} \tag{26}$$

which is simply the strength of the composite (either yield stress or maximum flow stress) in compression (σ_c) represented as a fraction above (or below) the strength expected on the basis of a naïve rule of mixtures,

$$\sigma_e = V_p \cdot \sigma_p + (1 - V_p)\sigma_m \tag{27}$$

where σ_m and σ_p are the yield or flow stress of the matrix and reinforcement phases, respectively, and V_p is the volume fraction of the reinforcement "particles" (which we take to mean the second phase generally, irrespective of its morphology). Note that Eq. (27) is an ideal upper bound on composite strength, and strictly applies only to cases where the strain is the same in both phases. Our purpose here is not to present a rigorous or exact analysis of composite behavior, but rather to examine broad trends across the experimental literature on a relative basis; for this purpose the normalization of Eqs. (26) and (27) is reasonable.

An important caveat to Fig. 30a is that often the literature cited does not specify the properties of the reinforcement phase (σ_p), so in many cases – particularly for the nanocrystalline composites – we have had to estimate the yield strength of the reinforcement. This was done by using tabulated or estimated values of the shear modulus μ of the particles based on the composition (where given) and then making an estimate of the theoretical strength as $\sigma_p \approx \mu/15$. However, the broad conclusions drawn below are not particularly sensitive to these estimates.

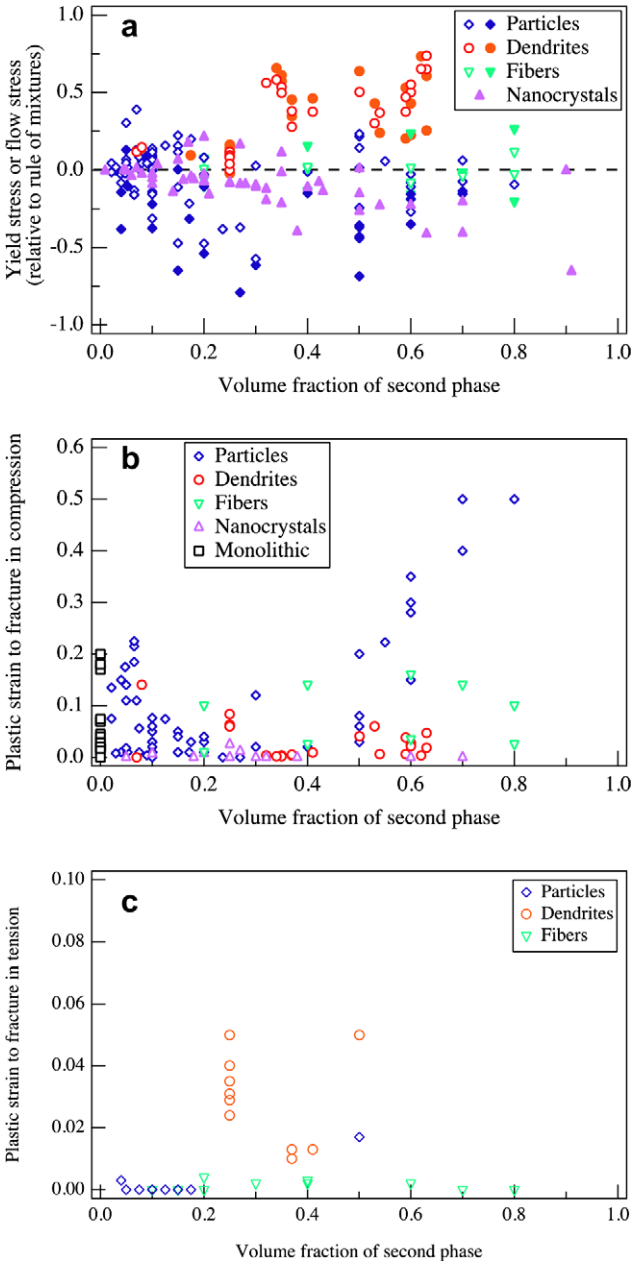

Fig. 30. A broad analysis of (a) flow stress, as well as strain to failure in both (b) compression and (c) tension, for a selection of dual-phase materials based upon metallic glasses with varying volume fractions of the second phase. In (a) the data are presented in a normalized fashion that is intended to allow a simple comparison among different types of reinforcement phases, including micron-scale dendrites [411–416], particles [376–400] and fibers [380,417,418], as well as embedded nanocrystalline reinforcements [401–410].

At low volume fractions of the crystalline phase ($V_p < 0.3$) the yield and flow stresses of composites of all types are clustered around the rule-of-mixtures value, indicating that the presence of the second phase does not significantly alter the macroscopic constitutive response of the amorphous matrix (with the exception that the plastic strain to fracture may be larger, as discussed below). At higher volume fractions ($V_p > 0.3$) the response of the com-

posite depends on the form of the second phase. The data for large particles and fiber reinforcement are still mostly distributed around the rule-of-mixtures line, but the data for dendritic (“in situ”) composites all lie above it, and the data for nanocrystalline composites are mostly below. (Note, though, that the effect of the uncertainty discussed above regarding the strength of the nanocrystals becomes more important at larger volume fractions.) Thus, the dendritic composites are relatively more effective at inhibiting macroscopic plastic deformation of the matrix than any of the others, an effect that may be related to the length scales associated with the dendritic microstructures, as relative to the characteristic length scales for plastic deformation of a metallic glass. We discuss this at greater length below.

Metallic glasses are inherently quite strong, so the point of making a composite is usually not higher strength, but improved ductility or toughness. Fig. 30b and c shows the plastic strain to failure in compression and tension, respectively, again for a variety of composite systems. Even in compression, none of the composites show more than about 0.2 (20%) plastic strain to failure up to volume fractions of ~0.5, although at higher volume fractions some systems do show larger plastic strains. Although nanocrystals do in some cases slightly improve the plastic strain to failure in compression, the effect is much smaller than for larger particles, for reasons that are discussed below.

7.4.1. Shear band initiation

In single-phase glasses, plastic flow is initiated in some locally perturbed region and localizes due to strain softening (see Section 4.2.1). Structural inhomogeneities and defects that introduce stress concentrations will thus naturally tend to promote shear band initiation, and limited plastic deformation can occur even at stresses below the macroscopic yield stress [396,419]. This can be used to advantage in composites, where the microstructure can be tailored with the goal of achieving a high density of shear bands.

There are three principal contributions to the stress concentrations around second-phase particles in a composite. First, significant residual stresses can be present in both phases (even in the absence of an external load) due to thermal mismatch strains that develop during processing of the composite [420,421]. Second, in response to an externally applied load both phases will deform elastically, and any difference in elastic properties between them will cause stress concentrations in the matrix [422]. Third, at higher loads, if the crystalline phase yields before the matrix, an additional contribution to the stress concentration results from the plastic misfit strain between the two phases [423].

Shear bands are initiated when the stress concentration in the amorphous matrix becomes sufficiently large that the appropriate yield criterion (see Section 4.2.3.3) is satisfied around the particles [396,424]. Depending on the relative properties of the two phases, however, the overall (composite) stress at which shear bands initiate may be too small to support the propagation of a shear front into the matrix. In this case, plastic deformation of the matrix will be localized around the particles until the overall stress reaches a level sufficient to drive a shear front (which will define the macroscopic yield stress, as typically determined on the basis of 0.2% plastic strain). The distinction between the stress required for localized yielding on the one hand and that required for shear front propagation and large-scale plasticity on the other can be seen either by careful measurement and analysis of stress–strain data, or by using in situ diffraction techniques to monitor the elastic strain in the particles and amorphous matrix [396,419,425].

7.4.2. Shear band propagation

The tendency for abrupt fracture due to shear localization, particularly under tensile loading, is a strong deterrent to using metallic glasses in structural applications. By analogy to dispersion and precipitation hardening of crystalline alloys, it has been widely anticipated that a composite microstructure might be used to inhibit shear banding events. As the data in Fig. 30a show, however, the strength of composites mostly follows a simple rule of mixtures, particularly at low volume fractions. Although the details depend on the specific system under consideration (which, for instance, determines the load partitioning between the two phases), this observation suggests that crystalline second phases are not effective barriers to the development of shear bands. This conclusion is supported by Fig. 30b and c, which shows that only very limited improvements have been made in plastic strain to failure.

Although our present understanding of operating shear bands is limited, perhaps it should come as no surprise that second-phase particles are, in general, not effective at disrupting operating shear bands. The shear flow stresses of monolithic glasses are quite high ($\sim\mu/30$), and ahead of a propagating shear front there must be a stress concentration. The details of this stress concentration are not yet known, but presumably it has the same form as that of a dislocation in a crystalline material,

$$\sigma \approx \frac{\mu \cdot \Delta u}{r} \tag{28}$$

where r is the distance ahead of the propagating shear band. The magnitude of the shear displacement Δu is not known; slip offsets of 1 μm are commonly observed on slip steps of specimens after mechanical testing, but it may be that these offsets are the result of multiple shear banding events on the same shear band. In any event, the existence of this stress concentration means that a propagating shear front would exert force on a particle ahead of it [426]. In some cases, a particle can deflect a shear band that intersects it [427] if the shear displacement is small. However, in many cases, the same flow stress under which a shear front propagates through the amorphous matrix appears to be sufficient to either cleave or plastically deform second-phase particles without the need for higher stresses.

Observation of deformed specimens by electron microscopy does show that operating shear bands can, in fact, induce localized plastic deformation in ductile second-phase particles [303] or fracture brittle particles [428]. An operating shear band can also be deflected by a crystal without intersecting it, due to the interaction between the stress concentrations associated with the shear band and with the crystal [428]. Interestingly, stronger such interactions were observed under compressive stresses than tensile stresses, which may partially explain why it seems easier to enhance plastic strain in compression than in tension in these composites.

Another effect of limiting the shear displacement on a shear band is that it presumably limits the maximum temperature achieved in the shear band and hence the thermal softening [102]. This may delay catastrophic fracture and thus contribute to enhanced plasticity.

In contrast to the other reinforcement morphologies, the dendritic composites [411,412,415,429–431] do achieve high strengths and, interestingly, these are the only composites for which the plastic strain to fracture in tension is similar to that in compression (Fig. 30b and c). The behavior of the dendritic composites is likely related to the microstructure, as illustrated in Fig. 31. Within each dendrite colony, the dendrite arm spacing is on the order of 10 μm, with somewhat coarser features between colonies. This changes the stress concentration in the amorphous matrix and thus influences shear band initiation. It would be interesting to investigate this by finite-element simulations making use of the actual microstructures [396]. Another effect of the dendritic microstructure is that newly formed shear bands are likely to intersect a dendrite arm before propagating very far, perhaps even before they achieve steady-state propagation, making the dendrite arms more effective barriers to shear front propagation.

Unfortunately, only a few alloy systems are known to produce amorphous matrix composites with a ductile dendritic phase, and even in those the range of possible compositions is limited. The nucleation and growth of the dendrites is quite sensitive to the cooling rate during casting, leading to significant variations in microstructure [432]. Furthermore, in the systems studied to date the dendritic phase is considerably softer than the amorphous matrix, requiring significant sacrifices in strength to achieve even modest gains in ductility.

If the presence of a second phase promotes plasticity in a metallic glass matrix composite, it is natural to suppose that the fracture toughness or fracture energy might be increased as well [102]. The limited data available do suggest that this is the case for dendritic in situ composites [260,411,412,415] and ex situ composites with ductile particles [433]. However, mixed crystalline/amorphous microstructures with brittle crystallites (produced by partial devitrification or due to cast-in crystallites) have lower fracture toughnesses than the corresponding single-phase glasses [234,239,434,435].

7.4.3. Nanocrystalline composites and "strain hardening" metallic glasses

Implicit in the above discussion is the assumption that the second-phase particles are larger than the characteristic dimensions associated with plasticity in the amorphous matrix, but this is not necessarily true if the second phase is nanocrystalline. In the case of shear band initiation, a recent estimate for the diameter of a disk-shaped critical shear band nucleus puts it on the order of ~0.5 μm [92] (see Section 4.2.4). Since the spatial extent of the stress concentration around a particle scales with the particle size, even if the magnitude of the stress concentration around a nanocrystal is large, it might not extend over a region large enough to permit nucleation of a shear band. Of course, at all but the lowest volume fractions the stress concentrations from neighboring nanocrystals may overlap, so the net effect may still be to favor shear band initiation. The data in Fig. 30 do suggest that nanocrystals may slightly enhance shear band initiation, as reflected in the slightly decreased strength (relative to a rule-of-mixtures) and increased plastic strain in compression.

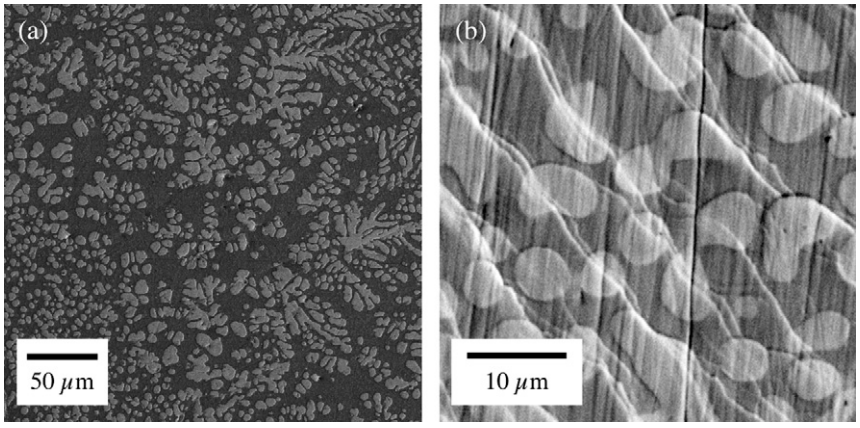

Fig. 31. Scanning electron micrographs from the work of Hays et al. [415], illustrating the microstructure of an in situ dendrite-reinforced composite with a Zr-based glass matrix. In (b) a series of shear band slip steps are seen, and these are clearly affected by the presence of the crystalline dendrite particles.

Pre-existing nanocrystals apparently have little ability to disrupt shear band operation, and thus do not contribute to improved tensile ductility. Such disruption is probably dependent upon the the thickness of the shear band, variously estimated as 10–100 nm but possibly as large as 1 μm (see Section 6.2). There is no particular reason to expect that individual particles smaller than this will have any effect on shear band propagation, although collectively a reasonably large volume fraction of nanocrystals might affect the rheology of the flowing shear band [164].

In addition to the direct effect of nanocrystals on plastic deformation, the process of producing nanocrystals by devitrification may affect the amorphous matrix in two ways. Nanocrystals generally have a composition different from that of the matrix, since kinetic limitations associated with diffusion are what limit their growth. This necessarily requires that the composition of the matrix change as well, possibly influencing its mechanical behavior. For example, the increased hardness of Al-based nanocomposites can be explained on the basis of composition effects, without the need to invoke any effect of the nanocrystals on the shear bands [407]. A second consideration is that the annealing process (often carried out above T_g) will change the state of structural relaxation of the matrix; this is often interpreted as a reduction in free volume, but it may be better expressed as a change in the fictive temperature of the glass [365].

Recently, a number of papers have appeared reporting the observation of large plastic strains to fracture (>0.5 in compression, in some cases) and apparent strain hardening in several alloy systems [164–168]. Particular attention has been paid to binary Cu–Zr alloys, long known to form glasses by rapid solidification but also recently reported capable of forming glassy rods of up to 2 mm diameter [436–438]. The structure of these alloys can be quite sensitive to the cooling rate during casting [439], which might explain some of the apparent disagreement as to whether they are fully amorphous or partially nanocrystalline. It has been reported that growth or coalescence of nanocrystals can occur in shear bands, either of which might increase the flow stress of the material in the shear band [164,440]. In addition, Chen and co-workers have reported nucleation of nanocrystals inside shear bands in amorphous $Cu_{50}Zr_{50}$, and proposed that this leads to strain hardening, explaining the large compressive strains to fracture [441].

On one level it is clear that these glasses do not strain harden, at least not according to the conventional definition, because shear localization is itself direct evidence of strain softening. It is possible, however, that nanocrystallization might raise the flow stress inside an operating shear band, thereby causing flow in the shear band to cease. But the flow stress in an active shear band drops dramatically; to reverse the shear localization, the flow stress would need to approach that of the surrounding (undeformed) material. This seems unlikely unless the density of nanocrystals in the shear band becomes quite high, and even then it is not clear that this would be sufficient. An alternative explanation for the observed behavior of these materials is more closely related to the initiation of plastic flow. Shear bands form in response to an imposed strain and cease flowing when the strain has been accommodated (see Section 4.2.1). In response to continued loading, the additional strain may be accommodated by initiating new shear bands or by reactivating new shear banding events on previously formed shear bands [8,171]. In practice, much of the deformation appears to happen sequentially on a relatively small number of "primary" shear bands (the number and spacing of which may be influenced by the loading geometry). It is believed that existing shear bands are reactivated because the prior deformation has altered the structure of the material in the shear band, lowering its flow stress [52]. In the case of the "strain-hardening" glasses, however, the presence of nanocrystals in the shear bands may effectively raise the flow stress, preventing their reactivation and forcing initiation of new shear bands elsewhere in the material. This would be consistent with the observation of a much higher density of slip steps on the surfaces of these glasses [164–166,168]. Furthermore, since shear bands are believed to initiate at defects or other structural inhomogeneities, as the most favorable initiation sites are used up the stress required to initiate new bands will increase. In this model, the apparent "strain hardening" is thus an effect of the difficulty of initiating new shear bands, and only indirectly results from the increased flow stress in shear bands due to nanocrystallization.

8. Conclusions and future research directions

In writing this overview, we have emphasized that the broad trends observed in the mechanical properties of metallic glass can, for the most part, be rationalized on the basis of physically sound deformation mechanisms – STZ activity and free volume redistribution. The basic features of plastic deformation, including homogeneous flow, strain localization and fracture, as well as rate, temperature and pressure dependencies, have all been nominally explained on the basis of such physics. In fact, many of these trends were explained over 20 years ago, and the explanations hold today despite the rapid evolution in glass compositions; what might be termed "classical" mechanical responses are frequently "discovered" (or, more accurately, rediscovered) in new amorphous metals.

Despite our general ability to rationalize experimental data, many pieces required for the desired comprehensive understanding of glass deformation are yet missing. These missing pieces represent the difference between explanatory and predictive understanding, between the ability to merely explicate what we observe and the possibility of consciously optimizing metallic glasses for mechanical properties. In preparing our survey of the field, we have identified several areas that we believe present particularly pressing research needs. We offer these as examples of directions for future research:

- *Deeper connections to glass structure*. Perhaps the largest outstanding question about the mechanical behavior of metallic glasses is how the glass structure influences potential STZs, and the effect this might have upon macroscopic properties. The typical state descriptions (in terms of free volume, for instance) may be adequate in a general sense, but neglect many details of true glass structure – notably the short- and medium-range chemical order now believed common among bulk glass-forming alloys. Additionally, potential spectral differences in STZ behavior that might arise due to, for example, variations in local bond enthalpies and ordering energies have not yet been discussed in detail. Just as analogs and simulations first drew attention to the STZ mechanism, it seems clear that more advanced atomistic simulations can also point the way to improved state descriptions of deforming metallic glasses.
- *STZ structure*. While STZs constitute the unitary deformation processes dictating the overall stress–strain response of metallic glasses, precise identification of the size and shape of STZs remains elusive. While the details of STZ structure certainly depend on the structure of the glass, the size (i.e. the volume of the atomic cluster that transforms) and shape (spherical vs. disk-shaped) may show trends with strain state, strain rate and temperature that are general across all amorphous alloys. Both detailed and critical experiments and atomistic simulations are necessary to resolve this issue.
- *Understanding of shear band formation.* The details as to how shear localizes in metallic glasses remain largely a topic of speculation, in particular with respect to the process by which shear displacements (i) accumulate in a given microscopic location and (ii) propagate spatially. The order in which (i) and (ii) occur, the degree to which they are simultaneous or separate, and the effect of glass structure (e.g. state of relaxation) on such processes require further exploration. Hints of intrinsic size effects in shear banding behavior (see Section 4.2.4) may point the way to experiments that can address this complex problem, and certainly there is an important role for computer simulations here. But further resolution of the shear band formation process may substantially impact the effort to toughen glasses by shear band distribution.
- *Structural evolution in shear bands.* Section 6.2 outlines a variety of direct and indirect observations of material that underwent severe shear during the localization process, with a number of interesting consequences that include free volume accumulation and coalescence, and nanocrystallization. These observations represent pioneering work on a topic of particular relevance in the practical pursuit of tougher glasses, and much more effort is needed to understand structure evolution in shear bands. For example, systematic studies of shear band structure at different levels of shear displacement (strain) in a single glass could offer a sort of stroboscopic view of structural evolution during a shear banding event. Careful comparison of equivalent shear bands (i.e. comparable offsets) in strong vs. fragile, brittle vs. ductile or metalloid-containing vs. non-metalloid-containing glasses could elucidate the role of chemistry and pre-existing structure on shear-induced structural changes. Besides these experimental studies, there is also a need for a better theoretical understanding of how the evolving structure influences the rheology of active shear bands. Although several authors have identified nanocrystallization in shear bands as a potential cause of "strain hardening", at present this appears to be purely speculative without a firm grounding in terms of deformation mechanisms.
- *Fracture length scale.* As discussed in Section 5.1, the plastic zone size and the toughness of metallic glasses are highly correlated. However, the criterion for fracture necessarily involves a microstructural length scale over which either stress or strain (or both), presumably on a shear band, reach a critical value. This length is determined by the microscopic deformation and fracture mechanisms. Fractographic observations on metallic glasses do indeed allude to the possibility of such a length scale controlling their fracture. However, this fundamental parameter, which has significant implications for the design of tough metallic glasses, is yet to be systematically evaluated in terms of the composition and the structure of the glass.
- *Tough vs. brittle glasses.* While much has been learned about deformation processes in metallic glasses, our understanding of fracture micromechanisms is still nascent. There are several important and related questions that need thorough understanding if components made of metallic glasses are to be successfully deployed in load-bearing applications. For instance, what makes some glasses reasonably tough whereas some others are extremely brittle and hence impractical for engineering applications? What are causes for the observed ductile–brittle transition? Although the observed correlations with elastic properties (μ/B or ν) are suggestive, they remain to be elucidated in terms of actual deformation and fracture mechanisms. Also, is it possible to impart intrinsic toughness to a metallic glass by employing alloy design principles, and if yes, what are these principles?
- *Origins of fatigue.* Fatigue in materials is a result of kinematic irreversibility of the microscopic deformation processes, such as the to-and-fro motion of dislocations and associated plastic strain accumulation during cyclic loading of crystalline metals. However, the sources of kinematic irreversibility in amorphous metals have yet to be determined, despite the experimentally established fact that metallic glasses are prone to fatigue failure. Once the fundamental origins of fatigue in metallic glasses are understood, controlling them in order to enhance fatigue resistance will become an important area for research.

- *Systems with microstructure.* With the profusion of in situ and ex situ composites, foams and nanocrystal-reinforced structures based on amorphous metals, there is clearly a need for detailed understanding of how microstructure affects mechanical properties of metallic glass. In addition to classical property mismatches that impact mechanical behavior of conventional composites (e.g. thermal expansion mismatch, elastic mismatch), there are additional complexities in systems based on amorphous metals. For example, in addition to a mismatch between the yield stresses of coexisting phases, there can be a mismatch in yield criteria which affects load partitioning and strain evolution in composites. The problem of strain localization in, around or through a field of nanoparticles, larger reinforcements or porosity has been the subject of speculation, but neither focused theoretical consideration nor systematic experimentation.

These topics are but a few from among a vast list of potentially intriguing directions for future research. With the recent proliferation of new glasses, new characterization techniques and new researchers trained in this field, we look forward to a period of rapid progress on these fundamental questions.

Acknowledgements

We are indebted to the many researchers in this field with whom we have had valuable and stimulating discussions, and whose work provided the inspiration for writing this overview. We wish to thank in particular X. Gu, C.C. Hays, J. Lewandowski, R. Vaidyanathan and R. Raghavan for providing original artwork for the present article. We also appreciate the assistance of K.M. Flores for her critical reading of portions of the manuscript, and for providing original artwork. C.A.S. acknowledges support from the US Office of Naval Research, under Grant N00014-04-1-0669, as well as the U.S. Army Research Office under contract DAAD19-03-1-0235. T.C.H. gratefully acknowledges support from the National Science Foundation under grant DMR-0307009. U.R. acknowledges the assistance rendered by his students, P. Murali, R. Raghavan and K. Eswar Prasad during the preparation of parts of this paper and the financial support through a grant by the Defence Research and Development Organization, Government of India.

References

[1] Klement W, Willens RH, Duwez P. Nature 1960;187:869.
[2] Inoue A. Acta Mater 2000;48:279.
[3] Wang WH, Dong C, Shek CH. Mater Sci Eng R 2004;44:45.
[4] Johnson WL. JOM 2002;54:40.
[5] Greer AL, Rutherford KL, Hutchings IM. Int Mater Rev 2002;47:87.
[6] Schuh CA, Nieh TG. J Mater Res 2004;19:46.
[7] Hufnagel TC, editor. Viewpoint set on mechanical behavior of metallic glasses. Scripta materialia 2006;54:317.
[8] Pampillo CA. J Mater Sci 1975;10:1194.
[9] Argon AS. Inelastic deformation and fracture of glassy solids. In: Mughrabi H, editor. Material science and technology. Weinheim: VCH; 1993. p. 63.
[10] Argon AS, Kuo HY. Mater Sci Eng 1979;39:101.
[11] Srolovitz D, Vitek V, Egami T. Acta Metall Mater 1983;31:335.
[12] Falk ML. Phys Rev B 1999;60:7062.
[13] Bulatov VV, Argon AS. Model Sim Mater Sci Eng 1994;2:167.
[14] Bulatov VV, Argon AS. Model Sim Mater Sci Eng 1994;2:185.
[15] Bulatov VV, Argon AS. Model Sim Mater Sci Eng 1994;2:203.
[16] Falk ML, Langer JS. Phys Rev E 1998;57:7192.
[17] Lemaitre A. Phys Rev Lett 2002;89:195503.
[18] Lund AC, Schuh CA. Acta Mater 2003;51:5399.
[19] Lund AC, Schuh CA. Intermetallics 2004;12:1159.
[20] Langer JS, Pechenik L. Phys Rev E 2003;68:061507.
[21] Langer JS. Phys Rev E 2004;70:041502.
[22] Langer JS. Scripta Mater 2006;54:375.
[23] Argon AS, Shi LT. Philos Mag A 1982;46:275.
[24] Yamamoto R, Matsuoka H, Doyama M. Phys Status Solidi A 1979;51:163.
[25] Kobayashi S, Maeda K, Takeuchi S. Acta Metall 1980;28:1641.
[26] Rottler J, Robbins MO. Phys Rev E 2003;68:011507.
[27] Srolovitz D, Maeda K, Vitek V, Egami T. Philos Mag A 1981;44:847.
[28] Deng D, Argon AS, Yip S. Phil Trans R Soc Lond 1989;329:613.
[29] Kotelyanskii MJ, Mazo MA, Oleynik EF, Grivtsov AG. Phys Status Solidi B 1991;166:25.
[30] Gagnon G, Patton J, Lacks DJ. Phys Rev E 2001;64:051508.
[31] Lacks DJ. Phys Rev Lett 2001;87:225502.
[32] Varnik F, Bocquet L, Barrat J-L, Berthier L. Phys Rev Lett 2003;90:095702.
[33] Malandro DL, Lacks DJ. J Chem Phys 1999;110:4593.
[34] Tomida T, Egami T. Phys Rev B 1993;48:3048.
[35] Brinkmann K, Teichler H. Phys Rev B 2002;66:184205.
[36] Johnson WL, Samwer K. Phys Rev Lett 2005;95:195501.
[37] Mayr SG. Phys Rev Lett 2006;97:195501.
[38] Zink M, Samwer K, Johnson WL, Mayr SG. Phys Rev B 2006;73:172203.
[39] Spaepen F. Acta Metall 1977;25:407.
[40] Argon AS. Acta Metall 1979;27:47.
[41] Argon AS, Kuo HY. J. Non-Cryst Solids 1980;37:241.
[42] Maeda K, Takeuchi S. Phys Status Solidi A 1978;49:685.
[43] Shi Y, Falk ML. Scripta Mater 2006;54:381.
[44] Shi YF, Falk ML. Phys Rev Lett 2005;95:095502.
[45] Eshelby JD. Proc Roy Soc Lond A 1957;241:376.
[46] Heggen M, Spaepen F, Feuerbacher M. J Appl Phys 2005;97:033506.
[47] Fu XL, Li Y, Schuh CA. Appl Phys Lett 2005;87:241904.
[48] Daniel BSS, Reger-Leonhard A, Heilmaier M, Eckert J, Schultz L. Mech Time-Dependent Mater 2002;6:193.
[49] Heilmaier M, Eckert J. Adv Eng Mater 2005;7:833.
[50] Reger-Leonhard A, Heilmaier M, Eckert J. Scripta Mater 2000;43:459.
[51] Cohen MH, Turnbull D. J Chem Phys 1959;31:1164.
[52] Polk DE, Turnbull D. Acta Metall 1972;20:493.
[53] Shi FG, Nieh TG, Chou YT. Scripta Mater 2000;43:265.
[54] Nabarro FRN. Deformation of crystals by the motion of single ions. In: report of a conference on the strength of solids. London: The Physical Society; 1948. p. 75.
[55] Herring C. J Appl Phys 1950;21:437.
[56] Coble RL. J Appl Phys 1963;34:1679.
[57] Gilman JJ. J Appl Phys 1975;46:1625.
[58] Li JCM. Micromechanisms of deformation and fracture. In: Metallic glasses. Materials Park, OH: American Society for Metals; 1978 [Chapter 9].
[59] Li JCM. Metall Trans A 1985;16:2227.
[60] Bobrov OP, Khonik VA. J Non-Cryst Solids 1995;193:603.

[61] Vella JB, Mann AB, Kung H, Chien CL, Weihs TP, Cammarata RC. J Mater Res 2004;19:1840.
[62] Kikuchi M, Fukamichi K, Kimura H, Masumoto T. Science reports of the Research Institutes Tohoku University. Ser A - Phys Chem Metall 1986;33:102.
[63] Ogi H, Shimoike G, Hirao M, Takashima K, Higo Y. J Appl Phys 2002;91:4857.
[64] Kunzi HU. Top Appl Phys 1983;53:169.
[65] Knuyt G, Deschepper L, Stals LM. J Phys F 1986;16:1989.
[66] Courtney TH. Mechanical behavior of materials. Boston, MA: McGraw-Hill; 2000.
[67] Jovanovic S, Smith CS. J Appl Phys 1961;32:161.
[68] Ashby MF, Nelson AN, Centamore RMA. Scripta Metall 1970;4:715.
[69] Masumoto T, Maddin R. Acta Metall 1971;19:725.
[70] Golding B, Bagley BG, Hsu FSL. Phys Rev Lett 1972;29:68.
[71] Chen HS. J Appl Phys 1978;49:3289.
[72] Weaire D, Ashby MF, Logan J, Weins MJ. Acta Metall 1971;19:779.
[73] Suzuki Y, Egami T. J Non-Cryst Solids 1985;75:361.
[74] Berry BS. Elastic and anealstic behavior. In: Metallic glasses. Materials Park, OH: American Society for Metals; 1978. p. 161.
[75] Nowick AS, Berry BS. Anelastic relaxation in crystalline solids. New York: Academic Press; 1972.
[76] Weiss M, Moske M, Samwer K. Appl Phys Lett 1996;69:3200.
[77] Schroter K, Wilde G, Willnecker R, Weiss M, Samwer K, Donth E. Eur Phys J B 1998;5:1.
[78] Suh DW, Dauskardt RH. J Mater Res 2002;17:1254.
[79] Egami T. Mater Res Bull 1978;13:557.
[80] Greer AL. Structural relaxation and atomic transport in amorphous alloys. In: Liebermann HH, editor. Rapidly solidified alloys. New York: Marcel Dekker; 1993. p. 69.
[81] Lewandowski JJ, Wang WH, Greer AL. Philos Mag Lett 2005;85:77.
[82] Morito N, Egami T. Acta Metall 1984;32:603.
[83] Bonetti E. Philos Mag B 1987;56:185.
[84] Tan M, He YH. J Non-Cryst Solids 1988;105:155.
[85] Aboki AM, Bouquet G, Tronc E. J Mater Sci 1991;26:4166.
[86] Khonik VA, Spivak LV. Acta Mater 1996;44:367.
[87] Kursumovic A, Scott MG, Girt E, Cahn RW. Scripta Metall 1980;14:1303.
[88] Berry BS, Pritchet WC, Tsuei CC. Phys Rev Lett 1978;41:410.
[89] Barmatz M, Chen HS. Phys Rev B 1974;9:4073.
[90] Sinning HR, Woldt E, Haessner F. Mater Sci Eng 1988;97:501.
[91] Zolotukhin IV, Belyavskii VI, Khonik VA, Ryabtseva TN. Phys Status Solidi A 1989;116:255.
[92] Schuh CA, Lund AC, Nieh TG. Acta Mater 2004;52:5879.
[93] Demetriou MD, Johnson WL. J Appl Phys 2004;95:2857.
[94] Demetriou MD, Johnson WL. Mater Sci Eng A 2004;375–7:270.
[95] Demetriou MD, Johnson WL. Acta Mater 2004;52:3403.
[96] Kawamura Y, Nakamura T, Inoue A. Scripta Mater 1998;39:301.
[97] Kawamura Y, Shibata T, Inoue A, Masumoto T. Acta Mater 1997;46:253.
[98] Wang G, Shen J, Sun JF, Huang YJ, Zou J, Lu ZP, et al. J Non-Cryst Solids 2005;351:209.
[99] Wang G, Fang SS, Xiao XS, Hua Q, Gu HZ, Dong YD. Mater Sci Eng A 2004;373:217.
[100] Schroers J. JOM 2005;57:35.
[101] Schroers J, Paton N. Adv Mater Process 2006;164:61.
[102] Lewandowski JJ, Shazly M, Nouri AS. Scripta Mater 2006;54:337.
[103] Bletry M, Guyot P, Brechet Y, Blandin JJ, Soubeyroux JL. Mater Sci Eng A 2004;387–389:1005.
[104] Tsao SS, Spaepen F. Acta Metall 1985;33:881.
[105] Busch R, Liu W, Johnson WL. J Appl Phys 1998;83:4134.
[106] Bakke E, Busch R, Johnson WL. Appl Phys Lett 1995;67:3260.
[107] Shadowspeaker L, Shah M, Busch R. Scripta Mater 2004;50:1035.
[108] Busch R, Bakke E, Johnson WL. Acta Mater 1998;46:4725.
[109] Angell CA. Science 1995;267:1924.
[110] Lu J, Ravichandran G, Johnson WL. Acta Mater 2003;51:3429.
[111] Ghosh AK, Ayres RA. Metall Trans 1976;7A:1589.
[112] Nichols FA. Acta Metall 1980;28:663.
[113] Hart EW. Acta Metall 1967;15:351.
[114] Burke MA, Nix WD. Acta Metall 1975;23:793.
[115] Kim WJ, Ma DS, Jeong HG. Scripta Mater 2003;49:1067.
[116] Shen J, Wang G, Sun JF, Stachurski ZH, Yan C, Ye L, et al. Intermetallics 2005;13:79.
[117] Homer C, Eberhardt A. Scripta Metall 1980;14:1331.
[118] Nieh TG, Wadsworth J, Liu CT, Ohkubo T, Hirotsu Y. Acta Mater 2001;49:2887.
[119] Nieh TG, Schuh C, Wadsworth J, Li Y. Intermetallics 2002;10:1177.
[120] Bae DH, Lim HK, Kim SH, Kim DH, Kim WT. Acta Mater 2002;50:1749.
[121] Chiang CL, Chu JP, Lo CT, Nieh TG, Wang ZX, Wang WH. Intermetallics 2004;12:1057.
[122] Wang WK, Iwasaki H, Fukamichi K. J Mater Sci 1980;15:2701.
[123] Wang WK, Iwasaki H, Suryanarayana C, Masumoto T. J Mater Sci 1983;18:3765.
[124] Yao B, Li FS, Lin XM, Ding BZ, Su WH, Hu ZQ. J Non-Cryst Solids 1997;217:317.
[125] Zhang XY, Zhang FX, Zhang JW, Yu W, Zhang M, Zhao JH, et al. J Appl Phys 1998;84:1918.
[126] Ye F, Lu K. Acta Mater 1999;47:2449.
[127] Wang WH, He DW, Zhao DQ, Yao YS, He M. Appl Phys Lett 1999;75:2770.
[128] Jiang JZ, Zhou TJ, Rasmussen H, Kuhn U, Eckert J, Lathe C. Appl Phys Lett 2000;77:3553.
[129] Jiang JZ, Olsen JS, Gerward L, Abdali S, Eckert J, Schlorke-de Boer N, et al. J Appl Phys 2000;87:2664.
[130] Zhuang YX, Jiang JZ, Zhou TJ, Rasmussen H, Gerward L, Mezouar M, et al. Appl Phys Lett 2000;77:4133.
[131] Wang WH, Zhuang YX, Pan MX, Yao YS. J Appl Phys 2000;88:3914.
[132] Jiang JZ, Zhuang YX, Rasmussen H, Saida J, Inoue A. Phys Rev B 2001;6409:094208.
[133] Zhang J, Qiu KQ, Wang AM, Zhang HF, Quan MX, Hu ZQ. J Mater Res 2002;17:2935.
[134] Ko BC, Wesseling P, Vatamanu OL, Shiflet GJ, Lewandowski JJ. Intermetallics 2002;10:1099.
[135] Jiang JZ, Yang B, Saksl K, Franz H, Pryds N. J Mater Res 2003;18:895.
[136] Zhang J, Zhang HF, Quan M, Hu ZQ. Scripta Mater 2003;49:485.
[137] Wesseling P, Ko BC, Vatamanu OL, Caris J, Lewandowski JJ. Mater Res Soc Proc 2003;754:CC10.
[138] Yang C, Wang WK, Liu RP, Zhan ZJ, Sun LL, Zhang J, et al. J. Appl Phys 2006;99:023525.
[139] Jeong HG, Kim WJ. J Mater Res 2005;20:1447.
[140] Steif PS, Spaepen F, Hutchinson JW. Acta Metall 1982;30:447.
[141] Duine PA, Sietsma J, Vandenbeukel A. Acta Metall Mater 1992;40:743.
[142] De Hey P, Sietsma J, Van den Beukel A. Acta Mater 1998;46:5873.
[143] Taub AI, Spaepen F. Acta Metall 1980;28:1781.
[144] Demetriou MD, Johnson WL. Scripta Mater 2005;52:833.
[145] Tsao SS, Spaepen F. Acta Metall 1985;33:891.
[146] Volkert CA, Spaepen F. Acta Metall 1989;37:1355.
[147] Huang R, Suo Z, Prevost JH, Nix WD. J Mech Phys Solids 2002;50:1011.
[148] Chen HS, Kato H, Inoue A. Jpn J Appl Phys Part 1-Regular Papers Short Notes & Review Papers 2000;39:1808.
[149] Kato H, Kawamura Y, Inoue A, Chen HS. Mater Trans JIM 2000;41:1202.
[150] Safarik DJ, Cady CM, Schwarz RB. Acta Mater 2005;53:2193.
[151] Kimura H, Masumoto T. Acta Metall 1983;31:231.
[152] Kimura H, Masumoto T. Acta Metall 1980;28:1663.
[153] Kimura H, Masumoto T. Philos Mag A 1981;44:1021.
[154] Lowhaphandu P, Lewandowski JJ. Scripta Mater 1998;38:1811.
[155] Flores KM, Dauskardt RH. Scripta Mater 1999;41:937.
[156] Pampillo CA, Chen HS. Mater Sci Eng 1974;13:181.

[157] Zhang ZF, Zhang H, Pan XF, Das J, Eckert J. Philos Mag Lett 2005;85:513.
[158] Bei H, Xie S, George EP. Phys Rev Lett 2006;96:105503.
[159] Mukai T, Nieh TG, Kawamura Y, Inoue A, Higashi K. Intermetallics 2002;10:1071.
[160] Megusar J, Argon AS, Grant NJ. Mater Sci Eng 1979;38:63.
[161] Anand L, Su C. J Mech Phys Solids 2005;53:1362.
[162] Schuh CA, Argon AS, Nieh TG, Wadsworth J. Philos Mag A 2003;83:2585.
[163] Conner RD, Johnson WL, Paton NE, Nix WD. J Appl Phys 2003;94:904.
[164] Inoue A, Zhang W, Tsurui T, Yavari AR, Greer AL. Philos Mag Lett 2005;85:221.
[165] Das J, Tang MB, Kim KB, Theissmann R, Baier F, Wang WH, et al. Phys Rev Lett 2005;94:205501.
[166] Lee SW, Huh MY, Fleury E, Lee JC. Acta Mater 2006;54:349.
[167] Zhu ZW, Zhang HF, Sun WS, Ding BZ, Hu ZQ. Scripta Mater 2006;54:1145.
[168] Yao KF, Ruan F, Yang YQ, Chen N. Appl Phys Lett 2006;88:122106.
[169] Tang CG, Li Y, Zeng KY. Mater Let 2005;59:3325.
[170] Bhowmick R, Raghavan R, Chattopadhyay K, Ramamurty U. Acta Mater 2006;54:4221.
[171] Hufnagel TC, El-Deiry P, Vinci RP. Scripta Mater 2000;43:1071.
[172] Moser B, Kuebler J, Meinhard H, Muster W, Michler J. Adv Eng Mater 2005;7:388.
[173] Leamy HJ, Chen HS, Wang TT. Mater Trans JIM 1972;3:699.
[174] Wright WJ, Saha R, Nix WD. Mater Trans JIM 2001;42:642.
[175] Wright WJ, Schwarz RB, Nix WD. Mater Sci Eng A 2001;319–321:229.
[176] Bai Y, Dodd B. Adiabatic shear localization: Occurrence, theories, and applications. Oxford: Pergamon Press; 1992.
[177] Wright TW. The physics and mathematics of adiabatic shear bands. Cambridge: Cambridge University Press; 2002.
[178] Chen HS. Appl Phys Lett 1976;29:328.
[179] Neuhauser H. Scripta Metall 1978;12:471.
[180] Lewandowski JJ, Greer AL. Nature Mater 2006;5:15.
[181] Bruck HA, Rosakis AJ, Johnson WL. J Mater Res 1996;11:503.
[182] Flores KM, Dauskardt RH. J Mater Res 1999;14:638.
[183] Yang B, Liu CT, Nieh TG, Morrison ML, Liaw PK, Buchanan RA. J Mater Res 2006;21:915.
[184] Zhang Y, Greer AL. Appl Phys Lett 2006;89:071907.
[185] Hufnagel TC, Jiao T, Li Y, Xing L-Q, Ramesh KT. J Mater Res 2002;17:1441.
[186] Li H, Subhash G, Gao XL, Kecskes LJ, Dowding RJ. Scripta Mater 2003;49:1087.
[187] Sunny GP, Prakash V, Lewandowski JJ. Proceedings of the ASME international mechanical engineering congress and exposition, IMECE 2005 2005:83016.
[188] Sunny GP, Lewandowski JJ. J Mater Res 2007;22:389.
[189] Mukai T, Nieh TG, Kawamura Y, Inoue A, Higashi K. Scripta Mater 2002;46:43.
[190] Subhash G, Dowding RJ, Kecskes LJ. Mater Sci Eng A 2002;334:33.
[191] Jiang WH, Atzmon M. J Mater Res 2003;18:755.
[192] Schuh CA, Nieh TG. Acta Mater 2003;51:87.
[193] Nieh TG, Schuh C, Wadsworth J, Li Y. Intermetallics 2002;10:1177.
[194] Schuh CA, Nieh TG, Kawamura Y. J Mater Res 2002;17:1651.
[195] Chen HS. Scripta Metall 1973;7:931.
[196] Sergueeva AV, Mara NA, Branagan DJ, Mukherjee AK. Scripta Mater 2004;50:1303.
[197] Sergueeva AV, Mara NA, Kuntz JD, Branagan DJ, Mukherjee AK. Mater Sci Eng A 2004;383:219.
[198] Lewandowski JJ, Lowhaphandu P. Int Mater Rev 1998;43:145.
[199] Desai CS, Siriwardane HJ. Constitutive laws for engineering materials. Englewood Cliffs, NJ: Prentice-Hall; 1984.
[200] Reynolds O. Philos Mag 1885;20:469.
[201] Taylor DW. Fundamentals of soil mechanics. New York: John Wiley; 1948.
[202] Li JCM, Wu JBC. J Mater Sci 1976;11:445.
[203] Donovan PE. Acta Mater 1989;37:445.
[204] Kimura H, Masumoto T. In: Lubrosky FE, editor. Amorphous metallic alloys. London: Butterworth; 1983. p. 87.
[205] Kimura H, Ast DG, Bassett WA. J Appl Phys 1982;53:3523.
[206] Bruck HA, Christman T, Rosakis AJ, Johnson WL. Scripta Metall Mater 1994;30:429.
[207] Davis LA, Kavesh S. J Mater Sci 1975;10:453.
[208] Lewandowski JJ, Lowhaphandu P. Philos Mag A 2002;82:3427.
[209] Lowhaphandu P, Montgomery SL, Lewandowski JJ. Scripta Mater 1999;41:19.
[210] Lu J, Ravichandran G. J Mater Res 2003;18:2039.
[211] Flores KM, Dauskardt RH. Acta Mater 2001;49:2527.
[212] Vaidyanathan R, Dao M, Ravichandran G, Suresh S. Acta Mater 2001;49:3781.
[213] Young RJ, Lovell PA. Introduction to polymers. London: Chapman & Hall; 1992.
[214] Raghava RS, Caddell RM. Int J Mech Sci 1973;15:967.
[215] Schuh CA, Lund AC. Nature Mater 2003;2:449.
[216] Zhang ZF, He G, Eckert J, Schultz L. Phys Rev Lett 2003;91:045505.
[217] Ott RT, Sansoz F, Jiao T, Warner D, Fan C, Molinari JF, et al. Metall Mater Trans 2006;37A:3251.
[218] Flores KM, Dauskardt RH. Intermetallics 2004;12:1025.
[219] Flores KM, Dauskardt RH. J Mech Phys Solids 2006;54:2418.
[220] Sargent PM, Donovan PE. Scripta Metall 1982;16:1207.
[221] Ramamurty U, Jana S, Kawamura Y, Chattopadhyay K. Acta Mater 2005;53:705.
[222] Jana S, Ramamurty U, Chattopadhyay K, Kawamura Y. Mater Sci Eng A 2004;375–7:1191.
[223] Marsh DM. Proc Roy Soc Lond A 1964;279:420.
[224] Johnson KL. J Mech Phys Solids 1970;18:115.
[225] Narasimhan R. Mech Mater 2004;36:633.
[226] Patnaik MNM, Narashimhan R, Ramamurty U. Acta Mater 2004;52:3335.
[227] Keryvin V. Acta Mater 2007, in press, doi:10.1016/j.actamat.2006.12.005.
[228] Conner RD, Li Y, Nix WD, Johnson WL. Acta Mater 2004;52:2429.
[229] Ravichandran G, Molinari A. Acta Mater 2005;53:4087.
[230] Inoue A, Katsuya A, Amiya K, Masumoto T. Mater Trans JIM 1995;36:802.
[231] Frost HJ, Ashby MF. Deformation-mechanism maps: The plasticity and creep of metals and ceramics. Oxford: Pergamon Press; 1982.
[232] Masumoto T, Maddin R. Mater Sci Eng 1975;19:1.
[233] Conner RD, Rosakis AJ, Johnson WL, Owen DM. Scripta Mater 1997;37:1373.
[234] Gilbert CJ, Ritchie RO, Johnson WL. Appl Phys Lett 1997;71:476.
[235] Hess PA, Poon SJ, Shiflet GJ, Dauskardt RH. J Mater Res 2005;20:783.
[236] Davis LA. J Mater Sci 1975;10:1557.
[237] Spaepen F, Taub AI. In: Lubrosky FE, editor. Amorphous metallic alloys. London: Butterworth; 1983. p. 31.
[238] Xi XK, Zhao DQ, Pan MX, Wang WH, Wu Y, Lewandowski JJ. Phys Rev Lett 2005;94:125510.
[239] Nagendra N, Ramamurty U, Goh TT, Li Y. Acta Mater 2000;48:2603.
[240] Gilbert CJ, Ager JW, Schroeder V, Ritchie RO, Lloyd JP, Graham JR. Appl Phys Lett 1999;74:3809.
[241] Argon AS, Salama M. Mater Sci Eng 1976;23:219.
[242] Christiansen A, Shortall JB. J Mater Sci 1976;11:1113.
[243] Wu TW, Spaepen F. Philos Mag B 1990;61:739.
[244] Yavari AR. Mater Sci Eng 1988;98:491.
[245] Raghavan R, Murali P, Ramamurty U. Intermetallics 2006;14:1051.
[246] Suh D, Dauskardt RH. J Non-Cryst Solids 2003;317:181.
[247] Gilbert CJ, Schroeder V, Ritchie RO. Metall Mater Trans 1999;30:1739.
[248] Kelly A, Tyson WR, Cottrell AH. Philos Mag 1967;15:567.
[249] Murali P, Ramamurty U. Acta Mater 2005;53:1467.

[250] Kimura H, Masumoto T. Scripta Metall 1975;9:211.
[251] Ast DG, Krenitsky D. Mater Sci Eng 1976;23:241.
[252] Keryvin V, Bernard C, Sangleboeuf JC, Yokoyama Y, Rouxel T. J Non-Cryst Solids 2006;352:2863.
[253] Lee JG, Park SS, Lee DG, Lee S, Kim NJ. Intermetallics 2004;12:1125.
[254] Ogura T, Fukushima K, Masumoto T. Scripta Metall 1975;9:979.
[255] Chaki TK, Li JCM. Scripta Metall 1984;18:703.
[256] Alpas AT, Edwards L, Reid CN. Metall Trans A 1989;20:1395.
[257] Suresh S. Fatigue of materials. 2nd ed. Cambridge: Cambridge University Press; 1998.
[258] Gilbert CJ, Lippmann JM, Ritchie RO. Scripta Mater 1998;38:537.
[259] Menzel BC, Dauskardt RH. Acta Mater 2006;54:935.
[260] Flores KM, Johnson WL, Dauskardt RH. Scripta Mater 2003;49:1181.
[261] Wang GY, Liaw PK, Peker A, Yang B, Benson ML, Yuan W, et al. Mater Res Soc Proc 2004;806:331.
[262] Ogura T, Masumoto T, Fukushima K. Scripta Metall 1975;9:109.
[263] Peter WH, Liaw PK, Buchanan RA, Liu CT, Brooks CR, Horton JA, et al. Intermetallics 2002;10:1125.
[264] Peter WH, Buchanan RA, Liu CT, Liaw PK. J Non-Cryst Solids 2003;317:187.
[265] Qiao DC, Liaw PK, Fan C, Lin YH, Wang GY, Choo H, Buchanan RA. Intermetallics 2006;14:1043.
[266] Wang GY, Liaw PK, Peker A, Freels M, Peter WH, Buchanan RA, et al. Intermetallics 2006;14:1091.
[267] Wang GY, Liaw PK, Peker A, Yang B, Benson ML, Yuan W, et al. Intermetallics 2005;13:429.
[268] Menzel BC, Dauskardt RH. Scripta Mater 2006;55:601.
[269] Aydiner CC, Ustundag E, Hanan JC. Metall Mater Trans 2001;32:2709.
[270] Aydiner CC, Ustundag E, Prime MB, Peker A. J Non-Cryst Solids 2003;316:82.
[271] Launey ME, Busch R, Kruzic JJ. Scripta Mater 2006;54:483.
[272] Olofinjana AO, Davies HA. Mater Sci Eng A 1994;186:143.
[273] Zhang Y, Wang WH, Greer AL. Nature Mater 2006;5:857.
[274] Cameron KK, Dauskardt RH. Scripta Mater 2006;54:349.
[275] Egami T. In: Luborsky FE, editor. Amorphous metallic alloys. London: Butterworth; 1983.
[276] Koebrugge GW, Sietsma J, Vandenbeukel A. Acta Metall Mater 1992;40:753.
[277] Nagel C, Ratzke K, Schmidtke E, Wolff J, Geyer U, Faupel F. Phys Rev B 1998;57:10224.
[278] Vandenbeukel A, Sietsma J. Acta Metall Mater 1990;38:383.
[279] Tuinstra P, Duine PA, Sietsma J, Vandenbeukel A. Acta Metall Mater 1995;43:2815.
[280] Slipenyuk A, Eckert J. Scripta Mater 2004;50:39.
[281] Gerling R, Schimansky FP, Wagner R. Scripta Metall 1983;17:203.
[282] Lamparter P, Steeb S. J Non-Cryst Solids 1988;106:137.
[283] Yavari AR. J Mater Res 1986;1:746.
[284] Wu TW, Spaepen F. Acta Metall 1985;33:2185.
[285] Ramamurty U, Lee ML, Basu J, Li Y. Scripta Mater 2002;47:107.
[286] Lind M, Duan G, Johnson WL. Phys Rev Lett 2006;97:015501.
[287] Steif PS. J Mech Phys Solids 1983;31:359.
[288] Pampillo CA. Scripta Metall 1972;6:915.
[289] Vianco PT, Li JCM. J Mater Sci 1987;22:3129.
[290] Krishnanand KD, Cahn RW. Scripta Metall 1975;9:1259.
[291] Lakshmanan V, Li JCM, Tsai CL. Acta Metall Mater 1990;38:625.
[292] Tseng WJ, Koike K, Li JCM. J Mater Res 1993;8:775.
[293] Masumoto T, Maddin R. Mater Sci Eng 1975;19:1.
[294] Masumoto T, Kimura H, Inoue A, Waseda Y. Mater Sci Eng 1976;23:141.
[295] Waseda Y, Aust KT, Masumoto T. Scripta Metall 1979;13:187.
[296] Waseda Y, Egami T. J Mater Sci 1979;14:1249.
[297] Calvayrac Y, Harmelin M, Quivy A, Chevalier JP, Bigot J. Scripta Metall 1980;14:895.
[298] Takahara Y, Matsuda H. Trans Jpn Inst Met 1987;28:535.
[299] Koba ES, Milman YV, Rachek AP. Acta Metall Mater 1994;42:1383.
[300] Guoan W, Cowlam N, Gibbs MRJ. J Mater Sci 1984;19:1374.
[301] Sethi VK, Gibala R, Heuer AH. Scripta Metall 1978;12:207.
[302] Donovan PE, Stobbs WM. Acta Metall 1981;29:1419.
[303] Pekarskaya E, Kim CP, Johnson WL. J Mater Res 2001;16:2513.
[304] Li J, Spaepen F, Hufnagel TC. Philos Mag A 2002;82:2623.
[305] Jiang WH, Atzmon M. Acta Mater 2003;51:4095.
[306] Kanungo BP, Glade SC, Asoka-Kumar P, Flores KM. Intermetallics 2004;12:1073.
[307] Deng DG, Lu BH. Scripta Metall 1983;17:515.
[308] Cahn RW, Pratten NA, Scott MG, Sinning HR, Leonardsson L. Mater Res Soc Proc 1984;28:241.
[309] Nasu T, Nagaoka K, Itoh F, Suzuki K. J Phys Soc Japan 1989;58:894.
[310] Hajlaoui K, Benameur T, Vaughan G, Yavari AR. Scripta Mater 2004;51:843.
[311] Bever MB, Holt DL, Titchene Al. Prog Mater Sci 1972;17:5.
[312] Kanungo BP, Lambert MJ, Flores KM. Mater Res Soc Proc 2004;806:295.
[313] Cao QP, Li JF, Zhou YH, Horsewell A, Jiang JZ. Appl Phys Lett 2005;87:101901.
[314] Puska MJ, Nieminen RM. Rev Mod Phys 1994;66:841.
[315] Hautojarvi P, Corbel C. Proceedings of the international school of physics "Enrico Fermi" 1995:CXXV.
[316] Suh D, Dauskardt RH, Asoka-Kumar P, Sterne PA, Howell RH. J Mater Res 2003;18:2021.
[317] Bernal JD. Nature 1959;183:141.
[318] Cargill GSCI. Solid State Phys 1975;30:227.
[319] Asoka-Kumar P, Hartley J, Howell R, Sterne PA, Nieh TG. Appl Phys Lett 2000;77:1973.
[320] Flores KM, Suh D, Dauskardt RH, Asoka-Kumar P, Sterne PA, Howell RH. J Mater Res 2002;17:1153.
[321] Li J, Wang ZL, Hufnagel TC. Phys Rev B 2002;65:144201.
[322] Wright WJ, Hufnagel TC, Nix WD. J Appl Phys 2003;93:1432.
[323] Chen H, He Y, Shiflet GJ, Poon SJ. Nature 1994;367:541.
[324] Jiang WH, Atzmon M. Scripta Mater 2006;54:333.
[325] Kim J-J, Choi Y, Suresh S, Argon AS. Science 2002;295:654.
[326] Jiang WH, Pinkerton FE, Atzmon M. J Appl Phys 2003;93:9287.
[327] He Y, Shiflet GJ, Poon SJ. Acta Metall Mater 1995;43:83.
[328] Perepezko JH, Hebert RJ, Wilde G. Mater Sci Eng A 2004;375–377:171.
[329] El Eskandarany MS, Saida J, Inoue A. Acta Mater 2003;51:4519.
[330] El Eskandarany MS, Akoi K, Sumiyama K, Suzuki K. Appl Phys Lett 1997;70:1679.
[331] Csontos AA, Shiflet GJ. Nanostruct Mater 1997;9:281.
[332] Akhtar D, Cantor B, Cahn RW. Scripta Metall 1982;16:417.
[333] Akhtar D, Misra RDK. Scripta Metall 1985;19:1195.
[334] Mazzone G, Montone A, Antisari MV. Phys Rev Lett 1990;65:2019.
[335] Karpe N, Larsen KK, Bottiger J. Philos Mag B 1992;66:507.
[336] Lund AC, Schuh CA. Phys Rev Lett 2003;91:235505.
[337] Helfand E, Fredrickson GH. Phys Rev Lett 1989;62:2468.
[338] Wu XL, Pine DJ, Dixon PK. Phys Rev Lett 1991;66:2408.
[339] Clarke N. Phase Behav Polym Blends 2005;183:127.
[340] Lund AC, Schuh CA. J Appl Phys 2004;95:4815.
[341] Cini E, Vinet B, Desre PJ. Philos Mag A 2000;80:955.
[342] Lohwongwatana B, Schroers J, Johnson WL. Phys Rev Lett 2006;96:075503.
[343] Maeda K, Takeuchi S. Philos Mag A 1981;44:643.
[344] Albano F, Falk ML. J Chem Phys 2005:122.
[345] Chalupa J, Leath PL, Reich GR. J Phys C 1979;12:L31.
[346] Bailey NP, Schiotz J, Jacobsen KW. Phys Rev B 2006;73:064108.
[347] Li QK, Li M. Appl Phys Lett 2006;88:241903.
[348] Voyles PM, Gibson JM, Treacy MMJ. J Electr Microsc 2000;49:259.
[349] Li J, Gu X, Hufnagel TC. Microsc Microanal 2003;9:509.
[350] Stratton WG, Hamann J, Perepezko JH, Voyles PM, Mao X, Khare SV. Appl Phys Lett 2005;86:141910.
[351] Alpas AT, Embury JD. Scripta Metall 1988;22:265.

[352] Leng Y, Courtney TH. J Mater Sci 1989;24:2006.
[353] Leng Y, Courtney TH. Metall Trans A 1990;21:2159.
[354] Leng Y, Courtney TH. J Mater Sci 1991;26:588.
[355] Ashby MF, Greer AL. Scripta Mater 2006;54:321.
[356] Brothers AH, Dunand DC. Adv Mater 2005;17:484.
[357] Brothers AH, Dunand DC. Scripta Mater 2006;54:513.
[358] Wada T, Inoue A, Greer AL. Appl Phys Lett 2005;86:251907.
[359] Wada T, Kinaka M, Inoue A. J Mater Res 2006;21:1041.
[360] Schroers J, Johnson WL. Phys Rev Lett 2004;93:255506.
[361] Chen HS, Krause JT, Coleman E. J Non-Cryst Solids 1975;18:157.
[362] Pugh SF. Philos Mag 1954;45:823.
[363] Rice JR, Thomson R. Philos Mag 1974;29:73.
[364] Novikov VN, Sokolov AP. Nature 2004;431:961.
[365] Egami T. Intermetallics 2006;14:882.
[366] Battezzati L. Mater Trans JIM 2005;46:2915.
[367] Wang WH. J Appl Phys 2006;99:093506.
[368] Zhang Y, Greer AL. J Alloys Comp 2007, in press, doi:10.1016/j.jallcom.2006.08.094.
[369] Gu XJ, McDermott AG, Poon SJ, Shiflet GJ. Appl Phys Lett 2006;88:211905.
[370] Xing LQ, Li Y, Ramesh KT, Li J, Hufnagel TC. Phys Rev B 2001;6418:180201.
[371] Lee MH, Lee JY, Bae DH, Kim WT, Sordelet DJ, Kim DH. Intermetallics 2004;12:1133.
[372] Park ES, Lee JY, Kim DH. J Mater Res 2005;20:2379.
[373] Bae DH, Lee SW, Kwon JW, Yi S, Park JS. J Mater Res 2006;21:1305.
[374] Inoue A, Sobu S, Louzguine DV, Kimura H, Sasamori K. J Mater Res 2004;19:1539.
[375] Park JM, Chang HJ, Han KH, Kim WT, Kim DH. Scripta Mater 2005;53:1.
[376] Bae DH, Lee MH, Kim DH, Sordelet DJ. Appl Phys Lett 2003;83:2312.
[377] Choi-Yim H, Busch R, Koster U, Johnson WL. Acta Mater 1999;47:2455.
[378] Choi-Yim H, Conner RD, Szuecs F, Johnson WL. Acta Mater 2002;50:2737.
[379] Choi-Yim H, Conner RD, Szuecs F, Johnson WL. Scripta Mater 2001;45:1039.
[380] Choi-Yim H, Schroers J, Johnson WL. Appl Phys Lett 2002;80:1906.
[381] Fu HM, Zhang HF, Wang H, Zhang QS, Hu ZQ. Scripta Mater 2005;52:669.
[382] Kato H, Hirano T, Matsuo A, Kawamura Y, Inoue A. Scripta Mater 2000;43:503.
[383] Li H, Subhash G, Kecskes LJ, Dowding RJ. Mater Sci Eng A 2005;403:134.
[384] Lim HK, Park ES, Park JS, Kim WT, Kim DH. J Mater Sci 2005;40:6127.
[385] Xu YK, Ma H, Xu J, Ma E. Acta Mater 2005;53:1857.
[386] Xu YK, Xu J. Scripta Mater 2003;49:843.
[387] Fan C, Ott RT, Hufnagel TC. Appl Phys Lett 2002;81:1020.
[388] Fan C, Li HQ, Kecskes LJ, Tao KX, Choo H, Liaw PK, et al. Phys Rev Lett 2006;96:145506.
[389] Fu HM, Wang H, Zhang HF, Hu ZQ. Scripta Mater 2006;54:1961.
[390] Kim YC, Fleury E, Lee JC, Kim DH. J Mater Res 2005;20:2474.
[391] Lee JC, Kim YC, Ahn JP, Kim HS. Acta Mater 2005;53:129.
[392] Ma H, Xu J, Ma E. Appl Phys Lett 2003;83:2793.
[393] Bartusch B, Schurack F, Eckert J. Mater Trans JIM 2002;43:1979.
[394] Zhang W, Ishihara S, Inoue A. Mater Trans JIM 2002;43:1767.
[395] Hirano T, Kato H, Matsuo A, Kawamura Y, Inoue A. Mater Trans JIM 2000;41:1454.
[396] Ott RT, Sansoz F, Molinari JF, Almer J, Ramesh KT, Hufnagel TC. Acta Mater 2005;53:1883.
[397] Jiao T, Kecskes LJ, Hufnagel TC, Ramesh KT. Metall Mater Trans 2004;35A:3439.
[398] Dong WB, Zhang HF, Sun WS, Wang AM, Li H, Hu ZQ. J Mater Res 2006;21:1490.
[399] Sun GY, Chen G, Liu CT, Chen GL. Scripta Mater 2006;55:375.
[400] Zhang HF, Wang AM, Li H, Sun WS, Ding BZ, Hu ZQ, et al. J Mater Res 2006;21:1351.
[401] Eckert J, Kubler A, Schultz L. J Appl Phys 1999;85:7112.
[402] Bian Z, He G, Chen GL. Scripta Mater 2002;46:407.
[403] Fan C, Louzguine DV, Li CF, Inoue A. Appl Phys Lett 1999;75:340.
[404] Fan C, Inoue A. Appl Phys Lett 2000;77:46.
[405] Fan C, Li CF, Inoue A. J Non-Cryst Solids 2000;270:28.
[406] Fan C, Li CF, Inoue A, Haas V. Phys Rev B 2000;61:R3761.
[407] Greer AL. Mater Sci Eng A 2001;304-306:68.
[408] Kim YC, Na JH, Park JM, Kim DH, Lee JK, Kim WT. Appl Phys Lett 2003;83:3093.
[409] Xing LQ, Eckert J, Loser W, Schultz L. Appl Phys Lett 1999;74:664.
[410] Basu J, Nagendra N, Li Y, Ramamurty U. Philos Mag 2003;83:1747.
[411] Szuecs F, Kim CP, Johnson WL. Acta Mater 2001;49:1507.
[412] Lee ML, Li Y, Schuh CA. Acta Mater 2004;52:4121.
[413] Zhang Y, Xu W, Tan H, Li Y. Acta Mater 2005;53:2607.
[414] Bian Z, Kato H, Qin CL, Zhang W, Inoue A. Acta Mater 2005;53:2037.
[415] Hays CC, Kim CP, Johnson WL. Phys Rev Lett 2000;84:2901.
[416] Qin CL, Zhang W, Asami K, Kimura H, Wang XM, Inoue A. Acta Mater 2006;54:3713.
[417] Conner RD, Dandliker RB, Johnson WL. Acta Mater 1998;46:6089.
[418] Qiu KQ, Wang AM, Zhang HF, Ding BZ, Hu ZQ. Intermetallics 2002;10:1283.
[419] Hashimoto T, Kobayashi S, Maeda K, Takeuchi S. Precision measurements of pre-yield microstrain in amorphous alloys. In: Proceedings of the 6th international conference on the strength of metals and alloys. Oxford: Pergamon Press; 1983.
[420] Dragoi D, Ustundag E, Clausen B, Bourke MAM. Scripta Mater 2001;45:245.
[421] Aydiner CC, Ustundag E, Clausen B, Hanan JC, Winholtz RA, Bourke MAM, et al. Mater Sci Eng A 2005;399:107.
[422] Balch DK, Ustundag E, Dunand DC. Metall Mater Trans 2003;34A:1787.
[423] Clyne TW, Withers PJ. An introduction to metal matrix composites. Cambridge: Cambridge University Press; 1993.
[424] Clausen B, Lee SY, Ustundag E, Aydiner CC, Conner RD, Bourke MAM. Scripta Mater 2003;49:123.
[425] Hufnagel TC, Ott RT, Almer J. Mater Res Soc Proc 2006;903E:Z18.
[426] Zielinski PG, Ast DG. Acta Metall 1984;32:397.
[427] Hufnagel TC, Fan C, Ott RT, Li J, Brennan S. Intermetallics 2002;10:1163.
[428] Donovan PE, Stobbs WM. J Non-Cryst Solids 1983;55:61.
[429] Kuhn U, Eckert J, Mattern N, Schultz L. Appl Phys Lett 2002;80:2478.
[430] He G, Loser W, Eckert J, Schultz L. J Mater Res 2002;17:3015.
[431] Choi-Yim H, Conner RD, Johnson WL. Scripta Mater 2005;53:1467.
[432] He G, Eckert J, Loser W. Acta Mater 2003;51:1621.
[433] Conner RD, Choi-Yim H, Johnson WL. J Mater Res 1999;14:3292.
[434] Mercer C, Anglin PT, Cirincione R, Fenton C, Huang M, Soboyejo WO. Metall Mater Trans 2003;34A:1851.
[435] Fu XL, Li Y, Schuh CA. Scripta Mater 2007;56:617.
[436] Wang D, Li Y, Sun BB, Sui ML, Lu K, Ma E. Appl Phys Lett 2004;84:4029.
[437] Xu DH, Lohwongwatana B, Duan G, Johnson WL, Garland C. Acta Mater 2004;52:2621.
[438] Tang MB, Zhao DQ, Pan MX, Wang WH. Chinese Phys Lett 2004;21:901.
[439] Hofmann DC, Duan G, Johnson WL. Scripta Mater 2006;54:1117.
[440] Hajlaoui K, Yavari AR, Doisneau B, LeMoulec A, Botta WJF, Vaughan G, et al. Scripta Mater 2006;54:1829.
[441] Chen M, Inoue A, Zhang W, Sakurai T. Phys Rev Lett 2006;96:245502.
[442] Jiang WH, Liu F, Qiao DC, Choo H, Liaw PK. J Mater Res 2006;21:1570.
[443] Gu X, Livi KJT, Hufnagel TC. Mater Res Soc Proc 2003;754: CC7.9.1.